

**ULTRAFAST DYNAMICS AND NONLINEAR  
OPTICAL PROPERTIES OF GRAPHENE OXIDES  
AND NOBLE METAL NANOPARTICLES**

**JIANG XIAOFANG**

**NATIONAL UNIVERSITY OF SINGAPORE**

**2014**

**ULTRAFAST DYNAMICS AND NONLINEAR  
OPTICAL PROPERTIES OF GRAPHENE OXIDES  
AND NOBLE METAL NANOPARTICLES**

**JIANG XIAOFANG**

*(M.S., SUN YAT-SEN UNIVERSITY)*

**A THESIS SUBMITTED  
FOR THE DEGREE OF DOCTOR OF PHILOSOPHY  
DEPARTMENT OF CHEMISTRY  
NATIONAL UNIVERSITY OF SINGAPORE**

**2014**

## Declaration

I hereby declare that this thesis is my original work and it has been written by me in its entirety, under the supervision of A/P Xu Qing-Hua, (in the Ultrafast Laser Spectroscopy and Imaging Laboratory), Chemistry Department, National University of Singapore, between Aug. 2010 and Aug. 2014.

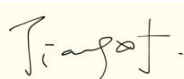
I have duly acknowledged all the sources of information which have been used in the thesis.

This thesis has also not been submitted for any degree in any university previously.

The content of the thesis has been partly published in:

- 1) **X.-F. Jiang**, Y.L. Pan, C.F. Jiang, T.T. Zhao, P.Y. Yuan, T. Venkatesan, Q.-H. Xu, "Excitation Nature of Two-photon Photoluminescence of Gold Nanorods and Coupled Gold Nanoparticles by Two-pulse Emission Modulation Spectroscopy", *J. Phys. Chem. Lett.*, 2013, 4, 1634-1638.
- 2) T.T. Zhao<sup>#</sup>, **X.-F. Jiang**<sup>#</sup>, N.Y. Gao, S. Li, N. Zhou, R.Z. Ma, Q.-H. Xu, "Solvent Dependent Two-Photon Photoluminescence and Excitation Dynamics of Gold Nanorods", *J. Phys. Chem. B*, 2013, 117, 15576-15583. (<sup>#</sup>equally contributed)
- 3) **X.-F. Jiang**, L. Polavarapu, S. T. Neo, T Venkatesan, Q.-H. Xu, "Graphene Oxides as Tunable Broadband Nonlinear Optical Materials for Femtosecond Laser Pulses", *J. Phys. Chem. Lett.*, 2012, 3, 785-790.

Jiang Xiaofang



20 Aug., 2014

Name

Signature

Date

## **Acknowledgements**

I am very fortunate to have the opportunity to study as a graduate student in NUS for the past four years. My sincere gratitude goes to plenty of peoples who played very important roles on the completion of this thesis as well as in my life. This section is dedicated to them.

The first person I would like to express my deep gratitude to is my supervisor, Prof. Xu Qing-Hua. I feel honored to be able to work in his group. Without his guidance and support, it would have been impossible for me to complete my PhD projects. His wide knowledge and personal encouragements are of great value for me. He gave lots of constructive comments to help me solving the tough problems in my experiments. He also offered me lots of good opportunities to practice and develop my research skills. I extremely appreciate him for providing me such a wonderful research experience for the past four years.

I am also very grateful to Prof. Venky for giving me the opportunity to work in femtosecond laser lab of NUSNNI-Nanocore. I sincerely thank him for his guidance and effort to find time to advise me when I needed, despite his hectic schedule. I have learnt a lot from his dedication and positive attitude towards work.

It was a great pleasure to work together with my colleagues in ultrafast laser laboratory. Herein, I would like to acknowledge all the help and support received from my seniors: Dr. Lakshmi, Dr. Yu Kuai, Dr. Guan Zhenping and Dr. Chen

Jianqiang. Special thanks go to Dr. Lakshmi, who gave me the first insight in the lab and the warmest friendship. His encouragements and suggestions continued during my graduate study even after he left Singapore, which means a lot to me. His diligence, passion for research and generous spirit of sharing all wonderful ideas with others inspired me. Many thanks should also be given to Dr. Yu Kuai, Dr. Guan Zhenping and Dr. Chen Jianqiang for their helpful discussions, technical supports and patience for my relentless questions.

For some of my other labmates, Dr. Ye Chen, Dr. Jiang Cuifeng, Dr. Zhao Tingting, Dr. Yuan Peiyan, Dr. Shen Xiaoqin, Ms Zhou Na, Mr. Gao Nengyue, Mr. Pan Yanlin, Ms Li Shuang, Ms Han Fei, Mr. Ma Rizhao, Mr. Zhu Hai, Ms Monalisa and Mr. Liu Peng, thanks for their help, support and discussions. Because of them, I had an enjoyable and cheerful journey during the four years of research. Thank you all for being good friends forever. I will cherish it in my whole life.

Additionally, I would like to acknowledge the financial support provided by the university in the form of NUSNNI- Nanocore PhD Scholarship, which ensures a smooth completion of my candidature.

Finally, I would like to thank my family and all my close friends. Their continuous love and support ensure me to pursue my interests without any worry and give me strength to go through.

# Table of Contents

Declaration.....	I
Acknowledgements.....	II
Table of Contents.....	IV
Summary.....	VIII
List of Tables.....	XI
List of Figures.....	XII
List of Publications.....	XVII
Chapter 1. Introduction.....	1
1.1 Background and Motivation.....	1
1.2 Nonlinear Absorption and Two-Photon Photoluminescence.....	4
1.3 Nonlinear Optical Properties of Noble Metal Nanoparticles.....	7
1.3.1 Localized surface plasmon resonance.....	7
1.3.2 Two-photon photoluminescence.....	9
1.3.3 Excitation dynamics.....	15
1.4 Nonlinear Optical Properties of Graphene Oxides.....	18
1.4.1 Structural revolution during reduction of graphene oxide.....	20
1.4.2 Excitation dynamics.....	23
1.4.3 Nonlinear absorption.....	25
1.4.4 Platform for optical applications.....	27
1.5 Ultrafast Spectroscopic Techniques.....	28
1.5.1 Pump-probe and transient absorption spectroscopy.....	28
1.5.2 Two-pulse emission modulation spectroscopy.....	31
1.5.3 Two-photon photoluminescence and lifetime measurement.....	32
1.5.4 Open-aperture Z-scan technique.....	34
1.6 Thesis Outline.....	35
References.....	38

Chapter 2. Excitation Nature of Two-Photon Photoluminescence of Gold Nanorods and Coupled Gold Nanoparticles Studied by Two-pulse Emission Modulation Spectroscopy .....	45
2.1 Introduction .....	45
2.2 Experimental Section.....	47
2.3 Localized Surface Plasmon Resonance of Coupled Au Nanospheres and Au Nanorods.....	51
2.4 Strong Two-Photon Photoluminescence of Coupled Au Nanospheres.....	52
2.5 Excitation Mechanisms Studied by Two-Pulse Emission Modulation and Pump-Probe Techniques .....	54
2.5.1 Fluorescein: a standard two-photon absorption organic dye .....	56
2.5.2 Au nanorods .....	57
2.5.3 Coupled Au nanospheres .....	59
2.6 Conclusion .....	61
References .....	63
Chapter 3. Solvent Dependent Two-Photon Photoluminescence and Excitation Dynamics of Gold Nanorods .....	66
3.1 Introduction .....	66
3.2 Experimental Section.....	68
3.3 Two-Photon Photoluminescence Variation of Au Nanorods in Different Solvents .....	71
3.4 Mechanisms and Dynamics of Two-Photon Photoluminescence Quenching in Organic Solvents .....	75
3.4.1 Excitation dynamics of Au nanorods in H <sub>2</sub> O, DMF and DEG solvents .....	76
3.4.2 Charge transfer between Au nanorods and organic solvents .....	82
3.5 Ion Effects on Two-Photon Photoluminescence and Excitation Dynamics of Au Nanorods in H <sub>2</sub> O.....	83

3.6 Conclusion.....	85
References .....	86
Chapter 4. Broadband Ultrafast Carrier Dynamics of Graphene Oxide and Reduced Graphene Oxide .....	90
4.1 Introduction .....	90
4.2 Experimental Section.....	93
4.3 Absorption and Photoluminescence of Graphene Oxide .....	95
4.4 Carrier Dynamics of Graphene Oxide .....	96
4.5 Carrier Dynamics of Reduced Graphene Oxide .....	102
4.6 Conclusion.....	108
References .....	109
Chapter 5. Graphene Oxides as Tunable Broadband Nonlinear Optical Materials for Femtosecond Laser Pulses .....	112
5.1 Introduction .....	112
5.2 Experimental Section.....	115
5.3 Characterizations of Graphene Oxide Films.....	118
5.4 Nonlinear Optical Properties of Graphene Oxide Films.....	119
5.4.1 Z-scan measurements under low excitation fluences .....	120
5.4.2 Z-scan theories for characterizing multiphoton process.....	121
5.4.3 Z-scan measurements under high excitation fluences .....	124
5.5 Tunable Nonlinear Optical Properties Controlled by Degree of Reduction .....	125
5.5.1 Laser irradiation reduction .....	125
5.5.2 Chemical reduction.....	129
5.5.3 Mechanism analysis .....	130
5.6 Graphene Oxide on a Flexible Plastic Substrate.....	131
5.7 Conclusion.....	132
References .....	133



Chapter 6. Conclusions and Outlook.....	135
6.1 Conclusions .....	135
6.2 Outlook.....	139

## Summary

Nonlinear optical phenomena, which normally occur with high intensity laser, are of extreme interest in the field of material science as well as in optoelectronics and bio-engineering applications. Femtosecond laser spectroscopy, with high peak power and unprecedented time resolution, offers a versatile and powerful tool to study these nonlinear optical behaviors. In this dissertation, several femtosecond laser spectroscopic techniques were employed to investigate the intriguing nonlinear optical properties of graphene oxide (GO) sheets and gold nanoparticles (Au NPs), including nonlinear absorption, two-photon photoluminescence (TPPL) as well as their electronic relaxation dynamics.

In Au NPs, gold nanorods (Au NRs) and coupled Au NPs are known to display intense TPPL compared to others. In Chapter 2, femtosecond two-pulse emission modulation (TPEM) and pump-probe measurements were performed to understand the excitation mechanism as well as aggregation enhancement mechanism of TPPL in Au NRs and coupled Au NPs. The TPEM profiles of Au NRs and coupled Au NPs showed much slower decay compared to the autocorrelation profile of laser pulses and TPEM result of a standard two-photon absorption organic dye. Their TPEM decay time constants match well with the lifetimes of the intermediate states measured by pump-probe experiment. These results support that the observed TPPL in Au NRs and coupled Au NPs results from two sequential one-photon absorption steps involving real intermediate states instead of coherent two-photon absorption.

These results also give direct evidence that previously observed aggregation enhanced TPPL arises from enhanced two-photon excitation efficiency, which is facilitated by two sequential plasma coupling enhanced one-photon absorption steps via intermediate states.

In Chapter 3, the solvent dependent TPPL properties of Au NRs and associated excitation dynamics were investigated by transient absorption spectroscopy. TPPL intensities of Au NRs in different organic solvents were found to be significantly quenched than that of Au NRs in H<sub>2</sub>O. Ultrafast dynamics of Au NRs in H<sub>2</sub>O, DMF and DEG were measured to understand the corresponding quenching mechanism. Different from the excitation decay behavior of Au NRs in H<sub>2</sub>O, an additional transient species was observed for Au NRs in DMF or DEG upon photo-excitation. This intermediate state is ascribed to the charge separated species, which serves as a direct evidence to support that the observed TPPL quenching in various organic solvents is due to electron transfer from electron-donating solvents to the excited Au NRs. This charge transfer mechanism was further supported by the observation that TPPL intensity of Au NRs in H<sub>2</sub>O was found to be quenched by nearly 5.0-fold in the presence of S<sup>2-</sup>.

In Chapter 4, by performing the similar pump-probe and transient absorption spectroscopy, we studied the broadband ultrafast carrier relaxation dynamics of as-prepared GO and reduced GO. Both as-prepared GO solution and film exhibited strong excited state absorption over a broad range of probe wavelengths from

visible to infrared, which is ascribed to the localized states induced absorption arising from the small sizes of  $sp^2$  clusters isolated by  $sp^3$  sites in GO sheets. Due to the formation of larger  $sp^2$  domains during reduction, transient absorption spectra of GO switched over from excited-state absorption to saturable absorption when GO was converted to totally reduced GO by thermal annealing. Carrier relaxation of reduced GO film was found to be significantly faster compared to that of GO and quite similar to that of pristine graphene.

Based on the carrier dynamics results listed above, we further investigated the nonlinear optical properties of GO and reduced GO by femtosecond open aperture Z-scan measurement in Chapter 5. The as-prepared GO films were found to exhibit strong broadband optical limiting behaviors, which were significantly enhanced upon partial reduction by using laser irradiation or chemical reduction methods. These laser irradiation or chemical reduction induced partial reduction of GO could result in a huge enhancement of effective two-photon and three-photon absorption coefficient at 400 nm and 800 nm respectively. Highly reduced GO films prepared by chemical reduction displayed strong saturable absorption behavior. The optical limiting thresholds of these partially reduced GO films are significantly lower than those of previously reported  $\pi$ -conjugated organic molecules and metal nanoparticles.

## List of Tables

<b>Table 3-1:</b> The fitting results of the pump-probe measurement for Au NRs in H <sub>2</sub> O, DMF and DEG at probe wavelength of 725 nm under excitation at 400 nm. ....	79
<b>Table 4-1:</b> Lifetimes of the transient absorption signal of GO films at different probe wavelengths under excitation at 400 nm.....	100
<b>Table 4-2:</b> Lifetimes of the transient absorption signal of reduced GO film at different probe wavelengths under excitation at 400 nm.....	106
<b>Table 5-1:</b> Linear transmittance (T), effective two-photon absorption coefficients ( $\beta_{\text{eff}}$ ), optical limiting onsets ( $F_{\text{on}}$ ) and thresholds ( $F_{50}$ ) of laser reduced GO films at 400 nm. ....	128
<b>Table 5-2:</b> Linear transmittance (T), effective two- and three-photon absorption coefficients ( $\beta_{\text{eff}}$ and $\gamma_{\text{eff}}$ ), optical limiting onsets ( $F_{\text{on}}$ ) and thresholds ( $F_{50}$ ) of laser reduced GO films at 800 nm.....	128

## List of Figures

<b>Figure 1.1:</b> Schematic diagram of one-photon and two-photon excited photoluminescence. ....	5
<b>Figure 1.2:</b> Schematic illustration of a localized surface plasmon resonance(LSPR). .....	7
<b>Figure 1.3:</b> Schematic band structure of noble metal showing the excitation and recombination transitions.....	10
<b>Figure 1.4:</b> Symmetry points and axes in the first Brillouin zone (a) and diagrams of band structures near the X and L symmetry points of Au (b). The dashed lines indicate the Fermi level. (c) Schematic structure of Au NRs. (d) TPPL spectrum from a single Au NR. Reprinted with permission from ref. 28. Copyright 2004 American Chemical Society.....	12
<b>Figure 1.5:</b> Sequence of excitation and relaxation dynamics processes and approximate time scales of metal nanoparticles. The pump pulse firstly interacts with the conduction electrons and creates the non-thermal electron distribution by LSPR absorption. Following by dephasing of the plasmon resonance and electron-electron (e-e) scattering, the excited electrons transfer their energy to the lattice by electron-phonon(e-ph) scattering. At the same time, acoustic vibrations can also be launched by sudden expansion of the electron cloud and the lattice with vibration period of tens of picoseconds. Finally, the hot electrons in nanoparticles reach thermal equilibrium with the surrounding environment by heat dissipation. .....	16
<b>Figure 1.6:</b> Schematic processes for fabrication of graphene oxide (GO) and reduced GO based films.....	19
<b>Figure 1.7:</b> Structural models (a&b) and the representative ideal band structures (c&d) of GO and reduced GO.....	21
<b>Figure 1.8:</b> (a) Direct chemical reduction of the metal precursors in the presence of GO or reduced GO suspensions; Reprinted with permission from ref. 122. Copyright 2008 American Physical Society (b) Simple assemble of noble metal nanocrystals of different shapes on the GO template by electrostatic interactions. Reprinted with permission from ref. 97. Copyright 2011 American Physical Society. .....	27
<b>Figure 1.9:</b> (a) Experimental setup of pump-probe and transient absorption spectroscopy. (b) Spectrum of white light continuum as probe beam measured by detector (Silicon Photodiode). The unit is voltage (V). ....	31
<b>Figure 1.10:</b> Experimental setup of two-pulse emission modulation spectroscopy. .....	32

<b>Figure 1.11:</b> Experimental setup of two-photon photoluminescence and lifetime measurement.....	33
<b>Figure 1.12:</b> (a) Experimental setup of the Z-scan measurement. D1 and D2: photodiodes. (b) Typical 2PA open aperture Z-scan curve. ....	35
<b>Figure 2.1:</b> UV-Vis extinction spectrum of Au NSs in the presence of different amounts of cysteamine to induce the aggregation and plasmon coupling. The insets are the TEM images of isolated and coupled Au NSs. ....	51
<b>Figure 2.2:</b> UV-Vis extinction spectra and TEM images (inset) of Au NRs.....	52
<b>Figure 2.3:</b> TPPL spectra of Au NSs in the presence of different amounts of cysteamine to induce the aggregation and plasmon coupling. TPPL spectra were measured using fs laser pulses at 800 nm as the excitation source. The inset is the power dependence of TPPL intensities of coupled Au NSs at 650 nm.....	53
<b>Figure 2.4:</b> Schematics of coherent two-photon absorption (2PA) process through a virtual state (left) and two sequential one-photon absorption (1PA) steps mediated by real intermediate states (right).....	55
<b>Figure 2.5:</b> Absorption and fluorescence spectra of fluorescein in water (pH was adjusted to 11 by using proper amount of NaOH). ....	56
<b>Figure 2.6:</b> TPPL measurement of fluorescein. The black curve is pulse autocorrelation profile measured by using a BBO doubling crystal.....	57
<b>Figure 2.7:</b> (a) TPPL measurement of Au NRs. (b) Pump-probe measurement result on Au NRs ( $\lambda_{\text{pump}}=800\text{ nm}$ , $\lambda_{\text{probe}}=760\text{ nm}$ ). The inset of (b) confirms the linear dependence of the pump-probe signal on the pump fluence to ensure the used pump power (indicated by the vertical dashed line) falling into the linear regime. ....	59
<b>Figure 2.8:</b> TPPL (a) and pump-probe (b) measurement results of the coupled Au NSs. The black curves in (a) is the pulse autocorrelation profile. The pump-probe measurement was performed with $\lambda_{\text{pump}}=800\text{ nm}$ , $\lambda_{\text{probe}}=760\text{ nm}$ and pump fluence (indicated by the vertical dashed line in the inset of (b)) falling in the linear regime of pump fluence dependent signals.....	61
<b>Figure 3.1:</b> (a) TEM image of PEG-SH capped Au NRs. (b) Extinction spectra, (c) TPPL spectra, and (d) relative TPPL intensities of Au NRs in H <sub>2</sub> O/DMF mixed solvents with different volume ratios.....	73
<b>Figure 3.2:</b> (a) Extinction spectra, (b) TPPL spectra, and (c) relative TPPL intensities of Au NRs in H <sub>2</sub> O/DEG mixed solvent with different volume ratios...	74
<b>Figure 3.3:</b> (a) Extinction and (b) TPPL spectra of Au NRs in various solvents..	74
<b>Figure 3.4:</b> Transient absorption spectra of Au NRs in (a) H <sub>2</sub> O, (b) DMF, and (c) DEG at the different delay times under excitation at 400 nm; (d) Single wavelength dynamics of Au NRs in H <sub>2</sub> O, DMF and DEG probed at 725 nm. ....	78

<b>Figure 3.5:</b> Transient absorption spectra of Au NRs in H <sub>2</sub> O, H <sub>2</sub> O/DMF mixture and DMF at the delay time of (a) 0 ps and (b) 500 ps; Single wavelength dynamics of Au NRs in H <sub>2</sub> O, H <sub>2</sub> O/DMF mixture and DMF probed at (c) 765 nm and (d) 740 nm under excitation at 800 nm with fluence of 25.4 μJ·cm <sup>-2</sup> .....	81
<b>Figure 3.6:</b> (a) Transient absorption spectra of Au NRs in DEG at the different delay times. (b) Single wavelength dynamics of Au NRs in DEG probed at 740 nm and 775 nm under excitation at 800 nm with fluence of 25.4 μJ·cm <sup>-2</sup> .....	82
<b>Figure 3.7:</b> Schematic mechanisms of TPPL quenching behavior in organic solvents compared to that in H <sub>2</sub> O. ....	83
<b>Figure 3.8:</b> TPPL intensities of Au NRs in different buffer solutions. The concentrations of buffer solutions are 10 mM. ....	83
<b>Figure 3.9:</b> TPPL intensities of Au NRs in H <sub>2</sub> O in the presence of different ions. The concentrations of ions are 1x10 <sup>-4</sup> M. ....	84
<b>Figure 3.10:</b> (a) Relative TPPL intensities of Au NRs in H <sub>2</sub> O with different concentrations of Na <sub>2</sub> S. (b) Transient absorption spectra of Au NRs in H <sub>2</sub> O with the concentrations of Na <sub>2</sub> S is 10 <sup>-1</sup> M at the different delay times under excitation at 400 nm. (c) Single wavelength dynamics of Au NRs in H <sub>2</sub> O with different concentrations of Na <sub>2</sub> S (0, 5×10 <sup>-4</sup> , 10 <sup>-2</sup> and 10 <sup>-1</sup> M) probed at 725 nm. ....	85
<b>Figure 4.1:</b> (a) AFM image of GO sheet. (b) UV-visible absorption spectra and photoluminescence (PL) spectra of GO at an excitation wavelength of 400 nm. (c) Time-resolved PL of GO solution measured via time correlated single photon counting (TCSPC) system. The detection wavelength was at 580 nm and no wavelength dependence of the PL lifetimes was found. ....	95
<b>Figure 4.2:</b> Transient absorption spectra of GO in water (a) and GO film (b) at different delay times upon excitation at 400 nm.....	97
<b>Figure 4.3:</b> Carrier relaxation dynamics probed at different wavelength of GO in water (a) and GO film (b). (c) Probe wavelength dependent time constants for carrier relaxation processes of GO films (τ <sub>1</sub> , τ <sub>2</sub> , τ <sub>3</sub> ). (d) Schematic band structure of semiconducting π-conjugated sp <sup>2</sup> domains in GO sheets. ....	98
<b>Figure 4.4:</b> (a) Carrier relaxation dynamics of GO solution probed at wavelength of 600 nm upon different pump fluence at 400 nm. The insets show the normalized data. (b) The absorption maximum after photo excitation is plotted for various pump fluences for GO solution.....	101
<b>Figure 4.5:</b> (a) Carrier relaxation dynamics of GO film probed at wavelength of 600 nm upon different pump fluence at 400 nm. The insets show the normalized data. (b) The absorption maximum after photo excitation is plotted for various fluences for GO film.....	101
<b>Figure 4.6:</b> (a) Transmittance spectra of the as-prepared GO and reduced GO (rGO)	



films. The inset shows the sample colors with a white background. (b) Raman spectra of as-prepared and reduced GO films..... 103

**Figure 4.7:** (a) Transient absorption spectra of reduced GO film at different time delays upon excitation at 400 nm. (b) Carrier relaxation dynamics of reduced GO probed at different wavelengths upon excitation at 400 nm. The solid lines are the analytical fits to the data using exponentials with two time constants:  $\tau_1$  and  $\tau_2$ . (c) Probe wavelength dependent time constant ( $\tau_2$ ) for carrier relaxation processes of reduced GO film (d) Schematic band structure of reduced GO showing intrinsic population near the Dirac point and its carrier relaxation via electron-electron scattering ( $\tau_1$ ) and electron-phonon scattering ( $\tau_2$ ). ..... 104

**Figure 4.8:** (a) Carrier relaxation dynamics of reduced GO film probed at wavelength of 650 nm upon different pump fluence at 400 nm. The insets show the normalized data. (b) The absorption maximum after photo-excitation is plotted for various pump fluences for reduced GO film. .... 107

**Figure 5.1:** Experimental setup for laser induced reduction of GO film. D1 and D2: photodiodes..... 117

**Figure 5.2:** Experimental setup for the measuring absorption spectra of laser reduced GO films..... 118

**Figure 5.3:** (a) UV-Vis absorption spectrum of GO in water and (b) the AFM image of the as-prepared GO..... 118

**Figure 5.4:** UV-Vis transmittance spectra and photographs (inset) of GO films of different thicknesses on glass substrates (Samples 1-5). ..... 119

**Figure 5.5:** Open aperture Z-scan results of a GO film (Sample 4) at 800 nm (c) and 400 nm (d) under different input fluences. .... 120

**Figure 5.6:** Plots of  $\ln(1-T)$  versus  $\ln(I_0)$  ( $I_0$ : input intensity) at 800 (a) and 400 nm (b)..... 123

**Figure 5.7:** Consecutive Z-scan measurements under high excitation fluences at (a) 800 nm (fluence of  $58 \text{ mJ}\cdot\text{cm}^{-2}$  at focal point) and (b) 400 nm (fluence of  $4.1 \text{ mJ}\cdot\text{cm}^{-2}$  at focal point)..... 124

**Figure 5.8:** Absorption spectra (a) and Raman spectra (b) of GO film (Sample 4) before and after laser irradiation at 400 nm for 10 min with fluence of  $8 \text{ mJ}\cdot\text{cm}^{-2}$ . ..... 125

**Figure 5.9:** (a,b) Open-aperture Z-scan curves of a partially reduced GO film (Sample 4, film thickness=140 nm) at 800 nm (fluence of  $25 \text{ mJ}\cdot\text{cm}^{-2}$  at focal point) (a) and 400 nm (fluence of  $0.6 \text{ mJ}\cdot\text{cm}^{-2}$  at focal point) (b) by laser irradiation of different periods of time. (Insets: normalized transmittance at the focus ( $z=0$ ) versus laser illumination time) (c,d) Optical limiting response of laser induced partially reduced GO films of different thickness to femtosecond laser pulses at 800 nm (c)

and 400 nm (d)..... 127

**Figure 5.10:** Linear transmittance (a) and Z-scan measurement results at 800 nm (fluence of  $25 \text{ mJ}\cdot\text{cm}^{-2}$  at focal point) (b) at 400 nm (fluence of  $0.6 \text{ mJ}\cdot\text{cm}^{-2}$  at focal point) (c) of a GO film (Sample 4) upon exposure to hydrazine vapor for different periods of time. .... 129

**Figure 5.11:** Schematic structures of GO at different stages of reduction: as-prepared (a), partially reduced (b) and highly reduced (c)..... 131

**Figure 5.12:** (a) UV-Vis spectrum of a GO film on a plastic substrate (Sample 6) and its optical limiting properties at (b) 800 and (c) 400 nm after laser induced reduction. .... 132

## List of Publications

1. **X.-F. Jiang**, Y.L. Pan, C.F. Jiang, T.T. Zhao, P.Y. Yuan, T. Venkatesan, and Q.-H. Xu, "Excitation Nature of Two-photon Photoluminescence of Gold Nanorods and Coupled Gold Nanoparticles by Two-pulse Emission Modulation Spectroscopy", *J. Phys. Chem. Lett.*, 2013, 4, 1634-1638.
2. T.T. Zhao<sup>#</sup>, **X.-F. Jiang**<sup>#</sup>, N.Y. Gao, S. Li, N. Zhou, R.Z. Ma, Q.-H. Xu, "Solvent Dependent Two-Photon Photoluminescence and Excitation Dynamics of Gold Nanorods", *J. Phys. Chem. B*, 2013, 117, 15576-15583. (<sup>#</sup>**equally contributed**)
3. Z.P. Guan, N.Y. Gao, **X.-F. Jiang**, P.Y. Yuan, F. Han, Q.-H. Xu, "Huge Enhancement in Two-photon Photoluminescence of Au Nanoparticle Clusters Revealed by Single Particle Spectroscopy", *J. Am. Chem. Soc.*, 2013, 135, 7272-7277.
4. **X.-F. Jiang**, L. Polavarapu, S. T. Neo, T Venkatesan, Q.-H. Xu, "Graphene Oxides as Tunable Broadband Nonlinear Optical Materials for Femtosecond Laser Pulses", *J. Phys. Chem. Lett.*, 2012, 3, 785-790.
5. S. Wang<sup>#</sup>, C.T. Nai<sup>#</sup>, **X.-F. Jiang**<sup>#</sup>, Y.H. Pan<sup>#</sup>, C.-H. Tan, M. Nesladek, Q.-H. Xu, K.P. Loh, "Graphene Oxide-Polythiophene Hybrid with Broad-Band Absorption and Photocatalytic Properties", *J. Phys. Chem. Lett.*, 2012, 3, 2332-2336. (<sup>#</sup>**equally contributed**)
6. L.W. Chen, **X.-F. Jiang**, Z.M. Guo, H. Zhu, T.-S. Kao, Q.-H. Xu, G. Ho, and M.H. Hong, "Tuning Optical Nonlinearity of Laser-ablation-synthesized Silicon Nano-particles via Doping Concentration", *J. Nanomater.*, 2014, 2014, 652829-7.
7. **X.-F. Jiang**, R.Z. Ma, T.T. Zhao, T. Venkatesan, and Q.-H. Xu, "Polarization Anisotropy Study on Two-Photon Photoluminescence of Gold Nanorods Suspension", 2014 (manuscript in preparation)
8. Q.L. Bao, J.Q. Chen, Y.J. Xiang, K. Zhang, S.J. Li, **X.-F. Jiang**, Q.-H. Xu, K.P. Loh, T. Venkatesan, "Graphene Nanobubble: A New Optical Nonlinear Material", 2014 (submitted)

# Chapter 1. Introduction

## 1.1 Background and Motivation

Optics is a crucial component of our daily lives. After propagating through material objects, light carries their visual information, which helps us to better understand this world. Under weak or moderate irradiation, the interactions between light and matter, such as refraction, reflection, diffraction, absorption, and scattering, are proportional to light intensity without altering the light frequency. This realm is named as linear optics, and the optical parameters of materials are constant. Linear optics beautifies physics. However, if all optical phenomena were linear, the world would be dull and without surprise.

Fortunately, the invention of the laser in 1960<sup>1</sup> gave rise to the research of optics at high intensities. By the presence of sufficiently intense laser, the optical parameters of material will not be constants but become functions of light intensity. These changes of optical parameters at high laser intensity result in plenty of new promising phenomena, such as second harmonic generation, two-photon absorption (TPA), two-photon photoluminescence (TPPL) and so on, which are called nonlinear optics. Shortly afterwards, the development of pulsed lasers based on a mode-locking technique made it possible to concentrate the energy in a very short duration around picosecond ( $1 \text{ ps} = 10^{-12} \text{ s}$ ) and achieve a quite intense peak power up to Gigawatt ( $1 \text{ GW} = 10^9 \text{ W}$ ).<sup>2,3</sup> Due to the super-linear fluence dependence in nonlinear optics, this

high peak power significantly facilitates the nonlinear coupling of light with matter. In recent years, the pulsed lasers initiated nonlinear optics has become a main research subject of great common interest in science and technology.

Several decades of successive progress of ultrafast laser technology led femtosecond ( $1 \text{ fs} = 10^{-15} \text{ s}$ ) lasers become commercially available.<sup>4</sup> Nowadays, pulses as short as tens of femtoseconds can be readily generated in a compact Ti:sapphire oscillator system.<sup>5</sup> Moreover, the output peak power of the oscillator can be amplified by chirped pulse amplification (CPA) technique<sup>6</sup> up to Terawatt ( $1 \text{ TW} = 10^{12} \text{ W}$ ) in a regenerative Ti:sapphire amplifier system. By utilizing nonlinear crystals, optical parametric oscillator (OPO)<sup>7</sup> and optical parametric amplifier (OPA)<sup>8</sup> can even further extend femtosecond laser to a tunable source with wide wavelength range from ultraviolet to mid-infrared. These significant advancements make femtosecond laser an extremely powerful and versatile tool in many scientific fields including physics, chemistry and biology.

There are two major characteristics of femtosecond laser: high peak power and short pulse duration, which are also the decisive factors in nonlinear optics. As we mentioned previously, the former feature is related to the enough energy to enable occurrences of nonlinear phenomena. The second feature, short pulse duration induces an unprecedented time-resolution for the optical spectroscopy, such as two-pulse pump-probe technique,<sup>9</sup> three-pulse photon echo technique<sup>10</sup> and so on. In these techniques, ultrafast carrier dynamics processes happened in materials can be

observed directly by inducing one or two subsequently time-delayed probe pulses after excitation by pump pulse. These various techniques of time-resolved spectroscopy provide the comprehensive information about carrier dynamic behaviors such as charge transfer and recombination processes, which are of great importance for understanding the mechanisms of nonlinear optical responses.

In this thesis, we performed several techniques of femtosecond laser spectroscopy to investigate some nonlinear optical properties of nanostructures. Nanostructures with at least one dimension in the range of approximately 1 to 100 nanometers ( $1 \text{ nm} = 10^{-9} \text{ m}$ ) have attracted lots of scientific interests in past few decades. Through the development in their synthesis and fabrication, various types of nanostructures have been prepared with chemical compositions covering from metals, semiconductors to carbon and shapes varying from dots, rods to nano-sheets. Owing to small sizes, nanostructures display extremely high surface area-to-volume ratio, quantum size effect and strong electro-dynamics interactions, which lead to some fascinating optical, electronic, magnetic and chemical properties not observed in the bulk material.<sup>11, 12</sup> Nanostructures open a novel research field with plenty of opportunities and thus act as the perfect candidates for nonlinear optical applications of femtosecond laser spectroscopy. It is noteworthy that the study of nonlinear optical properties of nanostructures is also vital for guidance of material developments for the potential nonlinear optical applications ranging from biological imaging to optoelectronics.

In our study, nonlinear absorption (NLA) properties, in particular TPA and TPPL of graphene oxide nanostructures and noble metal nanoparticles are systematically studied by employing ultrafast spectroscopy with femtosecond laser. Time-resolved spectroscopy such as transient absorption and pump-probe techniques are further utilized to investigate ultrafast carrier dynamics behaviors in time-domain to understand the underlying mechanism within these nonlinear absorption phenomena. In the rest of this chapter, a review about our target nanostructures and their nonlinear optical properties is given to provide a clear framework of the research conducted in this thesis. An introduction of the relevant techniques of ultrafast laser spectroscopy are also followed. At the end of this chapter, an outline of this thesis is presented.

## **1.2 Nonlinear Absorption and Two-Photon Photoluminescence**

Among a wide variety of nonlinear optical phenomena, nonlinear absorption (NLA) and its associated emission process attracted our great interests. NLA refers to the absorption change of a material as a function of fluence, such as saturable absorption (a reduced absorption) and reverse saturable absorption (increased absorption) with increase of excitation fluence. Upon sufficiently high fluence, the probability of a material absorbing more than one photons before relaxing to the ground state can be greatly enhanced. So, reverse saturable absorption commonly results from multiphoton absorption. Göppert Mayer gave the prediction of the two-photon absorption (TPA) using second order quantum perturbation theory as early as 1931.<sup>13</sup> However, only until 1961, Kaiser and Garret experimentally

confirmed the TPA induced fluorescence in a  $\text{CaF}_2:\text{Eu}^{2+}$  crystal.<sup>14</sup> TPA induced fluorescence is usually called as two-photon photoluminescence (TPPL). These studies marked the opening of TPA and TPPL research of bulk and nanostructured materials.

TPPL is one of the most promising phenomena in nonlinear optics and widely applied to bio-imaging and bio-sensing. Briefly, TPPL involves the absorption of two incident photons during the excitation transition from the ground state  $S_0$  to a higher-lying excited state  $S_1$  (TPA process) and the subsequent radiative recombination to ground state by emitting photons. The emission process of TPPL is similar to the steady state photoluminescence from one-photon excitation (linear absorption). The energy level diagram were shown in Figure 1.1.

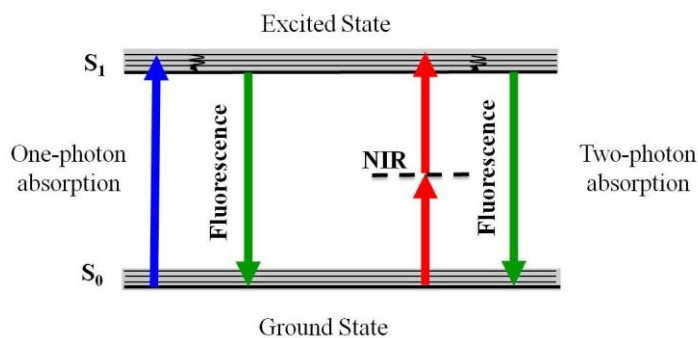


**Figure 1.1:** Schematic diagram of one-photon and two-photon excited photoluminescence.

Traditionally, TPA does not involve a real intermediate state and the absorption is proportional to the square of the incident intensity. The optical loss of the incident light can be described by the differential equation



$$\frac{dI}{dz} = -\alpha \frac{I}{1+I/I_s} - \beta I^2, \quad 1.1$$

where  $\alpha$  and  $\beta$  are the linear and two-photon absorption coefficients, respectively,  $I_s$  is the saturation intensity. Because the virtual intermediate state, there is rarely linear absorption at excitation wavelength in TPA materials, or only impurities may produce a small amount of linear absorption. TPA coefficient  $\beta$  is related to the third-order susceptibility, as well as a macroscopic parameter characterizing the material. Considering the individual molecular properties, TPA cross-section  $\sigma_{TPA}$  is more often utilized to evaluate the TPA ability for organic dye molecules. The relation between  $\beta$  and  $\sigma_{TPA}$  is given by

$$\sigma_{TPA} = \frac{\hbar \omega \beta}{N}, \quad 1.2$$

in which  $\hbar \omega$  is the photon energy of the incident light and  $N$  is the number density of molecules.

Compared to one-photon excitation, two-photon excitation wavelength is commonly infrared and localized in the biological transparent window, which has greater penetration depth. Additionally, due to the nonlinear absorption, TPPL occurs only at the focal volume of the excitation beam and there is no absorption in the out-of-focus specimen areas. These great merits inspired the research of TPA and TPPL in three-dimensional fabrication and imaging in vivo. Among the various types of TPA and TPPL materials, noble metal nanoparticles and graphene oxide based two dimensional (2D) nanostructured materials have gained eminent attentions. In the

sections as below, we will briefly review nonlinear absorption studies on these two particular kinds of nanostructured materials.

### 1.3 Nonlinear Optical Properties of Noble Metal Nanoparticles

To achieve a general understanding about nonlinear optical properties of noble metal nanoparticles, an introduction on the linear and nonlinear optical properties of noble metals and their corresponding electronic dynamics involved are highlighted in this section.

#### 1.3.1 Localized surface plasmon resonance

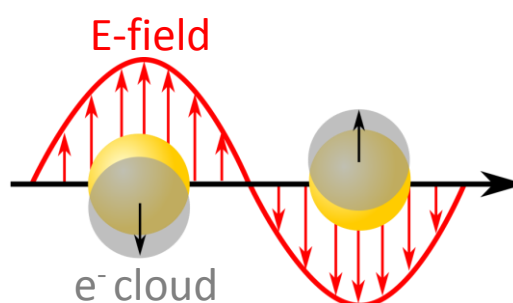


**Figure 1.2:** Schematic illustration of a localized surface plasmon resonance(LSPR).

The appealing optical properties of noble metals are mainly determined by the response of free electron occupying states in the conduction band. When the size of a metal particle is smaller than the light wavelength, a collective oscillation of free conduction electrons in noble metal can be induced by the presence of an external electromagnetic field (Figure 1.2). Owing to the high absorption in metals, this collective oscillation of electrons is typically confined at the surface of metal, termed as localized surface plasmon. When the frequency of an external field matches the

eigenfrequency of surface electrons oscillation against the restoring force of positive nuclei, the oscillation strength reaches a maximum, giving rise to a name of localized surface plasmon resonance (LSPR).

LSPR can be easily excited by incident light and lead to strong light extinction (scattering and absorption) in noble metal nanoparticles. So extinction spectra can be used to characterize the LSPR of noble metal nanoparticles. Based on the optical theorem, the extinction cross-section of nanoparticles  $\sigma_{ext}$  can be expressed via the relation<sup>15</sup>

$$\sigma_{ext} = \sigma_{abs} + \sigma_{sca}, \quad 1.3$$

where  $\sigma_{abs}$  and  $\sigma_{sca}$  are the absorption and scattering cross-sections, respectively. When the particle is much smaller than the wavelength of incident light, only dipole term is assumed in the absorption and scattering calculation. For spherical nanoparticles,

$$\sigma_{abs} = \frac{k_m}{\epsilon_m \epsilon_0} \text{Im}(\rho), \quad 1.4$$

$$\sigma_{sca} = \frac{k_m^4}{6\pi(\epsilon_m \epsilon_0)^2} (\rho)^2. \quad 1.5$$

In the above expressions,  $k_m$  is the wavenumber in vacuum,  $\epsilon_0$  and  $\epsilon_m$  are the permittivities of free space and surrounding medium, respectively. "Im" stands for the imaginary part of  $\rho$ , which is the polarizability of a spherical particle given by Clausius-Mosotti relation

$$\rho = 3V \varepsilon_m \varepsilon_0 \frac{\varepsilon_p - \varepsilon_m}{\varepsilon_p + 2\varepsilon_m}, \quad 1.6$$

where  $\varepsilon_p$  is the permittivity of the spherical particle, and  $V$  is its volume. Due to small value of  $V$ , scattering is much weaker compared to absorption for small nanoparticles, and thus the absorption cross section is approximately equal to the extinction cross section. The nanoparticles involved in the research of this thesis are mainly around tens of nanometers, so the measured extinction spectra of their assemble solution can be used for the absorption analysis.

There are two unique merits for LSPR. First, LSPR can greatly enhance the electromagnetic fields near the particle's surface, and this enhancement will rapidly fall off with distance from the surface. This strong local field enhancement induced by LSPR has been widely utilized to amplify various optical signals such as Raman scattering and fluorescence.<sup>16, 17</sup> Second, the LSPR wavelength can be easily monitored by the extinction spectra of metal nanoparticles, which can be tuned from ultraviolet to infrared region by controlling particles' size, shape, the refraction index of the surrounding medium as well as the plasmon coupling induced by aggregation of nanoparticles. This tunable feature of LSPR wavelength makes noble metal nanoparticles attractive in various chemical and biological applications as well as the fundamental studies on the light interaction with matter.

### **1.3.2 Two-photon photoluminescence**

Photoluminescence (PL) of bulk noble metal films under one-photon excitation

was first reported by Mooradian et al in 1969,<sup>18</sup> with a very low quantum efficiency of  $10^{-10}$ . This emission was ascribed to the direct radiative recombination of electrons in conduction band with the holes in d-band created after one-photo excitation, as shown in Figure 1.3.

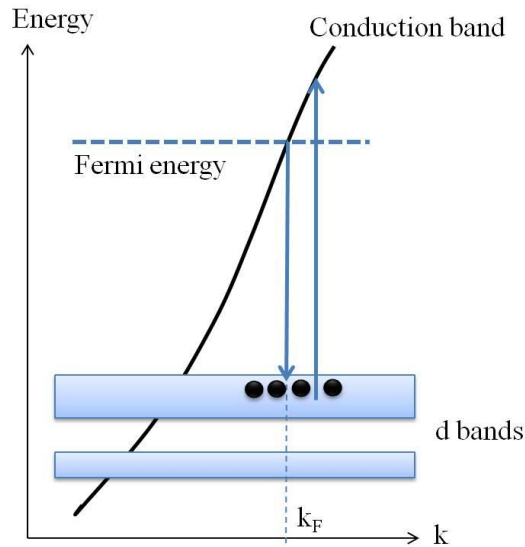


**Figure 1.3:** Schematic band structure of noble metal showing the excitation and recombination transitions.

Owing to its low quantum efficiency, there have been rare studies about the PL of noble metals until the discovery of much higher emission efficiency on the roughened noble metals films in 1986 by Boyd et al.<sup>19</sup> In their study, the weak emission of noble metals was found to be enhanced by the localized electron field of surface plasmon induced by protrusions on the rough surface. Their spectra reveal new features, such as peak positions, correlated with the strong interband transitions at selected X or L symmetry points in Brillouin zone, which is also consisted with the later report by Apell et al. in 1988.<sup>20</sup> Here it is noteworthy that the study by Boyd et al. is the first report on TPPL of noble metals.

Since the first report on TPPL of noble metals by Boyd et al,<sup>19</sup> numerous studies have been sequentially reported on the TPPL of different metal nanostructures.<sup>21-24</sup> Among them, the work by Wang et al. in 2005 is a major milestone on the TPPL of noble metals.<sup>24</sup> In this remarkable work, the application of gold nanorods (Au NRs) as the imaging agents was first demonstrated in vivo imaging of single nanorod flowing in the mouse ear blood vessel. Soon afterwards, the TPPL imaging capability of Au NRs and other nanostructures was highlighted in many investigations, due to their bio-compatibility, strong TPPL signal, resistance to photo-bleaching, chemical stability, ease of synthesis and the deep penetration ability.<sup>25, 26</sup>

Since these promising bio-imaging applications of gold nanoparticles, mechanisms underlying the TPPL of gold nanoparticles have attracted significant interests in noble metal research area. Among them, the emission and excitation mechanisms are two important issues that need to be clarified.

Previously, most studies on the emission of gold were focused on the PL in visible range.<sup>22, 27, 28</sup> These results showed that the TPPL shared similar emission mechanism with one-photon photoluminescence (1PPL) and independent on the excitation approach. The origin of TPPL from gold nanoparticles is widely believed to be the radiative recombination of sp-band electrons with d-band holes through interband transition, as shown in Figure 1.4.<sup>18, 19</sup> The work by Imura et al. lent strong support to this conclusion that the observed two emission peaks (520nm, 630nm) from a single nanorod were consistent with the theoretical interband energy bandgap around L (111

direction) and X (001 direction) symmetry points of the Brillouin zone of gold, respectively.<sup>28</sup> These two emission peaks have different incident polarization dependences, which was attributed to the crystalline structure and the band structure of Au NRs.

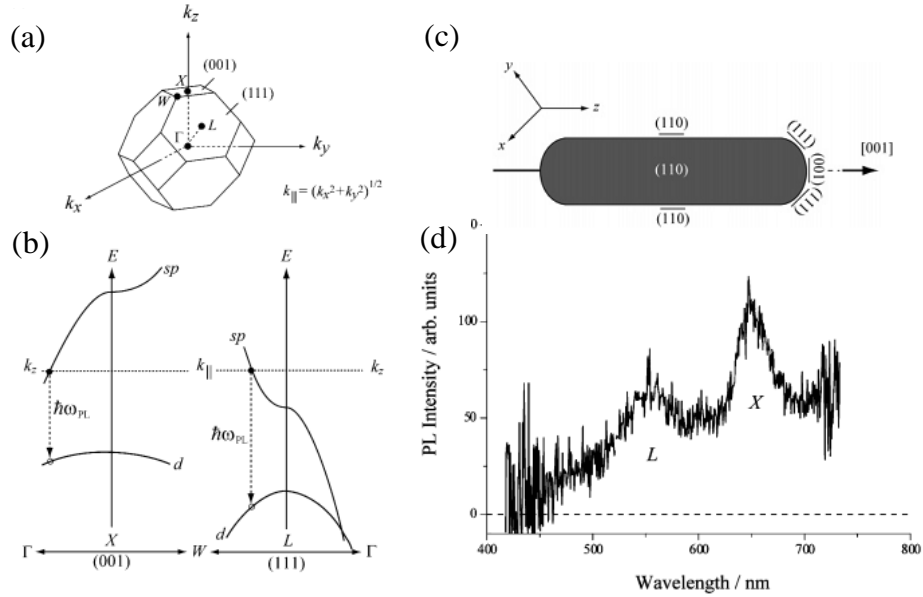


**Figure 1.4:** Symmetry points and axes in the first Brillouin zone (a) and diagrams of band structures near the X and L symmetry points of Au (b). The dashed lines indicate the Fermi level. (c) Schematic structure of Au NRs. (d) TPPL spectrum from a single Au NR. Reprinted with permission from ref. 28. Copyright 2004 American Chemical Society.

However, the discovery of the infrared emission ( $> 800$  nm) besides the visible emission from gold rough films by Beversluis et al. contested this well-known interpretation for the origin of overall PL from gold.<sup>21</sup> In contrast with direct interband radiative recombination for the origin of visible emission, they proposed a more comprehensive explanation by adding the origin of infrared emission as the near field intraband transition coupling to the far field by the radiative decay of localized surface plasmons. Subsequently, some related works have emphasized this plasmonic feature

of emission from various gold nanostructures, especially Au NRs.<sup>29, 30</sup> Their results indicated that the TPPL spectra resembled their corresponding scattering spectra, and the TPPL intensity strongly depended on the orientation of the incident polarization. These features are consistent with the properties of surface plasmon, and hence they claimed that the origin of PL from gold is plasmonic emission, which is the radiative decay of surface plasmons generated after the interconversion of the excited electron-hole pairs. These arguments for TPPL were also supported and highlighted in the 1PPL studies on gold nanostructures.<sup>31</sup> Recently, secondary light emission such as the resonant electronic Raman scattering from the continuum electron-hole pairs created by high electronic temperature was also proposed as an alternate description of the origin of TPPL in Au nanoparticles by Huang et al.<sup>32</sup>

Actually, the plasmonic features of TPPL as the evidences of resonant plasmonic emission are not plausible, since similar characteristic would also be observed if the emission from the interband radiative recombination is enhanced by the surface plasmon. It is difficult to distinguish these two emission mechanism models for TPPL in noble metals based on the present experiment results.

Besides the controversial emission mechanisms proposed, the excitation nature of TPPL in noble metal nanoparticles is not conclusive as for now. Many efforts have been made to understand the excitation processes of strong TPPL in gold nanostructures.<sup>24, 33</sup> Two possible excitation mechanisms have been proposed to account for the observed intense TPPL in Au NPs. One is coherent two-photon



absorption process and the other is two sequential one-photon absorption processes. The coherent two-photon absorption model, which is commonly used for organic dye molecules, involves a typical simultaneous absorption of two photons through a virtual intermediate state described in the preceding section. This coherent two-photon absorption mechanism was proposed to account for TPPL in noble metal nanoparticles and supported by the observation of a  $\cos^4\theta$  excitation polarization dependence of TPPL intensities.<sup>24, 26</sup> The second model assumes that the two-photon excitation process involves two sequential one-photon absorption steps that are mediated by real intermediate states. This model was initially proposed based on the observation of the  $\cos^2\theta$  excitation polarization dependence of TPPL in single Au NRs, which is contradictory from the previous observations.<sup>33</sup> This model gained strong support from the impressive work by Biagioni et al, who found that TPPL intensities of Au nanowires were insensitive to pulse duration for pulse widths of  $<1$  ps.<sup>34,35</sup>

In general, both explanations about the emission and excitation mechanisms have their own supporting evidences but contradict each other in some way. It is very challenging to investigate the true nature of TPPL in noble metal nanoparticles and find a clear guidance for the applications of TPPL-based imaging and sensing. Chapter 2&3 of this thesis present the studies of the excitation nature as well as the solvent dependent properties of TPPL in gold nanoparticles, which might give some inspirations for truly understanding TPPL nature of noble metal nanoparticles.

### 1.3.3 Excitation dynamics

Excitation dynamics and its associated time scales can provide comprehensive information about the interaction of the excitation light with the conduction electrons and lattice of particles, which are also the crucial elements for understanding the nonlinear optical mechanism in noble metal nanoparticles. In this subsection, we will generally review the excitation dynamics studies of noble metal nanoparticles and give a description of the proposed theoretical models.

Till now, the electron dynamics has been widely studied on various noble metal nanoparticles with different size, shapes and compositions by ultrafast laser spectroscopy.<sup>36-38</sup> Transient absorption and pump-probe techniques involving femtosecond laser pulses are frequently used to detect the excitation dynamics in picosecond timescales. A generic sequence of events following the photo excitation of noble metal nanoparticles has been found in most studies and is summarized schematically in Figure 1.5.

As shown in Figure 1.5, upon excitation of a laser pulse, the induced dipolar oscillator of the conduction electron (light induced LSPR) leads to the absorptions of metal nanoparticles by interband or intraband transitions, creating the excited electrons occupied in different levels of conduction band. The density of excited states depends on the spectral shape of the laser pulse.<sup>39-42</sup> This corresponding electron distribution is non-thermal and with the coherent phase memory between the

electronic states and electromagnetic field. Soon afterwards, this coherent electron distribution will rapidly dephase through electron-surface scattering or radiation damping.<sup>36, 43, 44</sup> This dephasing time relies on the size of nanoparticles and thus, can be reflected in the LSPR line width.<sup>45</sup> The reason can be explained by the different functional dependence of the surface electron scattering and radiative damping contributions on dimensions of particles. The dephasing times usually are very fast and round 10 fs, and thus direct time-resolved measurements of these processes are very difficult, and also beyond the scope of this thesis.

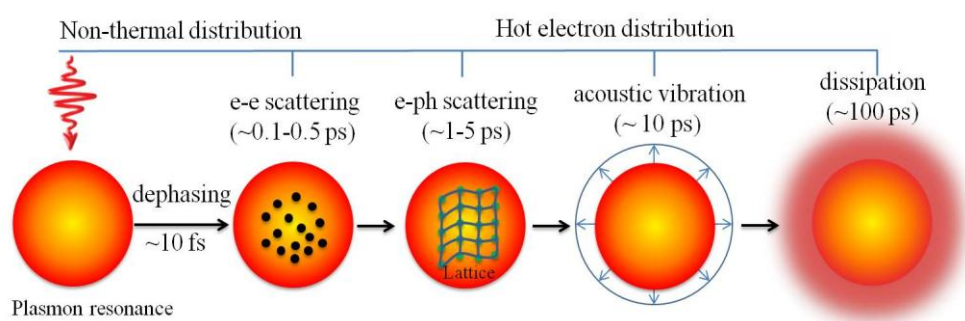


**Figure 1.5:** Sequence of excitation and relaxation dynamics processes and approximate time scales of metal nanoparticles. The pump pulse firstly interacts with the conduction electrons and creates the non-thermal electron distribution by LSPR absorption. Following by dephasing of the plasmon resonance and electron-electron (e-e) scattering, the excited electrons transfer their energy to the lattice by electron-phonon(e-ph) scattering. At the same time, acoustic vibrations can also be launched by sudden expansion of the electron cloud and the lattice with vibration period of tens of picoseconds. Finally, the hot electrons in nanoparticles reach thermal equilibrium with the surrounding environment by heat dissipation.

Following the dephasing of plasmon resonance, the excited electrons do not directly transfer energy to lattice owing to the small heat capacity of lattice. Instead, they equilibrate rapidly to thermalization by creating a hot electron distribution via electron-electron (e-e) scattering.<sup>46-51</sup> These hot electrons can reach electron

temperatures up to hundreds of degrees, which were found to be dependent on the excitation intensity.<sup>52, 53</sup> At this point, coherent memory of the way how electrons excited would be wiped out by e-e collision. Based on the experimental results, the time scale of e-e scattering in noble metals is round hundreds of femtosecond.<sup>39, 50</sup>

Sequentially, these hot electrons cool down and relax their heat to lattice and environment through electron-phonon (e-ph) scattering. This energy exchange between electron and lattice can be described by a two-temperature model (thermal equilibriums of electron and lattice, respectively).<sup>54</sup> By e-ph scattering, the hot electrons transfer their energy to the phonon in lattice and thus heat the lattice in nanoparticles. The time scale of e-ph coupling is generally several picoseconds and also relies on the excitation intensity.<sup>48, 55</sup> Similar to that of e-e scattering, it also increases with increase of excitation intensity, which can be easily understood by the electronic temperature dependent electron heat capacity. Additionally, the heating of the lattice will further induce a rapid thermal expansion of the particles, which launch an acoustic vibration related to the sound.<sup>38, 56-58</sup>

The final step of electron relaxation is heat transfer from particles to the dielectric matrix of environment, within in a few hundred picoseconds. There are two components for this cooling process: charge transfer across the interface and heat dissipation to the surrounding environment. These two processes have quite similar time scales, so it is very difficult to separate them in experimental measurement. Most previous excitation dynamics studies on the longer time scales (hundreds of

picoseconds) were mainly focused on the heat dissipation process.<sup>52, 54-57</sup> It was found that this heat diffusion process was very sensitive to the thermal conductivity of the surrounding medium.

In this thesis, the solvent dependent excitation dynamics results of Au NRs presented in Chapter 3 indicated the occurrence of charge transfer processes across the interface between Au NRs and the surrounding solvents, and it lent a strong support for the observed interesting TPPL variation phenomena of Au NRs in different solvents. This study provides a new perspective for understanding the excitation dynamics in noble metal nanoparticles.

## **1.4 Nonlinear Optical Properties of Graphene Oxides**

Graphene, the basic building block of graphite, is a one-atom-thick 2D sheets of  $sp^2$  carbon atoms that are densely packed in a honeycomb crystal lattice.<sup>59, 60</sup> Intrinsic graphene can act as a semi-metal or zero-gap semiconductor due to its linear energy dispersion relation of Dirac electron, which is very attractive for physicists.<sup>59-61</sup> Several approaches such as epitaxial growth,<sup>62</sup> chemical vapor deposition(CVD),<sup>63</sup> physical exfoliation,<sup>64</sup> solvent assisted exfoliation,<sup>65, 66</sup> longitudinal “unzipping” of carbon nanotubes (CNTs),<sup>67</sup> and reduction of graphene derivatives,<sup>68-71</sup> have been reported to prepare graphene. Among all these methods, chemically derived graphene oxide (GO) as a precursor offers a potential route towards low cost, large scale production of solution processed graphene-based materials.<sup>71</sup> By various methods of

reduction, GO can be readily transformed into a semiconductor or graphene-like semi-metal named reduced GO.<sup>69</sup> The fabrication processes of GO and reduced GO based films are briefly illustrated in Figure 1.6. Facile synthesis and solution-processing of GO and reduced GO facilitates not only the fabrication of graphene-based nano-electronic devices,<sup>69</sup> but also the exploration of chemically derived GO-based materials as a new type of macromolecule that can be complex with many organic and inorganic systems.<sup>72, 73</sup>

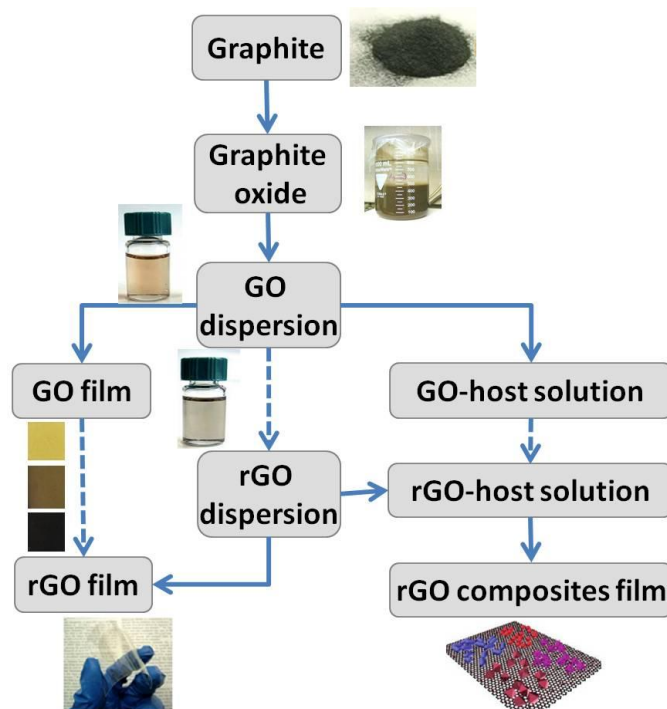


**Figure 1.6:** Schematic processes for fabrication of graphene oxide (GO) and reduced GO based films.

Owing to the unique properties, solution-processability and potential applications of GO-based materials, rapid progresses have been made in this field. Nonetheless, research toward the graphene based nonlinear optical applications have just begun. Many challenges and opportunities still remain. In this section, we will discuss some

basics of GO and reduced GO, placing emphasis on their nonlinear absorption properties and associated electronic dynamics.

#### **1.4.1 Structural revolution during reduction of graphene oxide**

Chemically derived GO was firstly reported in 1859 by Brodie et al.<sup>74</sup> However, only in last decade, the structures of GO and reduced GO sheets have been extensively identified in details by modern techniques like Raman spectroscopy,<sup>75, 76</sup> high resolution transmittance electron microscopy (TEM),<sup>77, 78</sup> atomic force microscopy (AFM),<sup>79, 80</sup> scanning tunneling microscopy (STM).<sup>81, 82</sup> Actually, the determination of structures in GO is very challenging because of its non-stoichiometric chemical composition. In general, GO sheets were prepared by oxidative exfoliation of graphite into atomically thin carbon sheets decorated with oxygen-containing functional groups.<sup>68, 69, 71, 83</sup> Compared to an ideal monolayer of graphene (thickness is around 0.34 nm), the thickness of a monolayer GO sheet is much thicker and approximately 1~1.4 nm, which is due to the presence of the functional groups and absorbed molecules.<sup>69, 83, 84</sup> These functional groups contain mainly hydroxyls and epoxies, but with wide variability in type and coverage in basal plane. As a consequence, GO sheets consist of ordered small  $sp^2$  (2-3 nm) clusters isolated within a non-uniform coverage of  $sp^3$  C-O matrix, which is shown in Figure 1.7a&b. their corresponding schematic band diagrams are also presented in Figure 1.7c&d.

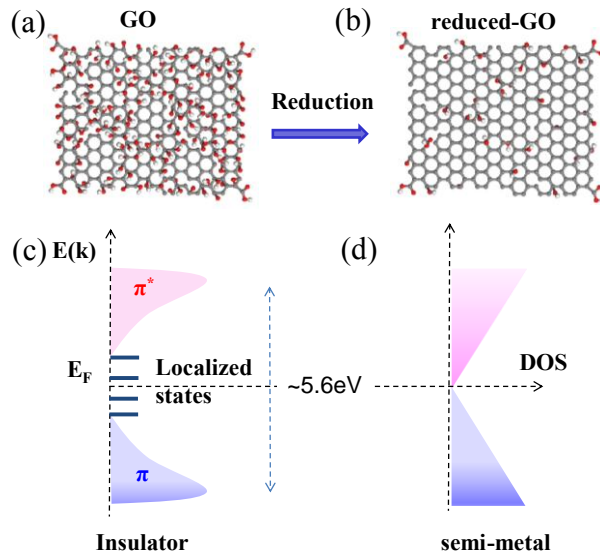


**Figure 1.7:** Structural models (a&b) and the representative ideal band structures (c&d) of GO and reduced GO.

As well known in carbon material, which contains both  $sp^2$  and  $sp^3$  sites, the electronic properties are mainly determined by the  $\pi$  state of the  $sp^2$  states. The  $\sigma$  bonds of  $sp^2$  and  $sp^3$  sites give rise to  $\sigma$  valence and  $\sigma^*$  conduction band states, separated by a band gap of order 6 eV.<sup>85</sup> The strong localized  $\pi$  and  $\pi^*$  states of the  $sp^2$  clusters lie within this  $\sigma$  and  $\sigma^*$  gap, form the band edges and control the bandgap. The bandgap of the carbon mixture mainly depends on the configurations of  $sp^2$  domains, such as size, shape and the relative fraction of  $sp^2$  domains in GO sheets. According to the theoretical calculation, the bandgap linearly scales with the  $sp^2$  fraction in disordered carbon systems.<sup>86</sup> These hypotheses are confirmed by the experimental study on the PL of GO solution.<sup>87</sup> These localized states arising from the small  $sp^2$  clusters within the  $sp^3$  matrix lead to the localization of e-h pairs, which facilitate the radiative recombination of small clusters.

Besides the bandgap opening, the oxygen-containing functional groups make GO



strongly hydrophilic and also give rise to remarkable mechanical strength along with molecular-level chemical sensing capability. After controllably and carefully removing specific oxygen groups by the different reduction processes, such as chemically,<sup>69, 88</sup> thermally,<sup>65</sup> electrically<sup>89</sup> and photo-thermally,<sup>90-92</sup> insulating GO can be transformed into semiconducting or conducting reduced GO. Although the electronic mobility of the reduced GO is less compared to the mechanically cleaved graphene due to the defects,<sup>69</sup> the structure evolution of GO by reduction can tailor the bandgap by tuning the ratio of the  $sp^2$  and  $sp^3$  fractions, which results in surprising optical properties of GO and reduced GO, such as the tunable photoluminescence and nonlinear optical properties.<sup>87, 93</sup>

In addition, the different types of oxygen-containing functional groups on the basal plane and the sheet edge allow GO to interact with a wide range of materials in non-covalent, covalent and ionic manner, so the functional hybrids with unique properties can be readily synthesized.<sup>72, 73</sup> The good solubility of GO in wide range of solvents enables the use of low-cost solution processing techniques to fabricate various potentially useful graphene-based materials.<sup>73</sup> To date, graphene-based composites have been successfully made with inorganic, organic nanostructures and are intensively explored in applications such as photovoltaic devices,<sup>94</sup> and photo-catalysis,<sup>95</sup> sensing platforms,<sup>61, 96</sup> Raman enhancement<sup>97</sup> and so on.

## 1.4.2 Excitation dynamics

According to the previous discussion, the oxygen-containing functional groups in graphene basal plane have altered the zero bandgap of graphene to a large bandgap insulator or semiconductor of GO and reduced GO. The excitation dynamics behavior of GO and reduced GO is no longer analogous to graphene but similar to a semiconductor.

The carrier dynamics in semiconductor can be generally described as below. When a photon of energy  $\hbar\omega$  is absorbed by a semiconductor with an energy bandgap  $E_{\text{gap}} < \hbar\omega$ , an electron is promoted from valence band to conduction band with an excess energy  $(\hbar\omega - E_g)$  and a nonzero momentum wave vector determined by the band structure. This process is followed by transferring the excess energy and momentum from excited electron to other electrons, holes and crystal lattice via various e-e and e-ph interactions. Eventually, the excited electron recombines with a hole in the valence band. These relaxation mechanisms and the time scales over which they occur, such as radiative recombination (PL) and nonradiative process (charge transfer process) inside the system, constitute the whole excitation dynamics behavior.

In the rapid progress of graphene research field, the fundamental studies on the excitation dynamics inside graphene play a vital role on understanding the basic optoelectronic properties and developing their electronic devices. Ultrafast carrier

dynamics of freestanding thin graphite films has been reported by Breusing et al.<sup>98</sup> By utilizing the single wavelength pump-probe technique with a ultrashort 7 fs laser, they found that a rapid intraband carrier equilibration with separated electron and hole chemical potentials were achieved within a short time scale of 30 fs upon laser excitation, and then phonon-mediated intraband carrier cooling occurred on a longer time scale of 100 fs. In 2008, Jahan et al.<sup>99</sup> found that the longer carrier relaxation time in epitaxial graphene layers grown in SiC wafers was inversely proportional to the degree of crystalline disorder.

Shortly afterwards, Huang et al.<sup>100</sup> employed the transient absorption microscopy to investigate the charge carrier dynamics of multilayer epitaxial graphene. Similar to previous report, they found the bi-exponential decay of the carrier cooling process, and the time constants showed a significant dependence on excitation carrier density. The fast and slow relaxation times were assigned to the e-ph coupling and the hot phonon effect, respectively. Later, ultrafast dynamics of CVD-grown multilayer graphene has been investigated by Obraztsov et al.<sup>101</sup> and Shang et al.<sup>102</sup>, separately. They revealed that broadband absorbance change is due to the band filling effect, and the ultrafast carrier kinetics could be described as the quasi-particle dynamics, which means the low-energy single-particle excitation with renormalized energy due to e-e, e-ph scattering and ph-ph interactions.<sup>102</sup> Besides, when the probe photon energy was higher than that of the pump photon, the Auger recombination and impact ionization also played a significant role in the dynamics of photo excited carriers in graphene.

Very recently, a few research groups have paid special attention to the studies of carrier relaxation dynamics of solution processing reduced GO.<sup>103-106</sup>

As it is known that the optical and electronic properties of reduced GO depend on the type of reduction method,<sup>68, 69</sup> there is a need to understand the ultrafast dynamics of GO and how the dynamic changes within the reduction process. On the other hand, since graphene and GO are both well-known electron acceptors, the research on their carrier dynamics is a good way to understand the charge transfer process between the electron donors and acceptors, which would offer some references to improve the performance of graphene and GO-based applications on photovoltaics, photo-catalysis and so on.<sup>107</sup> In Chapter 4 of this thesis, the excitation dynamics of GO solution, GO film and reduced GO film were comparatively studied to obtain a clear understanding of their carrier relaxation processes in GO-based materials.

### **1.4.3 Nonlinear absorption**

The linear dispersion and zero bandgap of graphene provide the possibility of exceptionally high optical nonlinearity, such as second harmonic generation,<sup>108</sup> saturable absorption,<sup>109</sup> optical nonlinear Kerr effect,<sup>110</sup> multiphoton absorption,<sup>111</sup> high harmonic generation and so on. Saturable absorbers display an decreased absorption at high excitation intensity, which are potentially useful for pulse compression, mode locking and Q-switching.<sup>112</sup> The ultrafast saturable absorption properties of graphene has been experimentally and theoretically investigated in fiber

laser for mode-locking.<sup>119, 120</sup> Their results predicted that atomic graphene has very low saturation intensity, ultrafast recovery time, tunable modulation depth and wideband tuneability, which could be well understood by a model with valence band depletion, conduction band filling and ultrafast intraband carrier thermalization within the linear dispersion from the uniform  $sp^2$  bonded atomic hexagonal pattern.<sup>121</sup>

However, for GO sheet, it contains a mixture of electronically conducting  $sp^2$  and insulating  $sp^3$  carbon domains, which breaks the linear dispersion relation of graphene and make GO sheets a insulator. Fortunately, these small sized  $sp^2$  fragments of several conjugated repeating units induce some discrete energy states, which are highly localized within the large  $\sigma$ - $\sigma^*$  gap of the  $sp^3$  matrix. These localized states lend the facility of excitation and recombination in a wide frequency range, which might have interesting implications on their nonlinear absorption applications.

Optical limiting materials display a decreased transmittance at higher input laser intensity, which can be utilized to protect eyes and sensitive instruments from laser induced damage.<sup>113-116</sup> Strong nonlinear absorption such as multiphoton absorption and excited state absorption, detailed in the above section is the main contributor for high optical limiting performance.<sup>117</sup>  $\pi$ -conjugated organic molecules such as porphyrins,<sup>118</sup> phthalocyanines<sup>118</sup> and other large aromatic molecules are commonly known to exhibit optical limiting activity at femtosecond laser pulses due to strong multiphoton absorption or excited state absorption. The isolated  $sp^2$  clusters in GO sheets resemble  $\pi$ -conjugated organic molecules with strong nonlinearity, which

motivated us to investigate the nonlinear optical properties of GO. So the chapter 5 of this thesis presented the work about the nonlinear absorption of GO and reduced GO films with femtosecond laser pulses. This investigation of femtosecond nonlinear optical properties of GO and GO-based materials is vital for the development of graphene-based ultrafast optoelectronic applications in the future.

#### 1.4.4 Platform for optical applications

Due to the 2D structure and good solubility, GO can act as an ideal template for the synthesis of GO-based hybrids. Depending on the different types of anchored nanoparticles, the GO-based or reduced GO-based nanocomposites have been applied in a broad range of areas.<sup>73</sup> Due to tunable LSPR properties, noble metal nanoparticles are good candidates anchored on GO sheets, which may inspire synergic effects and achieve some interesting optical properties. So in this subsection, we will emphasize on the GO-metal based nanocomposites, where GO acts as chemically tunable platforms for various applications.

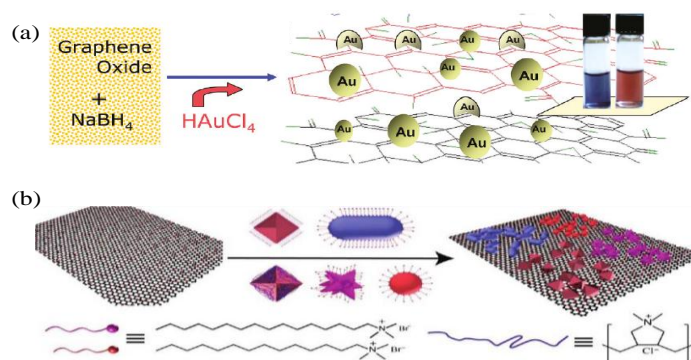


**Figure 1.8:** (a) Direct chemical reduction of the metal precursors in the presence of GO or reduced GO suspensions; Reprinted with permission from ref. 122. Copyright 2008 American Physical Society (b) Simple assemble of noble metal nanocrystals of

different shapes on the GO template by electrostatic interactions. Reprinted with permission from ref. 97. Copyright 2011 American Physical Society.

Generally, there are two basic ways for preparing graphene–metal based composites. As shown in Figure 1.8, the first approach is the direct chemical reduction of the metal precursors in the presence of GO or reduced GO suspensions.<sup>122</sup> The other efficient method is the solution mixing. Due to electrostatic interactions, noble metal nanocrystals of different shapes can be simply assembled on the GO platform.<sup>97</sup> The extinction spectra of Au nanocrystals became broadened and red-shifted from the visible to the near infrared upon the formation of GO-Au nanocomposites. Similar to GO, metal nanoparticles are the promising candidates for nonlinear optical devices, such as optical limiter or saturable absorber.<sup>123-125</sup> GO and metal nanoparticles accordingly can be expected for win-win cooperation of fabricating the broadband nonlinear optical devices.

## **1.5 Ultrafast Spectroscopic Techniques**

Time resolved optical spectroscopy and some other techniques with femtosecond laser were performed to investigate the ultrafast dynamics and nonlinear optical properties of GO and noble metal nanoparticles in this thesis. A brief description of these techniques is presented in this section.

### **1.5.1 Pump-probe and transient absorption spectroscopy**

Pump-probe technique is the most popular and versatile method used in spectroscopic measurement in time domain, which provides the effective information

about the electronic dynamics occurred in the measured sample. More importantly, pump-probe technique is suitable for most types of samples and the layout can be easily modified for some specific purposes. Basically, there are two laser pulses in pump-probe technique. As identified in its name, one is the pump beam, and the other one is the probe beam. The pump pulse excites the samples at a given wavelength and the probe pulse with a various delay time overlaps spatially with pump beam within the sample. The absorption or transmittance of probe pulse is monitored at various delay time. By comparison of probe spectra with pump and without pump (transient transmittance change:  $\Delta T/T$ ), it is possible to achieve the information about the excited molecules or transient species in the systems at a specific given delay time. Time resolved information about the kinetics of these molecules can be obtained by measuring at various delays at a fixed probe wavelength.

For common pump-probe technique, both pump and probe pulses can be identical or different, which should be specifically designed for different purposes. But for transient absorption measurement, the probe pulse should be a broadband source with a broad range of wavelength. In our experiment, to achieve both the transient absorption spectra and single wavelength dynamics, a white light continuum generated by 800 nm femtosecond laser was used as the probe beam. The detailed layout is described in Figure 1.9a and the spectrum of white light is shown in Figure 1.9b. In our experimental setup, a Ti:sapphire oscillator seeded regenerative amplifier



laser system with output pulse energy of 2 mJ at 800 nm and a repetition rate of 1 kHz was used as the source of the pump and probe beams. The 800 nm laser beam was split into two portions. One portion acts as the pump beam (for 800 nm excitation) or passes through a BBO crystal to generate the 400 nm pump beam by SHG (for 400 nm excitation). The other portion of the 800 nm beam was used to generate white light continuum in a 1 mm sapphire plate. The white light beam was split into two portions: probe and reference. The pump beam was focused onto the sample with a beam size of 300  $\mu\text{m}$  in diameter and overlapped with the smaller probe beam (100  $\mu\text{m}$  in diameter). The probe beam is collected after passing through the sample and its intensity is monitored by a photodiode as the detector. Both the detectors of probe and reference are connected to the lock-in amplifier to correct the pulse to pulse intensity fluctuations. The time delay between the pump and probe pulse was varied by a computer-controlled translation stage. The pump beam was modulated by an optical chopper at a frequency of 500 Hz. In a single wavelength dynamics scan, a fixed probe wavelength was picked and the transmittance change of probe with pump and without pump ( $\Delta T/T$ ) was monitored as a function of the various delay between the pump and probe beam. The transient absorption spectra at fixed time delays were measured by passing the probe beam through a monochromator before detector.

It should be noticed that the pulse duration of the pump and probe pulses must be shorter than the timescale of the dynamics measured. The time resolution of this system is determined by both the duration of the pump and probe pulses and the step of motion

control over the time delay between the pump and probe pulses by a translation stage

( $1\text{fs} = 0.15\ \mu\text{m}$ ).

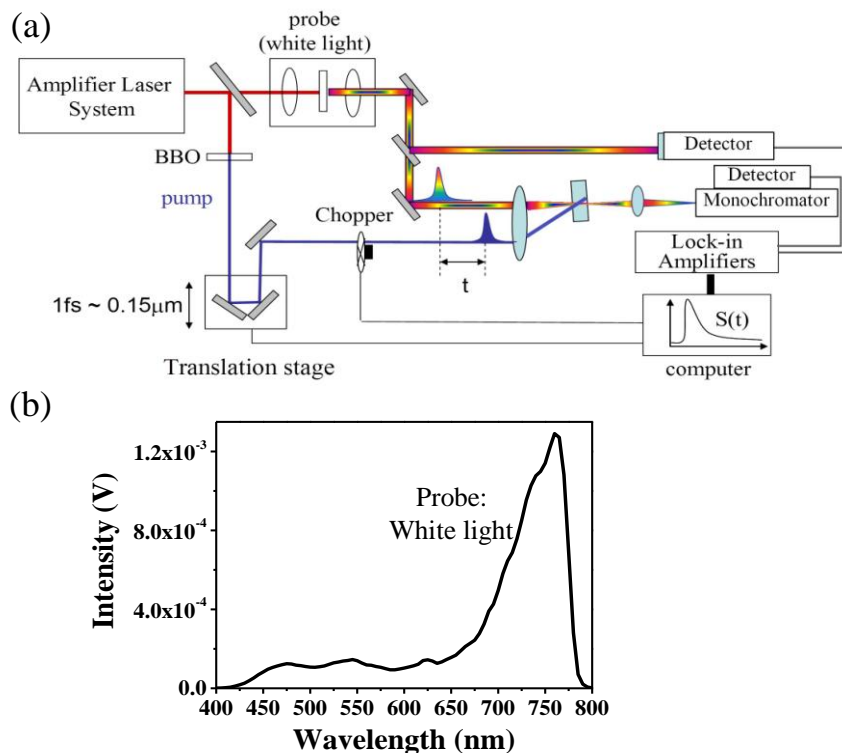


**Figure 1.9:** (a) Experimental setup of pump-probe and transient absorption spectroscopy. (b) Spectrum of white light continuum as probe beam measured by detector (Silicon Photodiode). The unit is voltage (V).

### 1.5.2 Two-pulse emission modulation spectroscopy

The two-pulse emission modulation experiment was designed based on the pump-probe technique. In this technique, the same laser pulses generated from a mode-locked Ti:sapphire oscillator seeded regenerative amplifier with an output at 800 nm and a repetition rate of 1 kHz were employed. The 800 nm laser beam was attenuated by neutral density filters before splitting into two portions of approximately equal intensities. The two laser beams were focused onto the sample and spatially overlapped. One beam was modulated by an optical chopper at a frequency of 500 Hz.

The time delay between these two pulse replicas was varied by a computer-controlled translation stage. The emission signals were collected by a Photomultiplier tubes (PMT) attached to a monochromator. The emission signals are recorded as a function of the time delay of the two pulses. The detailed experimental setup is illustrated in Figure 1.10.

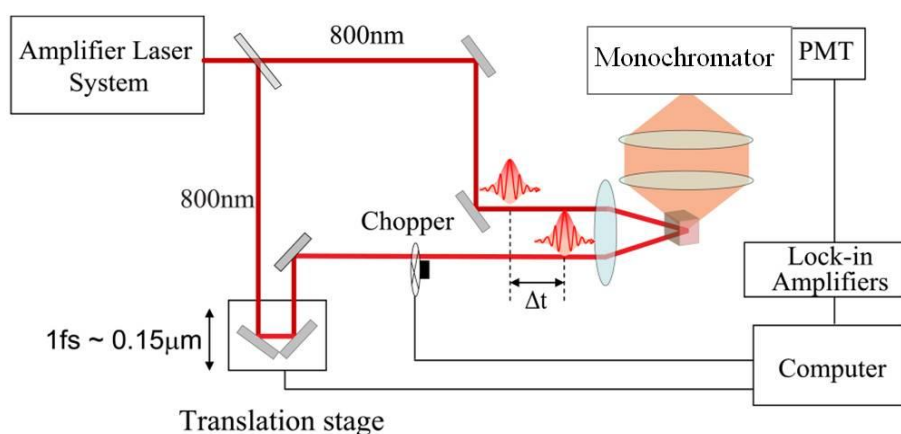


**Figure 1.10:** Experimental setup of two-pulse emission modulation spectroscopy.

### 1.5.3 Two-photon photoluminescence and lifetime measurement

Fluorescence lifetime is another important time-resolved spectroscopic measurement, which provides the kinetic information of radiative relaxation processes. The TPPL spectra and lifetime measurement is similar to the steady state (one-photon) PL spectra and lifetime measurement. Based on the different excitation mechanisms between two-photon and one-photon excitation, there are only two points of differences in the measurement: the excitation source and emission filter used.

The experimental setup is illustrated in Figure 1.11. In our experiment, the

emission spectrum of sample excited by the simultaneous absorption of two photons was measured. The excitation source was a femtosecond (fs) Ti:sapphire oscillator with an output at a central wavelength tunable from 750 to 840 nm with pulse duration of 80 fs and a repetition rate of 84.5 MHz. The laser beam was split into two portions. The strong portion was focused onto the samples using a lens with a focal length of 30 mm as excitation. The weak portion was detected by a fast photodiode for offering an electronic trigger for lifetime measurement.

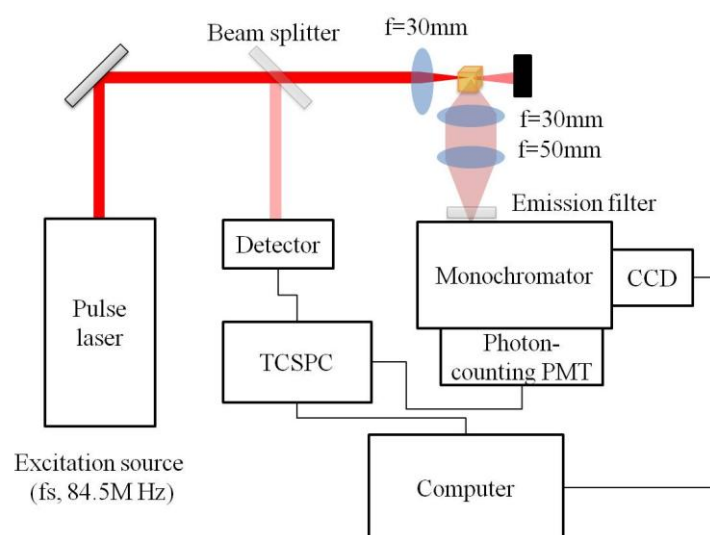


**Figure 1.11:** Experimental setup of two-photon photoluminescence and lifetime measurement.

The emission was collected at the direction perpendicular to the excitation beam to minimize the scattering. The emission signal was collected by an optical fiber or directly collected into a two port monochromator. A 750 nm short pass filter was placed before the monochromator to further minimize the scattering from the excitation light. One port of monochromator is attached with a charge coupled device (CCD) with thermoelectric cooling (down to  $-80\text{ }^{\circ}\text{C}$ ) to measure the TPPL spectra.

The other port is connected by a photon counting mode PMT following a time correlated single photon counting (TCSPC) device. For the fluorescence lifetime, the time resolution of this experiment is determined by not only the pulse duration of the excitation but also the response of the photon counting detector.

#### 1.5.4 Open-aperture Z-scan technique

As of now, many efforts have been devoted to characterize the nonlinear optical materials as well as understand the mechanisms of nonlinear optical properties in various nanostructures. Z-scan measurement is a simple technique for measuring third-order nonlinearities firstly introduced by M.Sheik-Bahae et al. in 1990.<sup>126</sup> Because of its simplicity, sensitivity, accuracy, open-aperture Z-scan measurement was widely used to characterize multiphoton absorption coefficient of the nonlinear optical materials. In this technique, as shown in Figure 1.12a, the transmittance through a nonlinear medium was measured as the sample travelling through the focus of a Gaussian beam (i.e.  $z = 0$ ,  $z$  is the focal distance). Information on nonlinear optical absorption was obtained by collecting all the transmitted energy. The normalized energy transmittance can be expressed as

$$T(z) = \frac{1}{\sqrt{\pi}q_0(z,0)} \int_{-\infty}^{\infty} \ln \left[ 1 + q_0(z,0)e^{-t^2} \right] dt, \quad 1.7$$

where  $I_0$  is the on-axis irradiance at focus point,

$$q_0(z,0) = \beta I_0(0)L_{eff} / \left( 1 + \frac{z^2}{z_0^2} \right), \quad 1.8$$

in which  $z_0 = \frac{kw_0^2}{2}$  is the diffraction length and  $w_0$  is the waist of the Gaussian beam. A typical open aperture Z-scan transmittance curve resulted from TPA is present in Figure 1.12b. The TPA coefficient  $\beta$  can be determined by fitting the experimental data by equation 1.7.

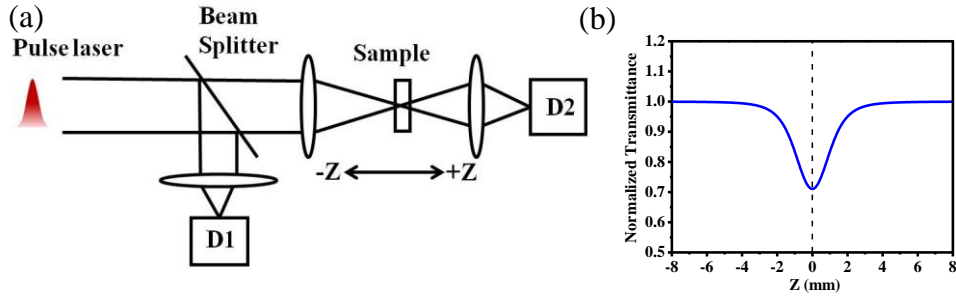


**Figure 1.12:** (a) Experimental setup of the Z-scan measurement. D1 and D2: photodiodes. (b) Typical 2PA open aperture Z-scan curve.

## 1.6 Thesis Outline

Having provided a brief introduction of background and motivation of this thesis, basic information about the nonlinear optical properties of our studying material as well as some ultrafast spectroscopic techniques related to our work, an outline of the research conducted in this thesis is given in this section.

In Chapter 2, we designed and performed two-pulse emission modulation (TPEM) and pump-probe measurements to investigate the excitation nature of TPPL in Au NRs and coupled Au nanospheres (Au NSs). As mentioned in the above section, the decay time of TPPL cross contribution carries obvious evidence to differentiate two excitation mechanisms of TPPL: coherent two-photon absorption or two sequential one photon absorption steps. So in this study, Three samples: Fluorescein, Au NRs and Au

NSs aggregates in aqueous solution were prepared and measured by TPPEM technique. Fluorescein is a standard two-photon absorption organic dye, which shares the coherent two-photon absorption mechanism for their excitation process. The comparison of these TPPEM results on these three samples may provide useful information for revealing their true excitation nature of TPPL. The results are also important for exploring the observed aggregation induced enhancement mechanism in coupled nanostructures.

Au NRs studied in Chapter 2 are in aqueous solution, which is also the most common condition in previous reports. In Chapter 3, PEG-SH capped Au NRs well dispersed in various organic solvents were prepared, and the solvent effects on the TPPL properties and ultrafast excitation dynamics of Au NRs were explored by the ultrafast time-resolved transient absorption and pump-probe measurements. The TPPL intensities of Au NRs in different organic solvents were found to be significantly quenched than that of Au NRs in H<sub>2</sub>O. Their corresponding quenching mechanisms were investigated by the excited carrier relaxation behaviors of Au NRs in H<sub>2</sub>O and organic solvents. This study might provide some useful information on fundamental understanding the TPPL properties as well as development of various potential biological applications of Au NRs based on the environment dependent TPPL intensity variation.

In Chapter 4, the pump-probe and transient absorption spectroscopy measurements were utilized to investigate the broadband ultrafast carrier relaxation

dynamics of GO and reduced GO. GO is an excellent platform for nanocomposites and also has its own fascinating nonlinear optical properties based on the tunable bandgap by controlling the degree of reduction. According to the different size distributions of  $sp^2$  domains before and after reduction, GO and reduced GO may have different nonlinear optical properties. So in this study, GO solution, GO films, as well as reduced GO films via high temperature annealing were prepared to investigate their different transient absorption responses over the broad range of probe wavelengths.

In Chapter 5, we further investigate the nonlinear optical properties of GO and reduced GO thin films and their optical limiting activity with femtosecond laser pulses at 800 and 400 nm. By employing open aperture Z-scan technique, the nonlinear absorption coefficients such as two-photon and three-photon absorption coefficients of GO films with different thickness on glass substrate were measured. Through controlling the exposure time of chemical and laser irradiation reduction, GO film were partially reduced at different degree of reduction. These optical limiting behaviors of these as-prepared, partially reduced and totally reduced GO films were systemically studied. Moreover, GO thin films were also fabricated on flexible plastic substrates by using solution processing methods on a large scale, and their nonlinear optical properties were also characterized.

Finally, conclusions and outlook are given in Chapter 6.



## References

- (1) Maiman, T.H. *Nature* **1960**, *187*, 493-494.
- (2) Hargrove, L.E., Fork, R.L. and Pollack, M.A. *Appl. Phys. Lett.* **1964**, *5*, 4-5.
- (3) Stetser, D.A. and DeMaria, A.J. *Appl. Phys. Lett.* **1966**, *9*, 118-120.
- (4) Spence, D.E., Kean, P.N. and Sibbett, W. *Opt. Lett.* **1991**, *16*, 42-44.
- (5) Ell, R., Morgner, U., Kärtner, F., Fujimoto, J.G., Ippen, E.P., Scheuer, V., Angelow, G., Tschudi, T., Lederer, M.J. and Boiko, A. *Opt. Lett.* **2001**, *26*, 373-375.
- (6) Maine, P., Strickland, D., Bado, P., Pessot, M. and Mourou, G. *IEEE J. Quantum Electron.* **1988**, *24*, 398-403.
- (7) Myers, L.E., Eckardt, R., Fejer, M., Byer, R., Bosenberg, W. and Pierce, J. *J. Opt. Soc. Am. B* **1995**, *12*, 2102-2116.
- (8) Cerullo, G., Nisoli, M., Stagira, S. and De Silvestri, S. *Opt. Lett.* **1998**, *23*, 1283-1285.
- (9) Woutersen, S., Emmerichs, U. and Bakker, H. *Science* **1997**, *278*, 658-660.
- (10) Scholes, G.D., Larsen, D.S., Fleming, G.R., Rumbles, G. and Burn, P.L. *Phys. Rev. B* **2000**, *61*, 13670.
- (11) Noguez, C. *J. Phys. Chem. C* **2007**, *111*, 3806-3819.
- (12) Ghosh, S.K. and Pal, T. *Chem. Rev.* **2007**, *107*, 4797-4862.
- (13) Göppert-Mayer, M. *Annalen der Physik* **1931**, *401*, 273-294.
- (14) Kaiser, W. and Garrett, C.G.B. *Phys. Rev. Lett.* **1961**, *7*, 229-231.
- (15) Bohren, C.F. and Huffman, D.R., *Absorption and scattering of light by small particles*. 2008: John Wiley & Sons.
- (16) Nie, S. and Emory, S.R. *Science* **1997**, *275*, 1102-1106.
- (17) Aslan, K. and Geddes, C.D. *Chem. Soc. Rev.* **2009**, *38*, 2556-2564.
- (18) Mooradian, A. *Phys. Rev. Lett.* **1969**, *22*, 185-187.
- (19) Boyd, G.T., Yu, Z.H. and Shen, Y.R. *Phys. Rev. B* **1986**, *33*, 7923-7936.
- (20) Apell, P., Monreal, R. and Lundqvist, S. *Phys. Scr.* **1988**, *38*, 174.
- (21) Beversluis, M.R., Bouhelier, A. and Novotny, L. *Phys. Rev. B* **2003**, *68*, 115433.
- (22) Varnavski, O.P., Mohamed, M.B., El-Sayed, M.A. and Goodson, T. *J. Phys. Chem. B* **2003**, *107*, 3101-3104.
- (23) Drachev, V.P., Khaliullin, E.N., Kim, W., Alzoubi, F., Rautian, S.G., Safonov,

- V.P., Armstrong, R.L. and Shalaev, V.M. *Phys. Rev. B* **2004**, *69*, 035318.
- (24) Wang, H., Huff, T.B., Zweifel, D.A., He, W., Low, P.S., Wei, A. and Cheng, J.-X. *Proc. Natl. Acad. Sci. U. S. A.* **2005**, *102*, 15752-15756.
- (25) Li, J.L., Day, D. and Gu, M. *Adv. Mater.* **2008**, *20*, 3866-3871.
- (26) Durr, N.J., Larson, T., Smith, D.K., Korgel, B.A., Sokolov, K. and Ben-Yakar, A. *Nano Lett.* **2007**, *7*, 941-945.
- (27) Dulkeith, E., Niedereichholz, T., Klar, T.A., Feldmann, J., von Plessen, G., Gittins, D.I., Mayya, K.S. and Caruso, F. *Phys. Rev. B* **2004**, *70*, 205424.
- (28) Imura, K., Nagahara, T. and Okamoto, H. *J. Am. Chem. Soc.* **2004**, *126*, 12730-12731.
- (29) Bouhelier, A., Bachelot, R., Lerondel, G., Kostcheev, S., Royer, P. and Wiederrecht, G.P. *Phys. Rev. Lett.* **2005**, *95*, 267405.
- (30) Grubisic, A., Schweikhard, V., Baker, T.A. and Nesbitt, D.J. *ACS Nano* **2012**, *7*, 87-99.
- (31) Yorulmaz, M., Khatua, S., Zijlstra, P., Gaiduk, A. and Orrit, M. *Nano Lett.* **2012**, *12*, 4385-4391.
- (32) Huang, J., Wang, W., Murphy, C.J. and Cahill, D.G. *Proc. Natl. Acad. Sci. U. S. A.* **2014**, *111*, 906-911.
- (33) Imura, K., Nagahara, T. and Okamoto, H. *J. Phys. Chem. B* **2005**, *109*, 13214-13220.
- (34) Biagioni, P., Celebrano, M., Savoini, M., Grancini, G., Brida, D., M á ě ě i-Tempfli, S., M á ě ě i-Tempfli, M., Du ò L., Hecht, B., Cerullo, G. and Finazzi, M. *Phys. Rev. B* **2009**, *80*, 045411.
- (35) Biagioni, P., Brida, D., Huang, J.-S., Kern, J., Du ò L., Hecht, B., Finazzi, M. and Cerullo, G. *Nano Lett.* **2012**, *12*, 2941-2947.
- (36) Hartland, G.V. *Chem. Rev.* **2011**, *111*, 3858-3887.
- (37) Link, S., Burda, C., Mohamed, M.B., Nikoobakht, B. and El-Sayed, M.A. *Phys. Rev. B* **2000**, *61*, 6086-6090.
- (38) Zijlstra, P., Tchebotareva, A.L., Chon, J.W.M., Gu, M. and Orrit, M. *Nano Lett.* **2008**, *8*, 3493-3497.
- (39) Voisin, C., Christofilos, D., Loukakos, P.A., Del Fatti, N., Vall é e, F., Lerm é J., Gaudry, M., Cottancin, E., Pellarin, M. and Broyer, M. *Phys. Rev. B* **2004**, *69*, 195416.
- (40) Schoenlein, R.W., Lin, W.Z., Fujimoto, J.G. and Eesley, G.L. *Phys. Rev. Lett.* **1987**, *58*, 1680-1683.
- (41) Staleva, H. and Hartland, G.V. *J. Phys. Chem. C* **2008**, *112*, 7535-7539.

- (42) Voisin, C., Del Fatti, N., Christofilos, D. and Vallée, F. *J. Phys. Chem. B* **2001**, *105*, 2264-2280.
- (43) Doremus, R. *J. Chem. Phys.* **1965**, *42*, 414-417.
- (44) Doremus, R.H. *J. Chem. Phys.* **1964**, *40*, 2389-2396.
- (45) Sönnichsen, C., Franzl, T., Wilk, T., von Plessen, G., Feldmann, J., Wilson, O. and Mulvaney, P. *Phys. Rev. Lett.* **2002**, *88*, 077402.
- (46) Del Fatti, N., Vallée, F., Flytzanis, C., Hamanaka, Y. and Nakamura, A. *Chem. Phys.* **2000**, *251*, 215-226.
- (47) Halté V., Guille, J., Merle, J.C., Perakis, I. and Bigot, J.Y. *Phys. Rev. B* **1999**, *60*, 11738-11746.
- (48) Hodak, J.H., Henglein, A. and Hartland, G.V. *J. Chem. Phys.* **2000**, *112*, 5942-5947.
- (49) Huang, J., Park, J., Wang, W., Murphy, C.J. and Cahill, D.G. *ACS Nano* **2012**, *7*, 589-597.
- (50) Inouye, H., Tanaka, K., Tanahashi, I. and Hirao, K. *Phys. Rev. B* **1998**, *57*, 11334-11340.
- (51) Jiang, Y., Wang, H.-Y., Xie, L.-P., Gao, B.-R., Wang, L., Zhang, X.-L., Chen, Q.-D., Yang, H., Song, H.-W. and Sun, H.-B. *J. Phys. Chem. C* **2010**, *114*, 2913-2917.
- (52) Hu, M. and Hartland, G.V. *J. Phys. Chem. B* **2002**, *106*, 7029-7033.
- (53) Zijlstra, P. and Orrit, M. *Rep. Prog. Phys.* **2011**, *74*, 106401.
- (54) Sun, C.K., Vallée, F., Acioli, L.H., Ippen, E.P. and Fujimoto, J.G. *Phys. Rev. B* **1994**, *50*, 15337-15348.
- (55) Yu, K., Polavarapu, L. and Xu, Q.-H. *J. Phys. Chem. A* **2011**, *115*, 3820-3826.
- (56) Hartland, G.V. *Annu. Rev. Phys. Chem.* **2006**, *57*, 403-430.
- (57) Hodak, J.H., Henglein, A. and Hartland, G.V. *J. Phys. Chem. B* **2000**, *104*, 5053-5055.
- (58) Nisoli, M., De Silvestri, S., Cavalleri, A., Malvezzi, A.M., Stella, A., Lanzani, G., Cheyssac, P. and Kofman, R. *Phys. Rev. B* **1997**, *55*, R13424-R13427.
- (59) Novoselov, K.S., Geim, A.K., Morozov, S.V., Jiang, D., Katsnelson, M.I., Grigorieva, I.V., Dubonos, S.V. and Firsov, A.A. *Nature* **2005**, *438*, 197-200.
- (60) Geim, A.K. and Novoselov, K.S. *Nat. Mater.* **2007**, *6*, 183-191.
- (61) Bo, Z., Shuai, X., Mao, S., Yang, H., Qian, J., Chen, J., Yan, J. and Cen, K. *Sci. Rep.* **2014**, *4*.
- (62) Berger, C., Song, Z., Li, X., Wu, X., Brown, N., Naud, C., Mayou, D., Li, T.,

- Hass, J., Marchenkov, A.N., Conrad, E.H., First, P.N. and de Heer, W.A. *Science* **2006**, *312*, 1191-1196.
- (63) Reina, A., Jia, X.T., Ho, J., Nezich, D., Son, H.B., Bulovic, V., Dresselhaus, M.S. and Kong, J. *Nano Lett.* **2009**, *9*, 30-35.
- (64) Novoselov, K.S., Geim, A.K., Morozov, S.V., Jiang, D., Zhang, Y., Dubonos, S.V., Grigorieva, I.V. and Firsov, A.A. *Science* **2004**, *306*, 666-669.
- (65) Li, X.L., Zhang, G.Y., Bai, X.D., Sun, X.M., Wang, X.R., Wang, E. and Dai, H.J. *Nat. Nanotechnol.* **2008**, *3*, 538-542.
- (66) Hernandez, Y., Nicolosi, V., Lotya, M., Blighe, F.M., Sun, Z.Y., De, S., McGovern, I.T., Holland, B., Byrne, M., Gun'ko, Y.K., Boland, J.J., Niraj, P., Duesberg, G., Krishnamurthy, S., Goodhue, R., Hutchison, J., Scardaci, V., Ferrari, A.C. and Coleman, J.N. *Nat. Nanotechnol.* **2008**, *3*, 563-568.
- (67) Kosynkin, D.V., Higginbotham, A.L., Sinitskii, A., Lomeda, J.R., Dimiev, A., Price, B.K. and Tour, J.M. *Nature* **2009**, *458*, 872-876.
- (68) Becerril, H.A., Mao, J., Liu, Z., Stoltenberg, R.M., Bao, Z. and Chen, Y. *ACS Nano* **2008**, *2*, 463-470.
- (69) Eda, G., Fanchini, G. and Chhowalla, M. *Nat. Nanotechnol.* **2008**, *3*, 270-274.
- (70) Li, D., Muller, M.B., Gilje, S., Kaner, R.B. and Wallace, G.G. *Nat. Nanotechnol.* **2008**, *3*, 101-105.
- (71) Hummers, W.S. and Offeman, R.E. *J. Am. Chem. Soc.* **1958**, *80*, 1339-1339.
- (72) Compton, O.C. and Nguyen, S.T. *Small* **2010**, *6*, 711-723.
- (73) Huang, X., Qi, X., Boey, F. and Zhang, H. *Chem. Soc. Rev.* **2012**, *41*, 666-686.
- (74) Brodie, B.C. *Phil. Trans. R. Soc. Lond. A* **1859**, *149*, 249-259.
- (75) Mattevi, C., Eda, G., Agnoli, S., Miller, S., Mkhoyan, K.A., Celik, O., Mastrogiovanni, D., Granozzi, G., Garfunkel, E. and Chhowalla, M. *Adv. Funct. Mater.* **2009**, *19*, 2577-2583.
- (76) Kudin, K.N., Ozbas, B., Schniepp, H.C., Prud'homme, R.K., Aksay, I.A. and Car, R. *Nano Lett.* **2007**, *8*, 36-41.
- (77) Gómez-Navarro, C., Meyer, J.C., Sundaram, R.S., Chuvilin, A., Kurasch, S., Burghard, M., Kern, K. and Kaiser, U. *Nano Lett.* **2010**, *10*, 1144-1148.
- (78) Wilson, N.R., Pandey, P.A., Beanland, R., Young, R.J., Kinloch, I.A., Gong, L., Liu, Z., Suenaga, K., Rourke, J.P., York, S.J. and Sloan, J. *ACS Nano* **2009**, *3*, 2547-2556.
- (79) Dreyer, D.R., Park, S., Bielawski, C.W. and Ruoff, R.S. *Chem. Soc. Rev.* **2010**, *39*, 228-240.
- (80) Stankovich, S., Piner, R.D., Nguyen, S.T. and Ruoff, R.S. *Carbon* **2006**, *44*,

3342-3347.

- (81) Paredes, J.I., Villar-Rodil, S., Solís-Fernández, P., Martínez-Alonso, A. and Tascón, J.M.D. *Langmuir* **2009**, *25*, 5957-5968.
- (82) Ishigami, M., Chen, J.H., Cullen, W.G., Fuhrer, M.S. and Williams, E.D. *Nano Lett.* **2007**, *7*, 1643-1648.
- (83) Stankovich, S., Dikin, D.A., Piner, R.D., Kohlhaas, K.A., Kleinhammes, A., Jia, Y., Wu, Y., Nguyen, S.T. and Ruoff, R.S. *Carbon* **2007**, *45*, 1558-1565.
- (84) Jung, I., Vaupel, M., Pelton, M., Piner, R., Dikin, D.A., Stankovich, S., An, J. and Ruoff, R.S. *J. Phys. Chem. C* **2008**, *112*, 8499-8506.
- (85) Robertson, J. and O'Reilly, E.P. *Phys. Rev. B* **1987**, *35*, 2946-2957.
- (86) Robertson, J. *Phys. Rev. B* **1996**, *53*, 16302-16305.
- (87) Eda, G., Lin, Y.Y., Mattevi, C., Yamaguchi, H., Chen, H.A., Chen, I.S., Chen, C.W. and Chhowalla, M. *Adv. Mater.* **2010**, *22*, 505-509.
- (88) Gilje, S., Han, S., Wang, M., Wang, K.L. and Kaner, R.B. *Nano Lett.* **2007**, *7*, 3394-3398.
- (89) Ekiz, O.O.n., Ürel, M., Güner, H., Mizrak, A.K. and Dâna, A. *ACS Nano* **2011**, *5*, 2475-2482.
- (90) Abdelsayed, V., Moussa, S., Hassan, H.M., Aluri, H.S., Collinson, M.M. and El-Shall, M.S. *J. Phys. Chem. Lett.* **2010**, *1*, 2804-2809.
- (91) Zhang, Y., Guo, L., Wei, S., He, Y., Xia, H., Chen, Q., Sun, H.-B. and Xiao, F.-S. *Nano Today* **2010**, *5*, 15-20.
- (92) Matsumoto, Y., Koinuma, M., Ida, S., Hayami, S., Taniguchi, T., Hatakeyama, K., Tateishi, H., Watanabe, Y. and Amano, S. *J. Phys. Chem. C.* **2011**, *115*, 19280-19286.
- (93) Cuong, T.V., Pham, V.H., Shin, E.W., Chung, J.S., Hur, S.H., Kim, E.J., Tran, Q.T., Nguyen, H.H. and Kohl, P.A. *Appl. Phys. Lett.* **2011**, *99*, 041905.
- (94) Lee, B.R., Kim, J.-w., Kang, D., Lee, D.W., Ko, S.-J., Lee, H.J., Lee, C.-L., Kim, J.Y., Shin, H.S. and Song, M.H. *ACS Nano* **2012**, *6*, 2984-2991.
- (95) Xiang, Q., Yu, J. and Jaroniec, M. *J. Am. Chem. Soc.* **2012**, *134*, 6575-6578.
- (96) Wang, Y., Li, Z., Hu, D., Lin, C.-T., Li, J. and Lin, Y. *J. Am. Chem. Soc.* **2010**, *132*, 9274-9276.
- (97) Lee, Y.H., Polavarapu, L., Gao, N., Yuan, P. and Xu, Q.-H. *Langmuir* **2011**, *28*, 321-326.
- (98) Breusing, M., Ropers, C. and Elsaesser, T. *Phys. Rev. Lett.* **2009**, *102*, 086809.
- (99) Dawlaty, J.M., Shivaraman, S., Chandrashekhara, M., Rana, F. and Spencer,

- M.G. *Appl. Phys. Lett.* **2008**, *92*, 042116.
- (100) Huang, L.B., Hartland, G.V., Chu, L.Q., Luxmi, Feenstra, R.M., Lian, C.X., Tahy, K. and Xing, H.L. *Nano Lett.* **2010**, *10*, 1308-1313.
- (101) Obraztsov, P.A.O.P.A., Rybin, M.G., Tyurnina, A.V., Garnov, S.V., Obraztsova, E.D., Obraztsov, A.N. and Svirko, Y.P. *Nano Lett.* **2011**, *11*, 1540-1545.
- (102) Shang, J., Yu, T., Lin, J. and Gurzadyan, G.G. *ACS Nano* **2011**, *5*, 3278-3283.
- (103) Ruzicka, B.A., Werake, L.K., Zhao, H., Wang, S. and Loh, K.P. *Appl. Phys. Lett.* **2010**, *96*, 173106.
- (104) Ruzicka, B.A., Kumar, N., Wang, S., Loh, K.P. and Zhao, H. *J. Appl. Phys.* **2011**, *109*, 084322.
- (105) Kumar, S., Anija, M., Kamaraju, N., Vasu, K.S., Subrahmanyam, K.S., Sood, A.K. and Rao, C.N.R. *Appl. Phys. Lett.* **2009**, *95*, 191911.
- (106) Liu, Z.B., Zhao, X., Zhang, X.L., Yan, X.Q., Wu, Y.P., Chen, Y.S. and Tian, J.G. *J. Phys. Chem. Lett.* **2011**, *2*, 1972-1977.
- (107) Stranks, S.D., Weisspfenig, C., Parkinson, P., Johnston, M.B., Herz, L.M. and Nicholas, R.J. *Nano Lett.* **2011**, *11*.
- (108) Dean, J.J. and Driel, H.M.v. *Appl. Phys. Lett.* **2009**, *95*, 261910.
- (109) Bao, Q., Zhang, H., Ni, Z., Wang, Y., Polavarapu, L., Shen, Z., Xu, Q.-H., Tang, D. and Loh, K. *Nano Res.* **2011**, *4*, 297-307.
- (110) Zhang, H., Virally, S., Bao, Q., Kian Ping, L., Massar, S., Godbout, N. and Kockaert, P. *Opt. Lett.* **2012**, *37*, 1856-1858.
- (111) Liu, Z.-B., Zhao, X., Zhang, X.-L., Yan, X.-Q., Wu, Y.-P., Chen, Y.-S. and Tian, J.-G. *J. Phys. Chem. Lett.* **2011**, 1972-1977.
- (112) Bonaccorso, F., Sun, Z., Hasan, T. and Ferrari, A.C. *Nat. Photonics* **2010**, *4*, 611-622.
- (113) Feng, M., Zhan, H.B. and Chen, Y. *Appl. Phys. Lett.* **2010**, *96*, 033107.
- (114) Gu, B., Huang, X.Q., Tan, S.Q., Wang, M. and Ji, W. *Appl. Phys. B: Laser O* **2009**, *95*, 375-381.
- (115) Polavarapu, L., Venkatram, N., Ji, W. and Xu, Q.H. *ACS Appl. Mater. Interfaces* **2009**, *1*, 2298-2303.
- (116) Francois, L., Mostafavi, M., Belloni, J. and Delaire, J.A. *Phys. Chem. Chem. Phys.* **2001**, *3*, 4965-4971.
- (117) He, G.S., Tan, L.S., Zheng, Q. and Prasad, P.N. *Chem. Rev.* **2008**, *108*, 1245-1330.
- (118) Calvete, M., Yang, G.Y. and Hanack, M. *Synth. Met.* **2004**, *141*, 231-243.

- (119) Sun, Z., Hasan, T., Torrisi, F., Popa, D., Privitera, G., Wang, F., Bonaccorso, F., Basko, D.M. and Ferrari, A.C. *ACS Nano* **2010**, *4*, 803-810.
- (120) Zhang, H., Tang, D., Zhao, L., Bao, Q. and Loh, K. *Opt. Express* **2009**, *17*, 17630-17635.
- (121) Xing, G., Guo, H., Zhang, X., Sum, T.C. and Huan, C.H.A. *Opt. Express* **2010**, *18*, 4564-4573.
- (122) Muszynski, R., Seger, B. and Kamat, P.V. *J. Phys. Chem. C* **2008**, *112*, 5263-5266.
- (123) Gao, Y., Zhang, X., Li, Y., Liu, H., Wang, Y., Chang, Q., Jiao, W. and Song, Y. *Opt. Commun.* **2005**, *251*, 429-433.
- (124) Luo, S., Chen, Y., Fan, G., Sun, F. and Qu, S. *Appl. Phys. A* **2014**, 1-4.
- (125) Lee, Y.H., Yan, Y., Polavarapu, L. and Xu, Q.-H. *Appl. Phys. Lett.* **2009**, *95*, 023105-023105-3.
- (126) Sheik-Bahae, M., Said, A.A., Wei, T.H., Hagan, D.J. and Van Stryland, E.W. *IEEE J. Quantum Electron.* **1990**, *26*, 760-769.

# **Chapter 2. Excitation Nature of Two-Photon Photoluminescence of Gold Nanorods and Coupled Gold Nanoparticles Studied by Two-pulse Emission Modulation Spectroscopy**

## **2.1 Introduction**

Noble metal nanoparticles have attracted lots of scientific interests because of their unique optical properties<sup>1-3</sup> and wide applications in various fields such as bio-imaging,<sup>4</sup> sensing,<sup>5, 6</sup> and nonlinear optics.<sup>7-9</sup> In particular, metal nanoparticles display localized surface plasmon resonance (LSPR), which arises from collective oscillation of conduction band electrons. The LSPR frequency can be tuned by the particle size, shape, refractive index and inter-particle plasmon coupling.<sup>10-14</sup> The strong local field induced by plasmon resonance has been widely utilized to amplify various optical signals such as Raman scattering and fluorescence.<sup>15-19</sup> Plasmon coupling was known to dramatically enhance local electrical fields within the gap region, which result in further enhancement in various linear and nonlinear optical signals.<sup>20-24</sup>

Au nanoparticles are generally known to display low emission quantum efficiency ( $10^{-6}$ ) under one-photon excitation.<sup>16, 25</sup> Au NRs and coupled nanostructures were recently observed to display strong two-photon photoluminescence (TPPL).<sup>21-24, 26, 27</sup> The observed strong TPPL can be attributed to enhanced local field arising from the



longitudinal plasmon resonance of these nanostructures at the wavelength range coincident with the excitation wavelength. Many efforts have been made to understand the excitation nature of strong TPPL in Au NRs,<sup>26, 28-34</sup> which is still under active debate. Two possible excitation mechanisms have been proposed to account for the observed strong TPPL in Au NRs: coherent two-photon absorption process or two sequential one-photon absorption processes. The coherent two-photon absorption model, which is commonly used for organic molecules, involves simultaneous absorption of two photons through a virtual intermediate state. The coherent two-photon absorption mechanism was proposed to account for TPPL in Au NRs and supported by the observation of a  $\cos^4\theta$  excitation polarization dependence of TPPL intensities of Au NRs.<sup>30-33</sup> The latter model assumes that the excitation process involves two sequential one-photon absorption steps that are mediated by real intermediate states. TPPL in Au NRs was believed to arise from recombination of electrons in the *sp* band with the holes in the *d* band, which were created by two sequential one-photon absorption transitions. The first photon induces *sp*→*sp* intraband transition to create a *sp* electron above the Fermi level. The second photon excites an electron from the *d* band to *sp* band through *d*→*sp* transition, which creates a hole in the *d* band. The hole in the *d* band and electron in the *sp* band can recombine radiatively to yield TPPL directly, or nonradiatively to emit particle plasmons that subsequently radiate to give rise to TPPL. The two sequential one-photon absorption model was initially proposed based on the observation of the  $\cos^2\theta$  excitation polarization dependence of TPPL in single Au

NRs,<sup>26</sup> which is contradictory from the previous observation.<sup>30, 32</sup> This model gained strong support from the work by Biagioni et al,<sup>28, 29</sup> who found that TPPL intensities of Au nanowires were insensitive to pulse duration for pulse widths of <1 ps.

As of now the excitation mechanisms for TPPL in Au NRs are not conclusive and need resolution. There are very few reports on the excitation mechanism for TPPL of coupled Au nanoparticles. In this work, we have performed femtosecond two-pulse emission modulation (TPEM) measurements on fluorescein, Au NRs and coupled Au NSs to understand the excitation mechanisms in Au NRs and coupled Au NSs. Fluorescein was used as the standard model system for coherent two-photon absorption. The decay profile of the cross contribution of TPEM measurements on fluorescein was found to closely follow the autocorrelation profile of the laser pulses (pulse duration of 60 fs). In contrast, the profiles of cross contribution of TPEM measurements on Au NRs and coupled Au NSs decay with much slower time constants compared to the autocorrelation profile of laser pulses. The decay time constants match well as the lifetimes of the intermediate states as measured from femtosecond pump-probe measurements. These results give unambiguous evidence that the observed TPPL in Au NRs and coupled Au NSs arise from two sequential one-photon absorption steps involving real intermediate states.

## **2.2 Experimental Section**

### **Preparation of Au nanospheres:**

Au nanospheres (Au NSs) with an average diameter of 45 nm are prepared by citrate reduction of  $\text{HAuCl}_4$ .<sup>35</sup> Briefly, 1.5 mg  $\text{HAuCl}_4$  was dissolved in 15 mL of  $\text{H}_2\text{O}$  and brought to boiling followed by addition of 0.12 mL of 1% sodium citrate solution. In ~30s the boiling solution turns faintly blue (nucleation) and the blue color suddenly changes into a brilliant red after ~1 min, indicating formation of spherical Au particles.

#### **Preparation of Au nanorods:**

Au nanorods (Au NRs) were prepared according to a previously reported seed-mediated growth method.<sup>36,37</sup> Gold seed solution was first prepared by mixing 5 mL of 0.1 M CTAB and 0.03 mL of 50 mM  $\text{HAuCl}_4$ . 0.1 mL portion of ice-cold 58 mM  $\text{NaBH}_4$  was then added, which resulted in formation of a brownish-yellow solution. This brownish-yellow solution was kept at room temperature for at least 2 hr. 0.2 mL of the gold seeds solution was subsequently added into the “growth solution” consisting of 100 mL of 0.1 M CTAB, 1.5 mL of 50 mM  $\text{HAuCl}_4$ , 0.224 mL of 50 mM  $\text{AgNO}_3$  and 1.5 mL of 0.08 M ascorbic acid. The reaction mixture was left undisturbed overnight. The obtained Au NRs were purified by washing with deionized water to remove excess CTAB and re-dispersed in 70 mL of deionized water.

The resulting Au NSs and Au NRs were utilized for various characterizations, TPPL and excitation dynamics measurements.

#### **Instrumentations and characterizations:**

Transmission electron microscopy (TEM) images of nanoparticles were taken

from a Philips CM10 TEM microscope (at an accelerating voltage of 100 kV). Ultraviolet-visible (UV-Vis) extinction spectra were measured by using a SHIMADZU UV-2550 spectrophotometer. The two-photon photoluminescence measurements were performed by using a Avesta TiF-100M femtosecond (fs) Ti:sapphire oscillator as the excitation source. The output laser pulses have a central wavelength of 800 nm with pulse duration of 80 fs and a repetition rate of 84.5 MHz. The laser beam was focused onto the samples using a lens with a focal length of 3.0 cm. The emission was collected at an angle of  $90^\circ$  to the direction of the excitation beam to minimize the scattering. The emission signal was directed into a CCD (Princeton Instruments, Pixis 100B) coupled monochromator (Acton, Spectra Pro 2300i) with an optical fiber. A 750 nm short pass filter was placed before the spectrometer to minimize the scattering from the excitation light.

#### **Two-pulse emission modulation experiment:**

The two-pulse emission modulation experiment was performed by the laser pulses generated from a mode-locked Ti:sapphire oscillator seeded regenerative amplifier (Spectra Physics), which gives an output with a pulse energy of 2.0 mJ at 800 nm and a repetition rate of 1 kHz. The 800 nm laser beam was attenuated by neutral density filters before splitting into two portions of approximately equal intensities. The two laser beams were focused onto the sample and spatially overlapped. One beam was modulated by an optical chopper at a frequency of 500 Hz. The time delay between these two pulse replicas was varied by a computer-controlled translation stage

(Newport, ESP 300). The TPPL signals in the 500 to 700 nm range were collected by a Photomultiplier tubes (Hamamatsu R928) attached to a monochromator (Acton SP-2150i, PI). The PL signals are recorded as a function of the time delay of the two pulses.

### **Pump-probe experiment:**

The pump-probe measurements were performed on Au NRs and coupled Au NSs by using the same femtosecond laser system. Briefly, the 800 nm laser beam was split into two portions. The larger portion of the beam was used as the pump beam. A residual portion of the beam was used to generate white light continuum (WLC) in a 1 mm sapphire plate. The WLC was split into two beams, one as probe and the other as a reference to correct for pulse-to-pulse intensity fluctuations. The signal and reference beams were detected by photodiodes that are connected to lock-in amplifiers and the computer. The pump beam is focused onto the film with a beam size of 300  $\mu\text{m}$  and overlaps with the smaller diameter (100  $\mu\text{m}$ ) probe beam. The delay between the pump and probe pulses was varied by a computer-controlled translation stage (Newport, ESP 300). The pump beam was modulated by an optical chopper at a frequency of 500 Hz. The variation transmittance at selected probe wavelength is recorded as a function of time delay between pump and probe pulses.

## 2.3 Localized Surface Plasmon Resonance of Coupled Au Nanospheres and Au Nanorods

The as-prepared isolated Au NSs with an average diameter of 45nm have a single LSPR band located at 532 nm presented in Figure 2.1. Cysteamine ( $\text{HS}(\text{CH}_2)_2\text{NH}_2$ ) was employed to induce the coupling of Au NSs due to its capability of binding to the gold surface through thiol and amine groups.<sup>38</sup> Addition of cysteamine into Au NSs solution resulted in a decrease of the original LSPR band at 532 nm, accompanied by the appearance of a new LSPR band at the longer wavelength range (650-1000 nm). This new band resembles the longitudinal LSPR mode of Au NRs, suggesting formation of anisotropic nano-aggregates. Formation of anisotropic nano-aggregates was further confirmed by the TEM images (Figure 2.1 insets), where a significant amount of linear nanochains and branched nanostructures were observed.

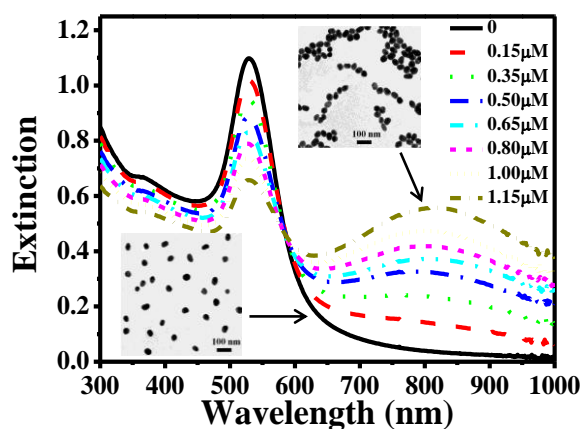


**Figure 2.1:** UV-Vis extinction spectrum of Au NSs in the presence of different amounts of cysteamine to induce the aggregation and plasmon coupling. The insets are the TEM images of isolated and coupled Au NSs.

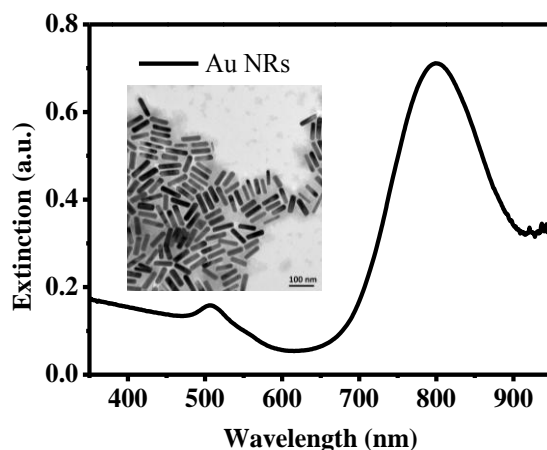


**Figure 2.2:** UV-Vis extinction spectra and TEM images (inset) of Au NRs.

The as-prepared Au NRs have average width and length of 19 and 74 nm, with an aspect ratio of 3.9. As shown in Figure 2.2, the extinction spectrum of Au NRs in deionized water exhibited a transverse LSPR band at 509 nm and a longitudinal LSPR band at 800nm, which shares the similar longitudinal LSPR and extinction spectra profile with coupled Au NSs.

## 2.4 Strong Two-Photon Photoluminescence of Coupled Au Nanospheres

TPPL spectra of the isolated and coupled Au NSs were measured by using femtosecond laser pulses with a central wavelength at 800 nm, repetition rate of 84.5 MHz as the excitation source. Under excitation with an incident power of 73 mW, TPPL intensity of the coupled Au NSs steadily increased upon gradual addition of cysteamine (Figure 2.3). TPPL enhancement of up to 57-fold was obtained when the concentration of cysteamine increased to 1.15  $\mu\text{M}$ . The log-log plot of the emission intensity at 650 nm of the coupled Au NSs (induced by 1.15  $\mu\text{M}$  of cysteamine) versus

excitation power (Figure 2.3 inset) gave a slope of 1.97, confirming that two photons were involved in the excitation process of the observed emission.

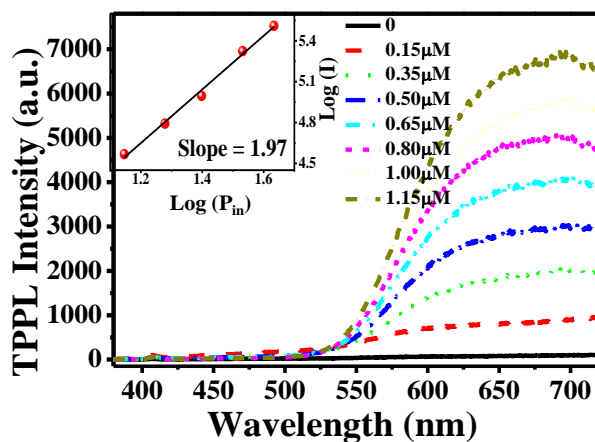


**Figure 2.3:** TPPL spectra of Au NSs in the presence of different amounts of cysteamine to induce the aggregation and plasmon coupling. TPPL spectra were measured using fs laser pulses at 800 nm as the excitation source. The inset is the power dependence of TPPL intensities of coupled Au NSs at 650 nm.

Two possible excitation mechanisms could be responsible for the observed emission: coherent two-photon absorption process or two sequential one-photon absorption processes. Considering the similarity between the extinction spectra of Au NRs and coupled Au NSs, the observed TPPL in Au NRs and coupled Au NSs is likely to arise from a similar excitation mechanism. The coherent two-photon absorption mechanism was mainly supported by the observation of  $\cos^4\theta$  excitation polarization dependence of TPPL intensities of Au NRs.<sup>30, 32</sup> However, single particle TPPL studies on Au NRs by Imura et al. gave a  $\cos^2\theta$  dependence on the excitation polarization instead,<sup>26</sup> which supported the mechanism of sequential one-photon absorption instead. The work by Biagioni et al.<sup>28, 29</sup> lent strong support for the sequential absorption mechanism by the observation that TPPL of Au nanowires were insensitive to pulse



duration for pulse widths of  $<1$  ps.

## **2.5 Excitation Mechanisms Studied by Two-Pulse Emission Modulation and Pump-Probe Techniques**

In order to further clarify the excitation nature of the observed TPPL, we utilized a two-pulse emission modulation (TPEM) technique<sup>39</sup> to investigate the correlation effects of two pulses on the observed emission in Au NRs and coupled Au NSs. The experimental setup is shown in chapter 1 and the details are described in experimental section. In this technique, the emission intensity was recorded as a function of time delay ( $\Delta t$ ) between two laser beams of similar intensities with one of the beams being chopped at 500 Hz. This technique allows one to clarify the roles and the contributions of two non-overlapping pulses with adjustable time delay to the TPPL. The detected emission arises from two contributions: (a) both excitation pulses from the chopped pulses (referred as auto-contribution), and (b) one excitation pulse from the chopped beam and another from the unchopped beam (referred as the cross-contribution). The auto-contribution is expected to contribute for all the delay times and independent of the time delay between two beams since both excitation pulses come from the same beam (the chopped beam). The cross contribution will decay quickly as the time delay increases, depending on the excitation nature of the system. If the observed emission arises from simultaneous absorption of two photons from the incident radiation field (i.e. coherent two-photon excitation, Figure 2.4, left), both auto-contribution and cross-contribution will contribute to the detected emission at short time delay when

two pulses temporally overlap, while only the auto-contribution will contribute to the detected emission when two pulses are well separated from each other. The cross contribution is expected to quickly decay to zero as the temporal overlap between two laser pulses vanishes, closely following the autocorrelation profile of the laser pulses. On the other hand, if the observed emission arises from two sequential one-photon absorption steps, the cross contribution is expected to decay with the lifetime of intermediate states. The delay time dependent cross contribution can thus be obtained by subtracting the signal levels at very large time delay (auto-contribution only) from the signal levels of different time delay between two beams (auto-contribution + cross-contribution). This technique can thus be utilized to differentiate two mechanisms shown in Figure 2.4 to clarify the excitation nature of Au NRs and coupled Au NSs.

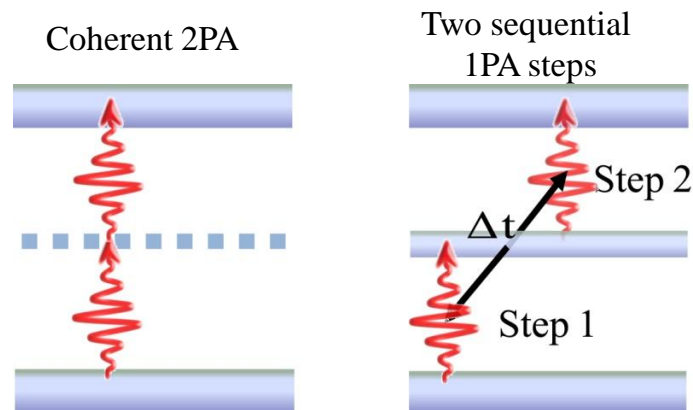


**Figure 2.4:** Schematics of coherent two-photon absorption (2PA) process through a virtual state (left) and two sequential one-photon absorption (1PA) steps mediated by real intermediate states (right).

### 2.5.1 Fluorescein: a standard two-photon absorption organic dye

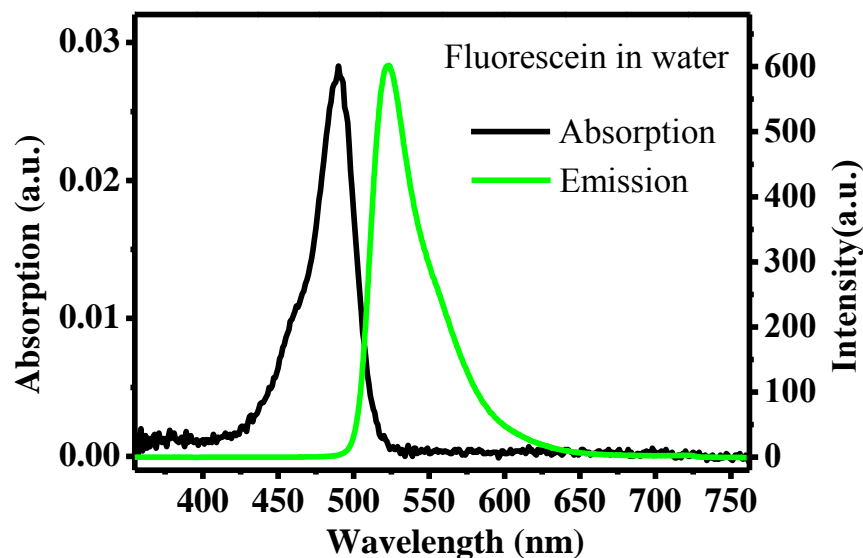


**Figure 2.5:** Absorption and fluorescence spectra of fluorescein in water (pH was adjusted to 11 by using proper amount of NaOH).

The above idea was first tested in fluorescein. Fluorescein is a fluorescent dye widely used as a standard reference for fluorescence quantum yield and two-photon absorption cross section measurements.<sup>40</sup> As shown in Figure 2.5, its absorption and emission maxima in water solution (with pH adjusted to 11) are located at 490 and 520 nm, respectively. Its emission under excitation at 800 nm femtosecond laser pulses arises from coherent two-photon absorption.

The autocorrelation profile of the laser pulses were measured by using a type-I BBO crystal as the doubling crystal, giving a FWHM of 85 fs and the corresponding pulse duration of 60 fs. As expected, the TPDM decay profile of fluorescein in water solution follows the autocorrelation profiles of the laser pulses closely (Figure 2.6), consistent with the coherent two-photon excitation nature of the observed emission under excitation of 800 nm femtosecond laser pulses. The subtle difference between

the TPEM and autocorrelation profiles is due to slight broadening of the laser pulses by the water solvent and quartz cell.

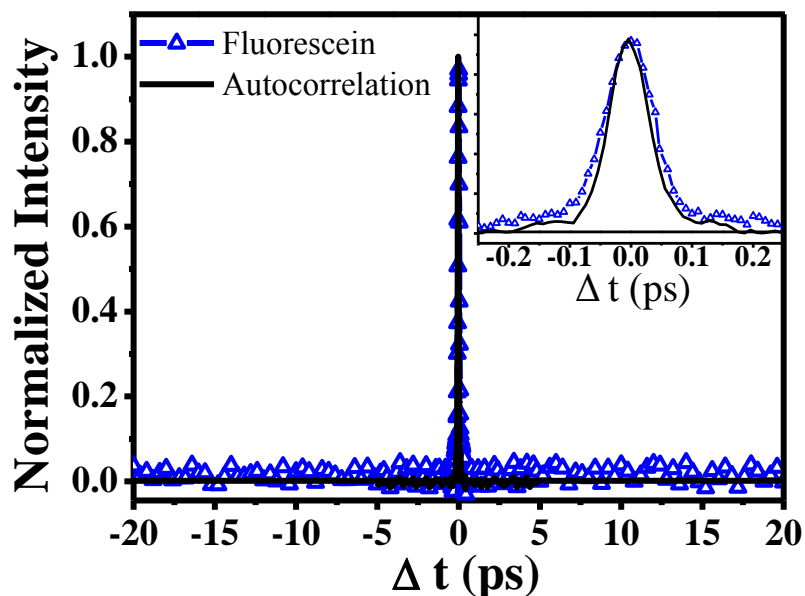


**Figure 2.6:** TPEM measurement of fluorescein. The black curve is pulse autocorrelation profile measured by using a BBO doubling crystal.

### 2.5.2 Au nanorods

To our surprise, the TPEM measurement results of Au NRs are quite different compared to fluorescein. Here Au NRs with dimension of 19 x 74 nm (aspect ratio of 3.9) and longitudinal LSPR band at 800 nm were used. The decay profiles of the TPEM cross contribution were nearly symmetrical for positive and negative time delay between the two laser beams. The emission intensity decreases slowly as the time delay between two beams increases, much slower than the auto-correlation profile of the laser pulses.

The significantly longer decay profile of the cross contribution of the TPEM for Au NRs suggests that the observed TPPL in Au NRs cannot be explained by the

coherent two-photon absorption model and provides a direct evidence that some real intermediate states are involved. Exponential fitting of the positive delay portion gives a time constant of  $4.0 \pm 0.2$  ps. These Au NRs show a strong plasmon extinction band at 800 nm, indicating the existence of intermediate states.

The lifetime of these intermediate states could be measured by pump-probe experiments. We have conducted pump-probe measurements on Au NRs with pump wavelength at 800 nm and probe wavelength at 760 nm under pump fluence of  $28.3 \mu\text{J}\cdot\text{cm}^{-2}$  (Figure 2.7b). The pump fluence used in the experiment was indicated by the vertical dashed line in the inset (Figure 2.7b), confirming that the used pump fluence fell in the linear regime of pump fluence dependent pump-probe signals.

Under this condition, excitation at 800 nm promotes Au NRs to the intermediate states by one-photon absorption to allow us to measure the lifetime of intermediate states, which was seen to be  $3.9 \pm 0.1$  ps. The consistency between the lifetime of intermediate states and the decay time of cross contribution term of the TPEM measurement support the fact that the observed emission arises from two sequential one-photon absorption processes via some real intermediate states.

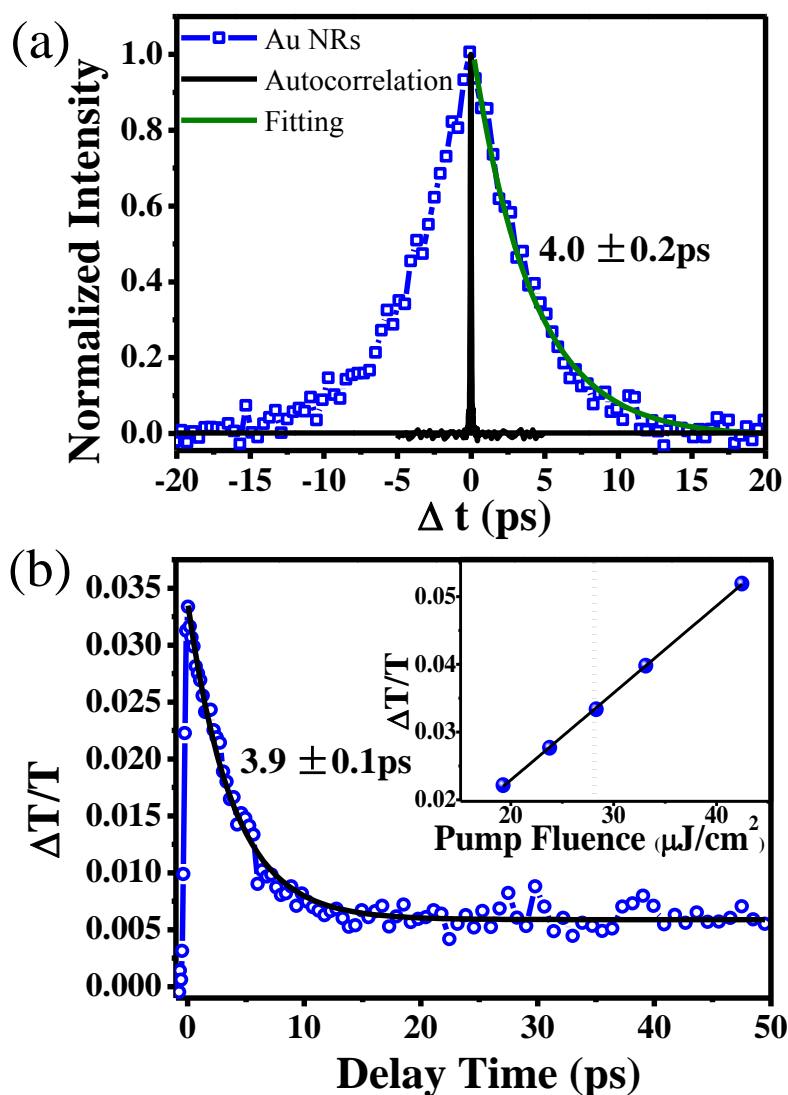


**Figure 2.7:** (a) TPEM measurement of Au NRs. (b) Pump-probe measurement result on Au NRs ( $\lambda_{\text{pump}}=800$  nm,  $\lambda_{\text{probe}}=760$  nm). The inset of (b) confirms the linear dependence of the pump-probe signal on the pump fluence to ensure the used pump power (indicated by the vertical dashed line) falling into the linear regime.

### 2.5.3 Coupled Au nanospheres

The TPEM measurements on coupled Au NSs have also been conducted and the results are shown in Figure 2.8. The coupled Au NSs were prepared by addition of 1.15  $\mu\text{M}$  of cysteamine into the Au NSs solution. The cross contribution of the TPEM signal of coupled Au NSs decays with a single exponential time constant of  $3.1 \pm 0.1$

ps, much slower compared to the autocorrelation profiles of laser pulses. Extinction spectra of the coupled Au NSs (Figure 2.3) indicate existence of intermediate states that could be excited at 800 nm by one-photon absorption process. Pump-probe measurements ( $\lambda_{\text{pump}} = 800 \text{ nm}$  and  $\lambda_{\text{probe}} = 760 \text{ nm}$ ) on the coupled Au NSs gave a lifetime of  $2.9 \pm 0.1 \text{ ps}$  for these coupling induced intermediate states. This behavior is very similar to those of Au NRs: decay time constant of the TPEM cross contribution is coincident with the lifetime of the intermediate states.

This result confirms that Au NRs and coupled Au NSs share the same excitation mechanism: two sequential one-photon excitation processes via real intermediate states. These results suggest that the previous observation of significantly enhanced TPPL in coupled metal nanoparticles compared to isolated nanoparticles<sup>21-24</sup>, can be ascribed to the formation of a longitudinal LSPR mode at the excitation wavelength induced by plasmon coupling between adjacent metal nanoparticles. The newly formed longitudinal LSPR mode provides enhanced local fields at the excitation wavelength, and thereby facilitates two sequential one-photon absorption steps at 800 nm via real intermediate states, resulting in huge enhancement in two-photon excitation efficiency and TPPL.

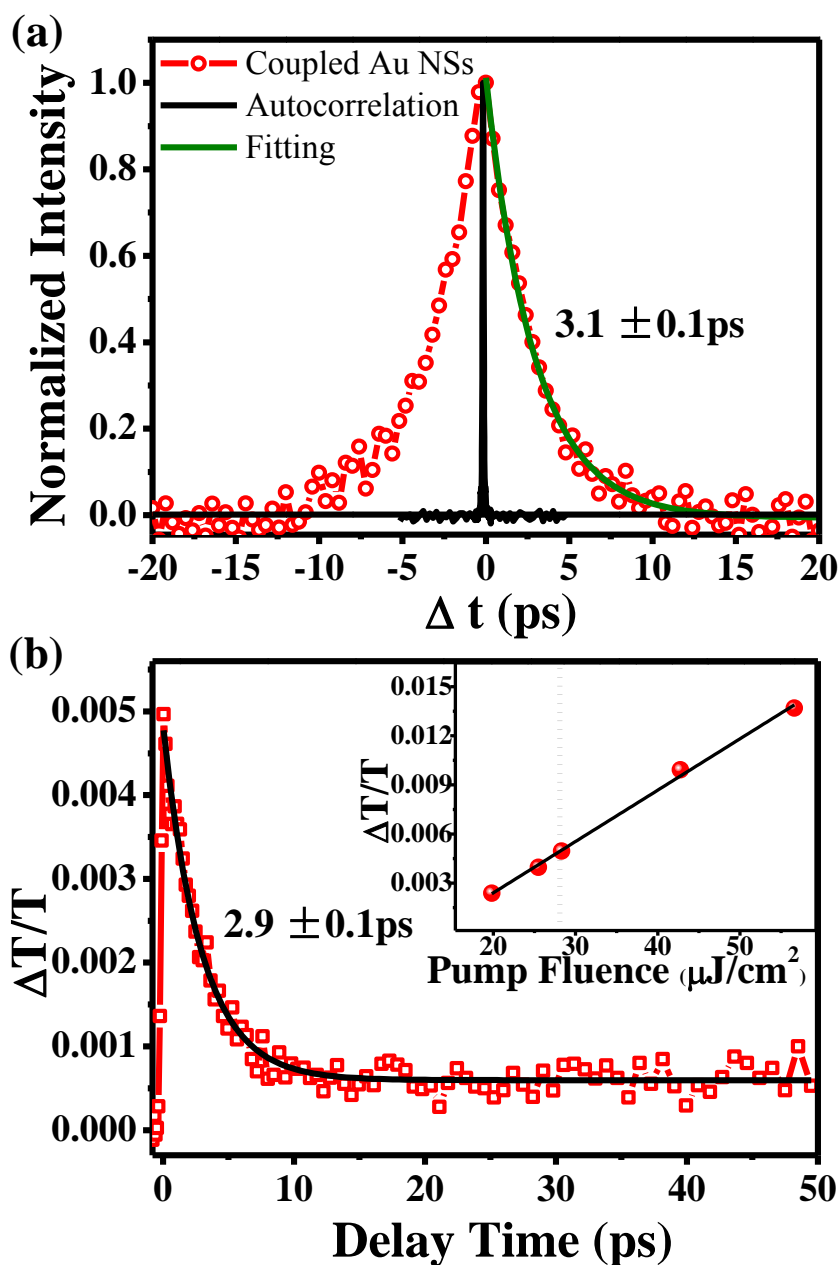


**Figure 2.8:** TPEM (a) and pump-probe (b) measurement results of the coupled Au NSs. The black curves in (a) is the pulse autocorrelation profile. The pump-probe measurement was performed with  $\lambda_{\text{pump}}=800$  nm,  $\lambda_{\text{probe}}=760$  nm and pump fluence (indicated by the vertical dashed line in the inset of (b)) falling in the linear regime of pump fluence dependent signals.

## 2.6 Conclusion

Two-pulse emission modulation measurements and pump-probe technique using 60 fs laser pulses on fluorescein, Au NRs and coupled Au NSs were performed to



understand the excitation mechanisms of TPPL in Au NRs and coupled Au NSs. The decay profile of the cross contribution of TPEM measurements on fluorescein follows the autocorrelation profile of the laser pulses, as expected for a coherent two-photon absorption process mediated by a virtual state. In contrast, the profiles of cross contribution of TPEM measurements on Au NRs and coupled Au NSs decay with much slower time constants compared to the autocorrelation profile of laser pulses. The decay time constants ( $4.0 \pm 0.2$  ps for Au NRs and  $3.1 \pm 0.1$  ps for coupled Au NSs) match well as the lifetimes of the intermediate states ( $3.9 \pm 0.1$  ps for Au NRs and  $2.9 \pm 0.1$  ps for coupled Au NSs) as measured by femtosecond pump-probe ( $\lambda_{\text{pump}}=800$  nm and  $\lambda_{\text{probe}}=760$  nm) measurements. These results support the excitation mechanism that the observed TPPL in Au NRs and coupled Au NSs arise from two sequential one-photon absorption steps involving real intermediate states. The existence of these intermediate states is evident from the extinction spectra of Au NRs and coupled Au NSs. These results give direct evidence that formation of LSPR band induced by plasmon coupling between adjacent nanoparticles in coupled Au nanostructures can significantly enhance the two-photon excitation efficiency by two sequential one-photon absorption steps. As the resonance energy and strength of this LSPR band could be tuned by the dimension of nanoparticles and interparticle coupling, their nonlinear plasmonic properties could be engineered to cater various applications. Our studies help to understand the fundamental excitation nature of nonlinear optical properties in various Au nanostructures as well as their practical applications in

two-photon sensing, imaging, phototherapy and optoelectronics.

## References

- (1) Link, S. and El-Sayed, M.A. *Annu. Rev. Phys. Chem.* **2003**, *54*, 331-366.
- (2) Hartland, G.V. *Chem. Rev.* **2011**, *111*, 3858-3887.
- (3) Lu, X., Rycenga, M., Skrabalak, S.E., Wiley, B. and Xia, Y. *Annu. Rev. Phys. Chem.* **2009**, *60*, 167-192.
- (4) Jiang, Y., Horimoto, N.N., Imura, K., Okamoto, H., Matsui, K. and Shigemoto, R. *Adv. Mater.* **2009**, *21*, 2309-2313.
- (5) Saha, K., Agasti, S.S., Kim, C., Li, X. and Rotello, V.M. *Chem. Rev.* **2012**, *112*, 2739-2779.
- (6) Jiang, C., Guan, Z., Rachel Lim, S.Y., Polavarapu, L. and Xu, Q.-H. *Nanoscale* **2011**, *3*, 3316-3320.
- (7) Lee, Y.H., Yan, Y., Polavarapu, L. and Xu, Q.H. *Appl. Phys. Lett.* **2009**, *95*, 023105.
- (8) Bachelier, G., Butet, J., Russier-Antoine, I., Jonin, C., Benichou, E. and Brevet, P.F. *Phys. Rev. B* **2010**, *82*, 235403.
- (9) Polavarapu, L., Venkatram, N., Ji, W. and Xu, Q.H. *ACS Appl. Mater. Interfaces* **2009**, *1*, 2298-2303.
- (10) Kelly, K.L., Coronado, E., Zhao, L.L. and Schatz, G.C. *J. Phys. Chem. B* **2002**, *107*, 668-677.
- (11) Noguez, C. *J. Phys. Chem. C* **2007**, *111*, 3806-3819.
- (12) Zhao, J., Pinchuk, A.O., McMahon, J.M., Li, S., Ausman, L.K., Atkinson, A.L. and Schatz, G.C. *Acc. Chem. Res.* **2008**, *41*, 1710-1720.
- (13) Zhang, S., Kou, X., Yang, Z., Shi, Q., Stucky, G.D., Sun, L., Wang, J. and Yan, C. *Chem. Commun.* **2007**, *0*, 1816-1818.
- (14) Sun, Z., Ni, W., Yang, Z., Kou, X., Li, L. and Wang, J. *Small* **2008**, *4*, 1287-1292.
- (15) Nie, S. and Emory, S.R. *Science* **1997**, *275*, 1102-1106.
- (16) Mohamed, M.B., Volkov, V., Link, S. and El-Sayed, M.A. *Chem. Phys. Lett.* **2000**, *317*, 517-523.
- (17) Cheng, D. and Xu, Q.-H. *Chem. Commun.* **2007**, 248-250.
- (18) Yuan, P., Lee, Y.H., Gnanasammandhan, M.K., Guan, Z., Zhang, Y. and Xu, Q.-H. *Nanoscale* **2012**, *4*, 5132-5137.

- (19) Ming, T., Zhao, L., Yang, Z., Chen, H., Sun, L., Wang, J. and Yan, C. *Nano Lett.* **2009**, *9*, 3896-3903.
- (20) Acuna, G.P., Möller, F.M., Holzmeister, P., Beater, S., Lalkens, B. and Tinnefeld, P. *Science* **2012**, *338*, 506-510.
- (21) Zhao, T., Shen, X., Li, L., Guan, Z., Gao, N., Yuan, P., Yao, S.Q., Xu, Q.-H. and Xu, G.Q. *Nanoscale* **2012**, *4*, 7712-7719.
- (22) Guan, Z., Polavarapu, L. and Xu, Q.-H. *Langmuir* **2010**, *26*, 18020-18023.
- (23) Han, F., Guan, Z., Tan, T.S. and Xu, Q.-H. *ACS Appl. Mater. Interfaces* **2012**, *4*, 4746-4751.
- (24) Guan, Z., Gao, N., Jiang, X.-F., Yuan, P., Han, F. and Xu, Q.-H. *J. Am. Chem. Soc.* **2013**.
- (25) Dulkeith, E., Niedereichholz, T., Klar, T.A., Feldmann, J., von Plessen, G., Gittins, D.I., Mayya, K.S. and Caruso, F. *Phys. Rev. B* **2004**, *70*, 205424.
- (26) Imura, K., Nagahara, T. and Okamoto, H. *J. Phys. Chem. B* **2005**, *109*, 13214-13220.
- (27) Ueno, K., Juodkasis, S., Mizeikis, V., Sasaki, K. and Misawa, H. *Adv. Mater.* **2008**, *20*, 26-30.
- (28) Biagioni, P., Celebrano, M., Savoini, M., Grancini, G., Brida, D., M á ě ĩ-Tempfli, S., M á ě ĩ-Tempfli, M., Du ò L., Hecht, B., Cerullo, G. and Finazzi, M. *Phys. Rev. B* **2009**, *80*, 045411.
- (29) Biagioni, P., Brida, D., Huang, J.-S., Kern, J., Du ò L., Hecht, B., Finazzi, M. and Cerullo, G. *Nano Lett.* **2012**, *12*, 2941-2947.
- (30) Wang, H., Huff, T.B., Zweifel, D.A., He, W., Low, P.S., Wei, A. and Cheng, J.-X. *Proc. Natl. Acad. Sci. U. S.A.* **2005**, *102*, 15752-15756.
- (31) Kim, H., Xiang, C., Güell, A.G., Penner, R.M. and Potma, E.O. *J. Phys. Chem. C* **2008**, *112*, 12721-12727.
- (32) Durr, N.J., Larson, T., Smith, D.K., Korgel, B.A., Sokolov, K. and Ben-Yakar, A. *Nano Lett.* **2007**, *7*, 941-945.
- (33) Grubisic, A., Schweikhard, V., Baker, T.A. and Nesbitt, D.J. *ACS Nano* **2012**, *7*, 87-99.
- (34) Huang, J., Wang, W., Murphy, C.J. and Cahill, D.G. *Proc. Natl. Acad. Sci. U.S.A.* **2014**, *111*, 906-911.
- (35) Frens, G. *Nature* **1973**, *241*, 20-22.
- (36) Jana, N.R., Gearheart, L. and Murphy, C.J. *J. Phys. Chem. B* **2001**, *105*, 4065-4067.
- (37) Nikoobakht, B. and El-Sayed, M.A. *Chem. Mater.* **2003**, *15*, 1957-1962.

- (38) Abbas, A., Tian, L., Kattumenu, R., Halim, A. and Singamaneni, S. *Chem. Commun.* **2012**, 48, 1677-1679.
- (39) Xu, Q.-H., Gaylord, B.S., Wang, S., Bazan, G.C., Moses, D. and Heeger, A.J. *Proc. Natl. Acad. Sci. U.S.A.* **2004**, 101, 11634-11639.
- (40) Xu, C. and Webb, W.W. *J. Opt. Soc. Am. B* **1996**, 13, 481-491.

# Chapter 3. Solvent Dependent Two-Photon Photoluminescence and Excitation Dynamics of Gold Nanorods

## 3.1 Introduction

Noble metal nanoparticles have been known to display unique optical properties such as localized surface plasmon resonance (LSPR).<sup>1-3</sup> The frequency of LSPR can be tuned by controlling the particle size, shape, and refractive index of the surrounding medium.<sup>4, 5</sup> Due to plasmon resonance, metal nanoparticles display significantly enhanced optical responses such as extremely large extinction coefficients, enhanced second harmonic generation (SHG) and two-photon photoluminescence (TPPL).<sup>6-11</sup> Metal nanoparticles could also be utilized to enhance the optical responses of nearby chromophores, including surface enhanced Raman scattering (SERS)<sup>12, 13</sup> and metal enhanced fluorescence.<sup>14-16</sup>

Among various metal nanoparticles, Au NRs have been known to display strong TPPL owing to the lightning rod effect.<sup>17</sup> Au NRs have high two-photon absorption action cross section ( $10^4$  GM), about 2 orders of magnitude larger than small organic molecules (1-100 GM).<sup>18</sup> The TPPL intensity of a single Au NR is ~58 times stronger than that of a single rhodamine molecule.<sup>19</sup> Au NRs have also been recently demonstrated to effectively generate singlet oxygen generation under two-photon excitation.<sup>20, 21</sup> The longitudinal LSPR band of Au NRs is tunable from 580 to 1000 nm

by adjusting the aspect ratio.<sup>3,22</sup> The excellent optical properties, good biocompatibility and chemical inertness of Au NRs render them to be extensively exploited for applications in bio-sensing,<sup>23,24</sup> two-photon imaging,<sup>19,25</sup> gene and drug delivery,<sup>26,27</sup> photo-thermal and photodynamic therapy.<sup>20,28</sup>

Most of the previous studies on Au NRs are focused on aqueous solution as Au NRs are typically prepared by using cetyltrimethylammonium bromide (CTAB) as the capping and stabilizing agents and can be well dispersed in water.<sup>29,30</sup> The optical properties of Au NRs in the organic solvents have been rarely studied due to the difficulty in dispersing CTAB capped Au NRs into organic solvents.<sup>31</sup> Dispersion of Au NRs into organic solvents could be improved by modifying the surfaces of Au NRs with alkanethiol molecules such as PEG-SH.<sup>32</sup> The PEG layer acts as a steric barrier to prevent the aggregation of Au NRs. PEG capped Au NRs can thus disperse well in various organic solvent such as DMF and methanol,<sup>33</sup> providing the opportunity to investigate the solvent dependent optical properties of Au NRs.

In this work, we have prepared PEG-SH modified Au NRs that can be well dispersed in various organic solvents to study the solvent effects on the TPPL properties and ultrafast dynamics of Au NRs. The TPPL properties of Au NRs were investigated in different organic solvents (such as DMF, DEG, CH<sub>3</sub>OH, C<sub>2</sub>H<sub>5</sub>OH, CH<sub>3</sub>CN, DMSO, and THF) and mixture solvents. The TPPL intensity of Au NRs was found to be strongly dependent on the solvents. The TPPL intensities of Au NRs in these organic solvents are much weaker compared to that in H<sub>2</sub>O. Ultrafast

time-resolved transient absorption and pump-probe measurements have been performed on Au NRs in H<sub>2</sub>O, DMF and DEG to understand the observed TPPL quenching mechanisms of Au NRs in these organic solvents. Different from the decay behaviors of Au NRs in H<sub>2</sub>O, an additional transient species was observed in Au NRs in DMF or DEG upon photo-excitation. This additional transient species was found to appear at the intermediate delay time (tens of picoseconds) and subsequently disappear on the nanosecond time scales. This intermediate state is ascribed to the charge separated species. The observation of this transient species serves as a direct evidence to support that the observed TPPL quenching in organic solvents is due to electron transfer from electron-donating solvents to the excited Au NRs. The TPPL properties of Au NRs in the presence of different buffer solutions and various different ions have also been studied to support the proposed electron transfer quenching mechanism. These studies provide useful information on fundamental understanding the TPPL of Au NRs and their quenching mechanisms, which will provide guidelines for choosing proper conjugated surfactants to improve the TPPL efficiency of Au NRs for their biological applications.

## **3.2 Experimental Section**

### **Preparation of PEG-SH capped gold nanorods:**

Gold nanorods (Au NRs) with longitudinal LSPR band centered at 780 nm were prepared according to a previously reported seed-mediated growth method.<sup>34, 35</sup> CTAB

aqueous solution (0.1 M, 10 mL) was mixed with  $\text{HAuCl}_4$  (50 mM, 50  $\mu\text{L}$ ) and ice-cold  $\text{NaBH}_4$  (10 mM, 0.6 mL) to form a brownish-yellow seed solution. This seed solution was kept at room temperature for at least 2 hrs. In the growth solution, CTAB solution (0.1 M 10 mL) was mixed with  $\text{HAuCl}_4$  (50 mM, 0.1 mL), different amounts of  $\text{AgNO}_3$  (10 mM, 63  $\mu\text{L}$ ),  $\text{HCl}$  (1.0 M 0.2 mL) and AA (0.1 M, 80  $\mu\text{L}$ ). After gentle mixing of the solution, the color of the growth solution changed to colorless. After the gold seed solution (25  $\mu\text{L}$ ) was added into the growth solution, the reaction mixture was then left undisturbed overnight. The obtained Au NRs were purified once by washing with de-ionized water to remove excess CTAB and re-dispersed in 10 mL deionized water. All procedures were conducted at room temperature unless otherwise specified.

The PEG-SH capped Au NRs were prepared by using a method previously reported by Thierry et al.<sup>36</sup> The aqueous Au NR solution (5 ml) were mixed with 2 ml of 2 mM PEG-SH solution and the reaction mixtures were left overnight under vigorous stirring. In this process, the original CTAB surfactant molecules on the surface of Au NRs were replaced by PEG molecules through formation of strong binding between Au and the thiol group of PEG-SH.

#### **Characterizations and two-photon photoluminescence measurements:**

Transmission electron microscopy (TEM) images of nanoparticles were taken from a Philips CM10 TEM microscope (at an accelerating voltage of 100 kV). Ultraviolet-visible (UV-Vis) extinction spectra were measured by using a SHIMADZU



UV-2550 spectrophotometer. TPPL of Au NRs were measured by using an Avesta TiF-100M femtosecond (fs) Ti:sapphire oscillator as the excitation source. The output laser pulses have a central wavelength tunable from 750 to 840 nm with pulse duration of 80 fs and a repetition rate of 84.5 MHz. The laser beam was focused onto the samples using a lens with a focus length of 3.0 cm. The emission was collected at the direction perpendicular to the excitation beam to minimize the scattering. The emission signal was directed into a CCD (Princeton Instruments, Pixis 100B) coupled monochromator (Acton, Spectra Pro 2300i) with an optical fiber. A 750 nm short pass filter was placed before the spectrometer to minimize the scattering from the excitation light.

#### **Transient absorption and pump-probe measurements:**

Time-resolved transient absorption and pump-probe measurements were performed on Au NRs suspensions by using a Ti:sapphire oscillator seeded regenerative amplifier (Spectra Physics Spitfire pro), which gives an output with a pulse energy of 2.0 mJ at 800 nm and a repetition rate of 1 kHz. The 800 nm laser beam was split into two portions. The larger portion of the beam passed through a BBO crystal to generate the 400 nm pump beam by second harmonic generation. A small portion of the 800 nm beam was focused onto a 1 mm sapphire plate to generate white light continuum. The white light beam was split into two beams, one as the probe and the other as the reference to correct the pulse-to-pulse intensity fluctuations. The intensities of signal and reference beams were measured by photodiodes that are

connected to lock-in amplifiers and the computer. The pump beam was focused onto the sample with a beam size of 300  $\mu\text{m}$  and overlaps with the smaller-diameter (100  $\mu\text{m}$ ) probe beam. The delay between the pump and probe pulses was varied by a computer-controlled translation stage (Newport, ESP 300). The pump beam was modulated by an optical chopper at a frequency of 500 Hz. The variation transmittance at selected probe wavelength is recorded as a function of time delay between pump and probe pulses. All the experiments were performed at room temperature. Au NRs in different solvents were contained in a 1 mm path length cuvette. During the measurements, the extinction spectra of the sample were checked before and after the experiments and only subtle difference was observed, which suggests that the sample is stable and there is little photo-damage to the sample during the whole experiments.

### **3.3 Two-Photon Photoluminescence Variation of Au Nanorods in Different Solvents**

Au NRs were prepared by using a seed-mediated, CTAB-assisted method.<sup>34, 35</sup> This method for preparation of Au NRs involves the use of bilayer CTAB as a template. The CTAB capping layer could be easily destroyed by organic solvents, which consequently causes aggregation and precipitation of Au NRs in organic solvents. Thiol groups are considered to have the highest affinity to noble metal surfaces, in particular to gold ( $\sim 200 \text{ kJ mol}^{-1}$ ).<sup>37</sup> Replacing CTAB with PEG molecules allows Au NRs to be well dispersed in various organic solvents such as DMF and methanol.

Their TEM images (Figure 3.1a) clearly show that the prepared PEG capped Au NRs are highly mono-disperse with an average aspect ratio  $\sim 3.8$ . Figure 3.1b shows the extinction spectra of PEG-SH capped Au NRs in H<sub>2</sub>O/DMF mixed solvents with different volume ratios. The longitudinal LSPR band of these Au NRs is centered at 780 nm in H<sub>2</sub>O, which gradually red-shifts from 780 to 809 nm with increasing the volume ratio of DMF. The observed red-shift is due to the increasing refractive index of the mixed solvents, which is consistent with the previous report that longitudinal LSPR band is highly sensitive to the refractive index of the surrounding media.<sup>38, 39</sup> This phenomenon has been widely utilized to develop plasmonic nano-sensors for detection of various chemical and biological targets.<sup>40, 41</sup>

We have further investigated the solvent effect on TPPL properties of PEG capped Au NRs by measuring their TPPL spectra in H<sub>2</sub>O/DMF mixed solvents with different volume ratios (Figures 3.1c & d). TPPL spectra were measured by using femtosecond laser pulses at 820 nm with average power of 100 mW as the excitation source. The TPPL spectra of Au NRs in different solvents were broad without any fine-structure in the visible range, which is consistent with the previous report.<sup>20, 42</sup> The steep edge of TPPL spectra at long wavelength is due to the emission enhancement by the longitudinal LSPR of Au NRs and the cut-off effect by the emission filter, which has extremely low transmittance at the wavelength longer than 750 nm. It is interesting to find that the TPPL intensity of Au NRs gradually decreases with the increasing content of DMF in H<sub>2</sub>O/DMF mixed solvents. The TPPL intensity of Au NRs in DMF was

quenched by nearly 91-fold compared to that in H<sub>2</sub>O.

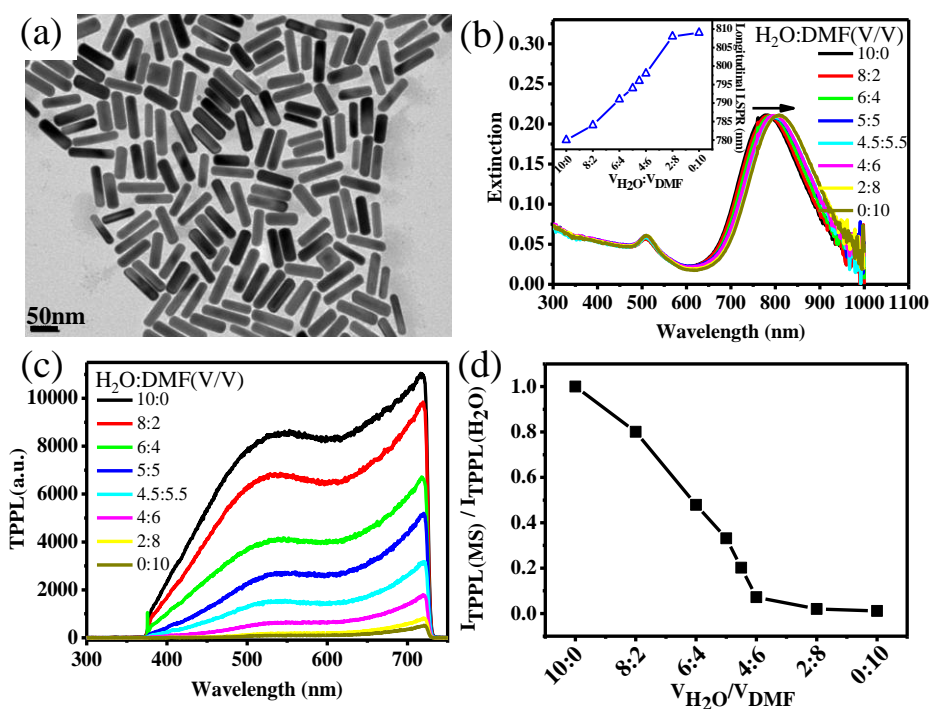


**Figure 3.1:** (a) TEM image of PEG-SH capped Au NRs. (b) Extinction spectra, (c) TPPL spectra, and (d) relative TPPL intensities of Au NRs in H<sub>2</sub>O/DMF mixed solvents with different volume ratios.

Similar TPPL quenching behaviors were also observed in the H<sub>2</sub>O/DEG mixed solvents with different volume ratios (Figure 3.2). The TPPL intensity of PEG capped Au NRs in DEG is quenched by ~47 times compared to that in H<sub>2</sub>O. The TPPL spectra of Au NRs in other organic solvents, including CH<sub>3</sub>OH, CH<sub>3</sub>CN, DMSO, and THF have also been measured (Figure 3.3). The TPPL intensities of Au NRs in these solvents were all found to be significantly quenched compared to that in H<sub>2</sub>O.

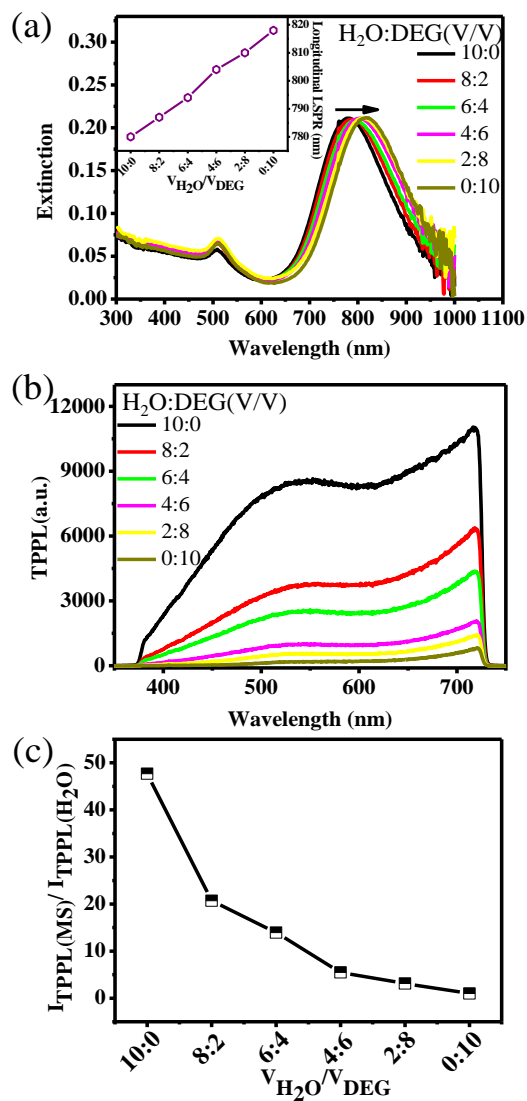


**Figure 3.2:** (a) Extinction spectra, (b) TPPL spectra, and (c) relative TPPL intensities of Au NRs in H<sub>2</sub>O/DEG mixed solvent with different volume ratios.

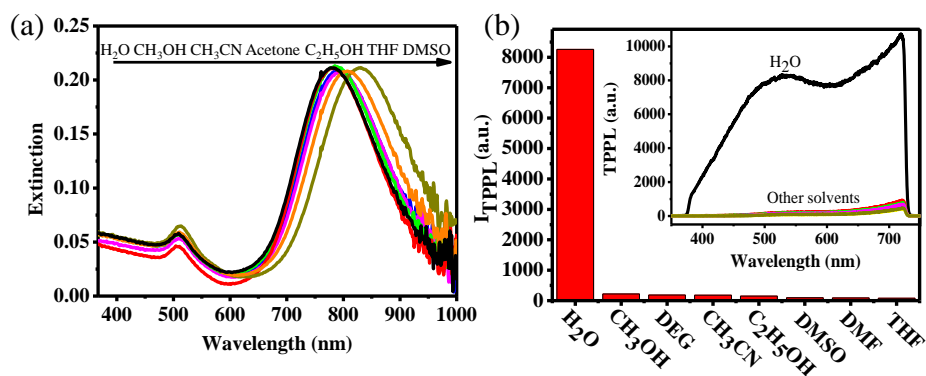


**Figure 3.3:** (a) Extinction and (b) TPPL spectra of Au NRs in various solvents.

### 3.4 Mechanisms and Dynamics of Two-Photon Photoluminescence Quenching in Organic Solvents

Generally there are three different possible mechanisms responsible for photoluminescence quenching: aggregation induced quenching, energy transfer, and electron transfer. Formation of aggregate of noble metal nanoparticles generally results in characteristics of a decrease in the original LSPR band and appearance of new band, which can be monitored by measuring their extinction spectra.<sup>21</sup> Extinction spectra of Au NRs in different solvents (Figures 3.1b and 3.2a and 3.3a) do not indicate any signature of aggregate formation. Furthermore, as described in Chapter 1, aggregation of metal nanoparticles generally results in enhanced TPPL instead of quenched TPPL.<sup>7</sup>

<sup>43</sup> Aggregation induced quenching thus plays a negligible role in the observed TPPL quenching. Energy transfer generally requires spectral overlap between the emission spectrum of the donor and absorption spectrum of the acceptor.<sup>44</sup> In the current studies, these solvents are saturated small molecules with absorption in the UV region, which has no spectral overlap with the photoluminescence spectra of Au NRs. Energy transfer mechanism is not likely to contribute to the observed TPPL quenching. The most likely mechanism for the observed quenching is electron transfer between two-photon excited Au NRs and the surrounding solvent molecules. The electron transfer quenching mechanism has been previously reported to be responsible for fluorescence quenching of the organic fluorescent dye molecules such as rhodamine 6G in the electron-donating solvents such as dimethylaniline (DMA), DMF and methanol.<sup>45-49</sup> A

similar electron transfer mechanism from electron-donating solvents to two-photon excited Au NRs is likely to be responsible for the observed TPPL quenching in various organic solvents.

### **3.4.1 Excitation dynamics of Au nanorods in H<sub>2</sub>O, DMF and DEG solvents**

To understand and demonstrate the mechanism of the observed TPPL quenching of Au NRs in various organic solvents, their excitation dynamics were investigated by using ultrafast transient absorption and pump-probe measurements. Transient absorption spectra and single wavelength dynamics of Au NRs in different solvents and solvent mixtures were measured under excitation at 400 nm with fluence of 15.6  $\mu\text{J}\cdot\text{cm}^{-2}$ .

Figures 3.4 a-c shows the transient absorption spectra of Au NRs in H<sub>2</sub>O, DMF and DEG solvents at different delay times. The transient absorption evolution and excitation dynamics of Au NRs in H<sub>2</sub>O display a typical behavior of hot electron relaxation.<sup>29, 50-52</sup> Upon femtosecond laser excitation at 400 nm, its transient spectra show a dominant bleaching band located at the longitudinal LSPR band of Au NRs and a weak one at the transverse mode, accompanied with transient absorption in the wings of the two bands. As delay time increases, both the transient bleaching and transient absorption bands decrease in magnitude while the overall spectral profiles remain nearly unchanged. These observations are consistent with the previous reports on hot electron dynamics in Au NRs.<sup>29, 50</sup> Upon femtosecond laser excitation, the electrons are

promoted to the conduction band, leading to a jump in the electron temperatures. The temperature increase will cause a broadening of the LSPR bands, which results in the transient bleaching at the center of original LSPR bands and transient absorption at the wings of the bands. The system subsequently relaxes through a series of heat exchange processes such as electron-electron scattering (on time scale of  $\sim 100$ fs), electron-phonon scattering (on time scale of a few ps) and phonon-phonon scattering (tens to hundreds of ps).<sup>1,2</sup> The time scales of these relaxation processes of Au NRs in H<sub>2</sub>O can be obtained by monitoring their single wavelength dynamics (Figure 3.4d). The single wavelength dynamics at probe wavelength of 725 nm displays a fast exponential decay with time constant of 4.4 ps, an under-damped oscillation with period of 83 ps (frequency of 12 GHz), and a slow exponential decay with time constant of 98 ps. The fast (4.4 ps) and slow (98 ps) exponential decay components can be ascribed to electron-phonon scattering and phonon-phonon scattering processes, respectively, while the under-damped oscillation can be ascribed to the extensional mode of the longitudinal LSPR mode. The obtained time constants and oscillation period/frequency are consistent with those previously reported.<sup>1, 2, 29, 50</sup> The electron-electron scattering generally occurs on a time scale of  $\sim 100$  fs, which was not well-resolved in our measurements.



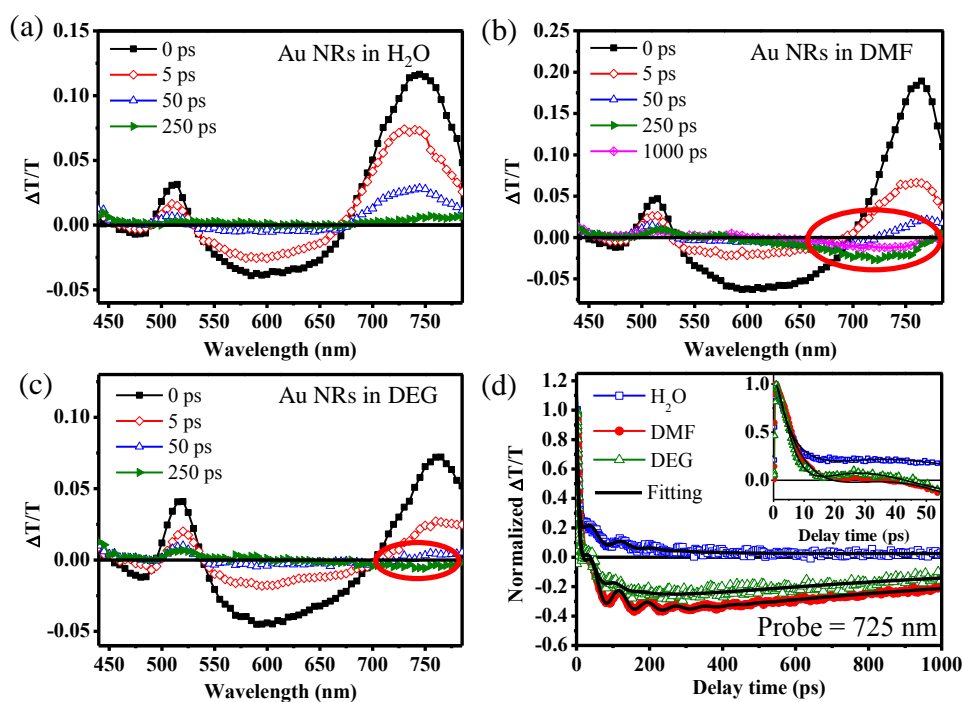


**Figure 3.4:** Transient absorption spectra of Au NRs in (a) H<sub>2</sub>O, (b) DMF, and (c) DEG at the different delay times under excitation at 400 nm; (d) Single wavelength dynamics of Au NRs in H<sub>2</sub>O, DMF and DEG probed at 725 nm.

The transient spectra and single wavelength dynamics of Au NRs in the DMF solvent displayed a quite different time-dependent evolution behavior from that in the H<sub>2</sub>O solvents. The transient spectra of Au NRs in DMF at short delay times (0 and 5 ps) are similar to those in H<sub>2</sub>O: transient bleaching of longitudinal and transverse LSPR bands and transient absorption at their wings, which decrease in magnitude as the delay time increases. However, the transient spectral profiles at longer delay times, such as 250 ps, are very different from those at short delay times. The initial transient bleaching signals (positive  $\Delta T/T$ ) changed its sign and evolved into a transient absorption signal (negative  $\Delta T/T$ ) centered at ~725 nm (highlighted by the red circles) at longer time delays, which eventually decays on an even longer time scale. This photo-induced transient absorption band in the DMF solvent suggested that a new population species

formed from the interaction between the excited Au NRs and the DMF solvent, most likely a charge transfer complex. As the photo-excitation of electron onto the sp band will create a hole in the d band, the holes could be filled by accepting an electron from the DMF molecule that possesses a lone pair of electrons. The time trace of the charge separation and recombination processes between Au NRs and the DMF molecules can be clearly visualized by the single wavelength dynamics at 725 nm (Figure 3.4d). The initial positive  $\Delta T/T$  signal (transient bleaching) decays quickly and changes sign to become negative values (transient absorption), which subsequently recover back on an even longer time scale. The formation of transient absorption signal (negative  $\Delta T/T$ ) can be ascribed to the charge separation process, while its subsequent recovery is due to charge-recombination processes.

**Table 3-1:** The fitting results of the pump-probe measurement for Au NRs in H<sub>2</sub>O, DMF and DEG at probe wavelength of 725 nm under excitation at 400 nm.

	A <sub>1</sub>	$\tau_{1,ps}$	A <sub>2</sub>	$\tau_{2,ps}$	A <sub>k</sub>	$\tau_{k,ps}$	$\nu_k$ , GHz/ps	A <sub>3</sub>	$\tau_{3,ps}$	A <sub>4</sub>	$\tau_{4,ps}$
H <sub>2</sub> O	0.77	4.4	0.19	98	0.04	145	12/83	-	-	-	-
DMF	0.71	4.5	0.18	94	0.11	140	13/77	0.45	29	-0.45	1340
DEG	0.72	4.8	0.15	95	0.13	68	15/67	0.35	46	-0.35	1250

So, the overall decay is composed of contribution of electron relaxation processes (electron-phonon scattering, phonon-phonon scattering and under-damped oscillation of the extensional mode), charge separation and recombination processes. The decay profiles were fitted with a sum of exponential decay components and an under-damped oscillation to account for the above contributions. The fitting parameters are summarized in Table 3-1.

The fitting function is a sum of four exponential decays and one under-damped

oscillation.  $A_i$  and  $\tau_i$  are the normalized amplitude and the corresponding decay time constant ( $i = 1, 2$  correspond to the relaxation processes of electron-phonon and phonon-phonon scattering,  $i = 3, 4$  correspond to the charge separation and recombination processes between Au NRs and the solvent molecules, while  $i = k$  relates to the under-damped oscillation with damping time of  $\tau_k$  and oscillation frequency of  $\nu_k$ . The amplitudes of charge separation and recombination are opposite as they correspond to appearance and disappearance of transient charge-separated species. Based on the fitting results, time constants for the charge separation and recombination processes were obtained to be  $\sim 29$  ps and 1.34 ns, respectively.

The ultrafast transient absorption and pump-probe measurements have also been performed for Au NRs in the DEG solvent (Figures 3.4c and d). The time-dependent evolution behavior of Au NRs in DEG is quite similar to that in DMF. An additional transient absorption band centered at  $\sim 725$  nm (highlighted by the red circles) appears at intermediate time delays and eventually recovers on an even longer time scale. Fitting the single wavelength dynamics at 725 nm (Figure 3.4d) gives the charge separation time constant of  $\sim 46$  ps and a charge recombination time constant of  $\sim 1.25$  ns. The slower charge separation time of Au NRs in DEG compared to that in DMF can be ascribed to stronger electron donating capability of DMF compared to DEG, consistent with the observation of less TPPL quenching of Au NRs in DEG.

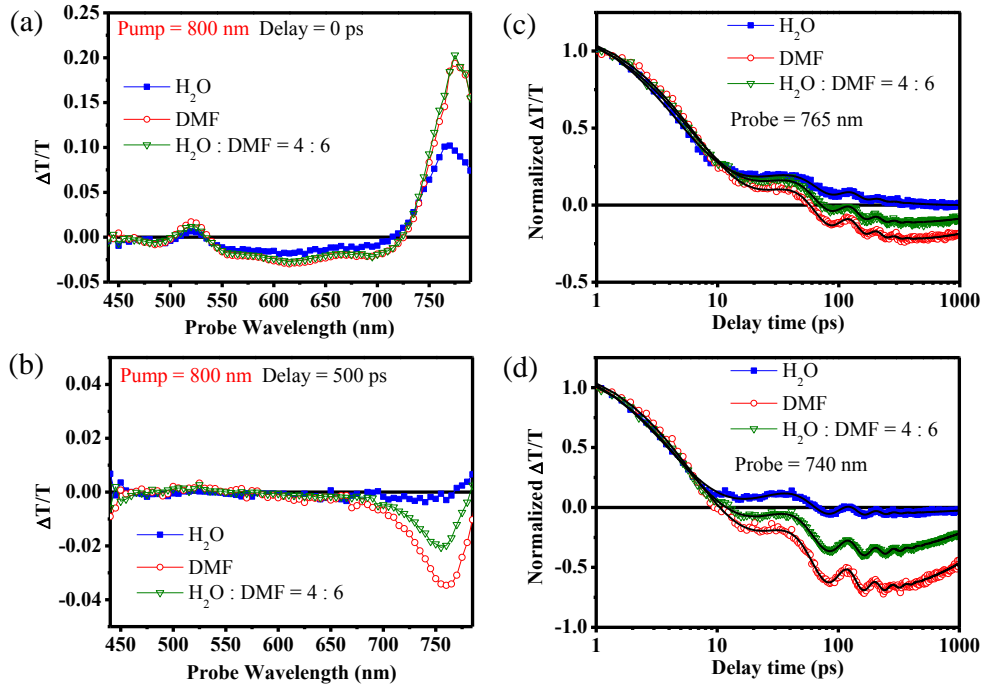


**Figure 3.5:** Transient absorption spectra of Au NRs in H<sub>2</sub>O, H<sub>2</sub>O/DMF mixture and DMF at the delay time of (a) 0 ps and (b) 500 ps; Single wavelength dynamics of Au NRs in H<sub>2</sub>O, H<sub>2</sub>O/DMF mixture and DMF probed at (c) 765 nm and (d) 740 nm under excitation at 800 nm with fluence of 25.4  $\mu\text{J}\cdot\text{cm}^{-2}$ .

We have also performed ultrafast transient absorption and pump-probe measurements on Au NRs in H<sub>2</sub>O, DMF and DEG solvents under excitation at 800 nm with excitation fluence of 25.4  $\mu\text{J}\cdot\text{cm}^{-2}$  and the data are shown in Figures 3.5 and 3.6, respectively. The decay behaviors are similar to those under excitation at 400 nm. For Au NRs in the DMF and DEG solvents, an additional transient absorption was observed, which appeared at intermediate times and recovered at even longer time scales. No such transient absorption component was observed for Au NRs in H<sub>2</sub>O. These results further confirm the charge transfer process from the electron-donating solvents to the excited Au NRs.

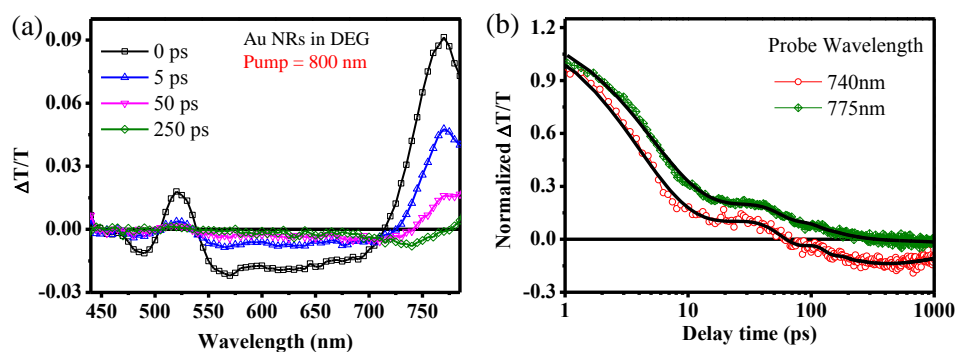


**Figure 3.6:** (a) Transient absorption spectra of Au NRs in DEG at the different delay times. (b) Single wavelength dynamics of Au NRs in DEG probed at 740 nm and 775 nm under excitation at 800 nm with fluence of  $25.4 \mu\text{J}\cdot\text{cm}^{-2}$ .

### 3.4.2 Charge transfer between Au nanorods and organic solvents

These ultrafast spectroscopic studies suggest that previous observation of significantly quenched TPPL of Au NRs in organic solvents compared to  $\text{H}_2\text{O}$  can be ascribed to the electron transfer between the excited Au NRs and the surrounding organic solvent molecules, which are shown in Figure 3.7.

After two-photon excitation of Au NRs, charge transfer from the solvent molecules to excited Au NRs will prevent the radiative recombination of the electron-hole pairs. The formed charge separated state subsequently decay back to original ground state through nonradiative charge-recombination processes, without emission of a photon, resulting in TPPL quenching of Au NRs. It is also interesting to note the oscillation associated with the extensional mode of the longitudinal LSPR mode was not interrupted by the charge separation process and still persisted in the charge-separated state.

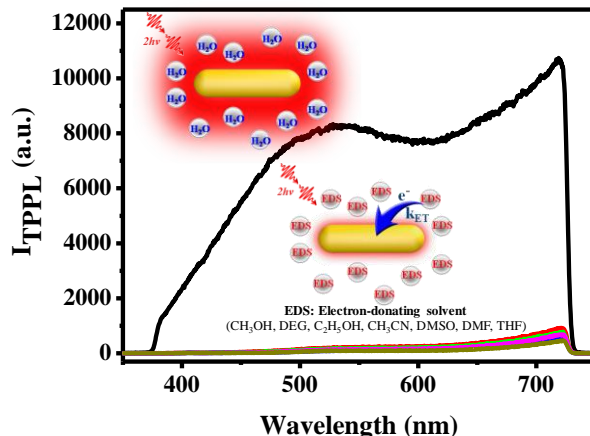


**Figure 3.7:** Schematic mechanisms of TPPL quenching behavior in organic solvents compared to that in H<sub>2</sub>O.

### 3.5 Ion Effects on Two-Photon Photoluminescence and Excitation Dynamics of Au Nanorods in H<sub>2</sub>O

The effect of different buffer solution and various ions (cations and anions) on TPPL properties of Au NRs in H<sub>2</sub>O has also been examined. The TPPL intensities of Au NRs in three most common buffer solutions only display subtle differences (Figure 3.8), which ensures high efficiency for their various biological applications.

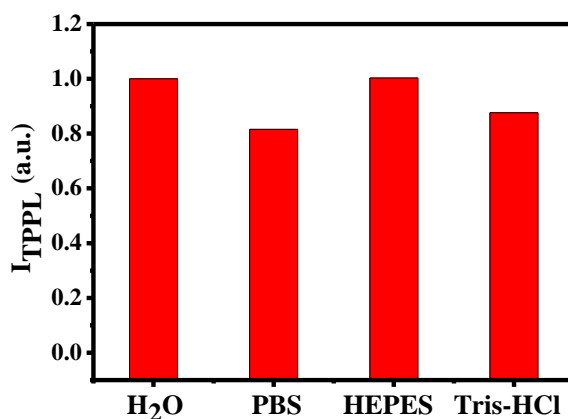


**Figure 3.8:** TPPL intensities of Au NRs in different buffer solutions. The concentrations of buffer solutions are 10 mM.

The TPPL intensities of Au NRs in H<sub>2</sub>O were nearly unaffected in the presence of

most cations and anions with concentration of  $1 \times 10^{-4}$  M (Figure 3.9). However, the TPPL intensity of Au NRs in  $H_2O$  was found to be quenched by nearly 5.0-fold in the presence of sulfide ions ( $S^{2-}$ ).  $S^{2-}$  is known to be electron-rich and can act as a good electron donor. Most importantly, it can bind with the surface of Au NRs with high affinity.

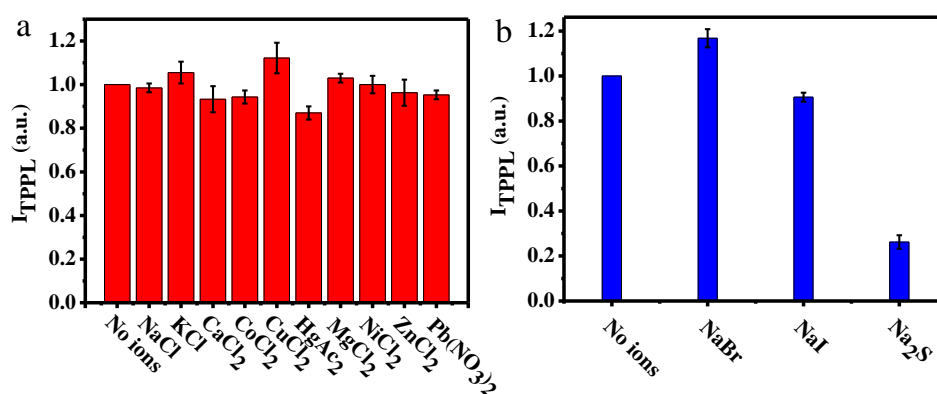


**Figure 3.9:** TPPL intensities of Au NRs in  $H_2O$  in the presence of different ions. The concentrations of ions are  $1 \times 10^{-4}$  M.

We have also conducted transient absorption and pump-probe measurements on Au NRs in the presence of different concentrations  $S^{2-}$ . As shown in Figure 3.10, the results display similar behavior to those in DMF and DEG: the decay dynamics (400 nm pump / 725 nm probe) become faster in the presence of  $S^{2-}$  compared to that in the absence of  $S^{2-}$ . The  $\Delta T/T$  signal changes the sign from positive to negative at the intermediate times and recovers back to zero at longer delay times, indicating formation of intermediate charge-separated species. These results confirm the electron transfer to the excited Au NRs is responsible for the TPPL quenching of Au NRs.

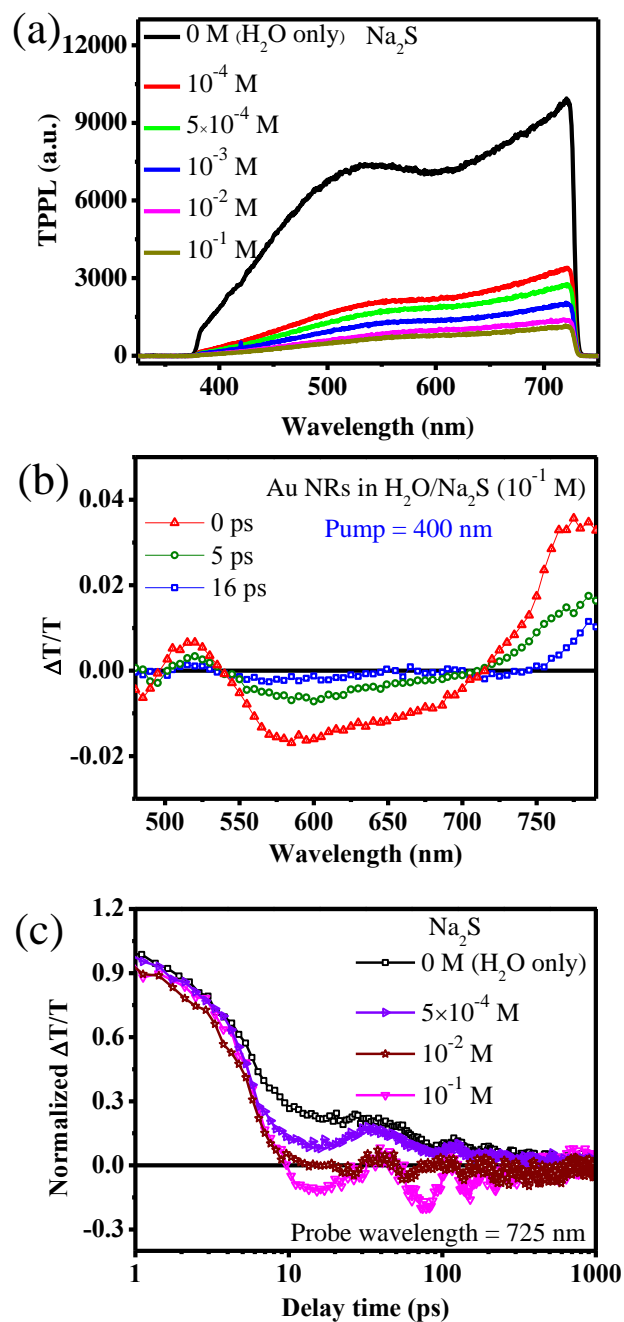


**Figure 3.10:** (a) Relative TPPL intensities of Au NRs in H<sub>2</sub>O with different concentrations of Na<sub>2</sub>S. (b) Transient absorption spectra of Au NRs in H<sub>2</sub>O with the concentrations of Na<sub>2</sub>S is 10<sup>-1</sup> M at the different delay times under excitation at 400 nm. (c) Single wavelength dynamics of Au NRs in H<sub>2</sub>O with different concentrations of Na<sub>2</sub>S (0, 5 × 10<sup>-4</sup>, 10<sup>-2</sup> and 10<sup>-1</sup> M) probed at 725 nm.

### 3.6 Conclusion

PEG capped Au NRs well dispersed in various organic solvents have been



prepared to study the solvent effects on the TPPL properties and ultrafast dynamics of Au NRs. The TPPL intensities of Au NRs in different organic solvents (such as DMF, DEG, CH<sub>3</sub>OH, C<sub>2</sub>H<sub>5</sub>OH, CH<sub>3</sub>CN, DMSO, and THF) and mixture solvents were found to be significantly lower than that in H<sub>2</sub>O. Ultrafast time-resolved transient absorption and pump-probe measurements have been performed on Au NRs in DMF and DEG to understand the underlying quenching mechanisms. Different from the decay behaviors of Au NRs in H<sub>2</sub>O, an additional transient species was observed in Au NRs in DMF or DEG upon photo-excitation. This additional transient species was found to appear on a time scale of tens of picoseconds and subsequently disappear on a time scale of nanoseconds. This intermediate state is ascribed to the charge separated species. The observation of this transient species serves as a direct evidence to support that the observed TPPL quenching in organic solvents is due to electron transfer from electron-donating solvents to the excited Au NRs. The charge transfer mechanism was further supported by the observation that the TPPL intensity of Au NRs in H<sub>2</sub>O was found to be quenched by nearly 5.0-fold in the presence of S<sup>2-</sup>. These studies will help to understand the fundamental mechanisms of TPPL of gold nanoparticles and its quenching behavior, which provide useful insight on the choice of surface conjugated surfactants to improve their TPPL efficiency for various biological applications.

## References

- (1) Link, S. and Ei-Sayed, M.A. *Annu. Rev. Phys. Chem.* **2003**, *54*, 331-366.
- (2) Hartland, G.V. *Chem. Rev.* **2011**, *111*, 3858-3887.

- (3) Lu, X., Rycenga, M., Skrabalak, S.E., Wiley, B. and Xia, Y., *Annu. Rev. Phys. Chem.* **2009**, *60*, 167-192.
- (4) Zhao, J., Pinchuk, A.O., McMahon, J.M., Li, S.Z., Ausman, L.K., Atkinson, A.L. and Schatz, G.C. *Acc. Chem. Res.* **2008**, *41*, 1710-1720.
- (5) Kelly, K.L., Coronado, E., Zhao, L.L. and Schatz, G.C. *J. Phys. Chem. B* **2003**, *107*, 668-677.
- (6) Imura, K., Nagahara, T. and Okamoto, H. *J. Phys. Chem. B* **2005**, *109*, 13214-13220.
- (7) Guan, Z.P., Polavarapu, L. and Xu, Q.H. *Langmuir* **2010**, *26*, 18020-18023.
- (8) Jain, P.K., Lee, K.S., El-Sayed, I.H. and El-Sayed, M.A. *J. Phys. Chem. B* **2006**, *110*, 7238-7248.
- (9) Jin, R.C., Jureller, J.E., Kim, H.Y. and Scherer, N.F. *J. Am. Chem. Soc.* **2005**, *127*, 12482-12483.
- (10) Guan, Z., Gao, N., Jiang, X.-F., Yuan, P., Han, F. and Xu, Q.-H. *J. Am. Chem. Soc.* **2013**, *135*, 7272-7277.
- (11) Jiang, X.-F., Pan, Y., Jiang, C., Zhao, T., Yuan, P., Venkatesan, T. and Xu, Q.-H. *J. Phys. Chem. Lett.* **2013**, *4*, 1634-1638.
- (12) Chen, G., Wang, Y., Yang, M.X., Xu, J., Goh, S.J., Pan, M. and Chen, H.Y. *J. Am. Chem. Soc.* **2010**, *132*, 3644-3645.
- (13) Tian, Z.Q., Ren, B., Li, J.F. and Yang, Z.L. *Chem. Commun.* **2007**, 3514-3534.
- (14) Sapsford, K.E., Berti, L. and Medintz, I.L. *Angew. Chem.-Int. Edit.* **2006**, *45*, 4562-4588.
- (15) Aslan, K. and Geddes, C.D. *Chem. Soc. Rev.* **2009**, *38*, 2556-2564.
- (16) Cheng, D.M. and Xu, Q.H. *Chem. Commun.* **2007**, 248-250.
- (17) Mohamed, M.B., Volkov, V., Link, S. and El-Sayed, M.A. *Chem. Phys. Lett.* **2000**, *317*, 517-523.
- (18) Zijlstra, P., Chon, J.W.M. and Gu, M. *Nature* **2009**, *459*, 410-413.
- (19) Wang, H.F., Huff, T.B., Zweifel, D.A., He, W., Low, P.S., Wei, A. and Cheng, J.X. *Proc. Natl. Acad. Sci. U. S. A.* **2005**, *102*, 15752-15756.
- (20) Zhao, T.T., Shen, X.Q., Li, L., Guan, Z.P., Gao, N.Y., Yuan, P.Y., Yao, S.Q., Xu, Q.H. and Xu, G.Q. *Nanoscale* **2012**, *4*, 7712-7719.
- (21) Jiang, C., Zhao, T., Yuan, P., Gao, N., Pan, Y., Guan, Z., Zhou, N. and Xu, Q.-H. *ACS Appl. Mater. Interfaces* **2013**, *5*, 4972-4977.
- (22) Chen, H., Shao, L., Li, Q. and Wang, J. *Chem. Soc. Rev* **2013**, *42*, 2679-2724.
- (23) Li, C.Z., Male, K.B., Hrapovic, S. and Luong, J.H.T. *Chem. Commun.* **2005**,

3924-3926.

- (24) Yu, C.X. and Irudayaraj, J. *Anal. Chem.* **2007**, *79*, 572-579.
- (25) Durr, N.J., Larson, T., Smith, D.K., Korgel, B.A., Sokolov, K. and Ben-Yakar, A. *Nano Lett.* **2007**, *7*, 941-945.
- (26) Chen, C.C., Lin, Y.P., Wang, C.W., Tzeng, H.C., Wu, C.H., Chen, Y.C., Chen, C.P., Chen, L.C. and Wu, Y.C. *J. Am. Chem. Soc.* **2006**, *128*, 3709-3715.
- (27) Wei, Q.S., Ji, J. and Shen, J.C. *Macromol. Rapid Commun.* **2008**, *29*, 645-650.
- (28) Huang, X.H., El-Sayed, I.H., Qian, W. and El-Sayed, M.A. *J. Am. Chem. Soc.* **2006**, *128*, 2115-2120.
- (29) Yu, K., Polavarapu, L. and Xu, Q.-H. *J. Phys. Chem. A* **2011**, *115*, 3820-3826.
- (30) Dondapati, S.K., Ludemann, M., Muller, R., Schwieger, S., Schwemer, A., Handel, B., Kwiatkowski, D., Djiango, M., Runge, E. and Klar, T.A. *Nano Lett.* **2012**, *12*, 1247-1252.
- (31) Park, J., Huang, J.Y., Wang, W., Murphy, C.J. and Cahill, D.G. *J. Phys. Chem. A* **2012**, *116*, 26335-26341.
- (32) Cao, J., Galbraith, E.K., Sun, T. and Grattan, K.T.V. *Sens. Actuators B-Chem.* **2012**, *169*, 360-367.
- (33) Niidome, T., Yamagata, M., Okamoto, Y., Akiyama, Y., Takahashi, H., Kawano, T., Katayama, Y. and Niidome, Y. *J. Control. Release* **2006**, *114*, 343-347.
- (34) Nikoobakht, B. and El-Sayed, M.A. *Chem. Mat.* **2003**, *15*, 1957-1962.
- (35) Jana, N.R., Gearheart, L. and Murphy, C.J. *J. Phys. Chem. B* **2001**, *105*, 4065-4067.
- (36) Thierry, B., Ng, J., Krieg, T. and Griesser, H.J. *Chem. Commun.* **2009**, 1724-1726.
- (37) Love, J.C., A., E.L., K., K.J., G., N.R. and M., W.G. *Chem. Rev.* **2005**, *105*, 1103-1169.
- (38) Wu, C.L. and Xu, Q.H. *Langmuir* **2009**, *25*, 9441-9446.
- (39) Vigderman, L., Khanal, B.P. and Zubarev, E.R. *Adv. Mater.* **2012**, *24*, 4811-4841.
- (40) Lee, K.S. and El-Sayed, M.A. *J. Phys. Chem. B* **2005**, *109*, 20331-20338.
- (41) Marinakos, S.M., Chen, S.H. and Chilkoti, A. *Anal. Chem.* **2007**, *79*, 5278-5283.
- (42) Zhao, T.T., Wu, H., Yao, S.Q., Xu, Q.H. and Xu, G.Q. *Langmuir* **2010**, *26*, 14937-14942.

- (43) Jiang, C.F., Guan, Z.P., Lim, S.Y.R., Polavarapu, L. and Xu, Q.H. *Nanoscale* **2011**, *3*, 3316-3320.
- (44) Lakowicz, J.R., *Principles of Fluorescence Spectroscopy*. 2006, Springer. p. 335-341.
- (45) Kandori, H., Kemnitz, K. and Yoshihara, K. *J. Phys. Chem.* **1992**, *96*, 8042-8048.
- (46) Xu, Q.-H., Scholes, G.D., Yang, M. and Fleming, G.R. *J. Phys. Chem. A* **1999**, *103*, 10348-10358.
- (47) Castner, E.W., Kennedy, D. and Cave, R.J. *J. Phys. Chem. A* **2000**, *104*, 2869-2885.
- (48) Morandeira, A., Fürstenberg, A., Gumy, J.-C. and Vauthey, E. *J. Phys. Chem. A* **2003**, *107*, 5375-5383.
- (49) Morandeira, A., Fürstenberg, A. and Vauthey, E. *J. Phys. Chem. A* **2004**, *108*, 8190-8200.
- (50) Link, S., Burda, C., Mohamed, M.B., Nikoobakht, B. and El-Sayed, M.A. *Phys. Rev. B* **2000**, *61*, 6086-6090.
- (51) Park, S., Pelton, M., Liu, M., Guyot-Sionnest, P. and Scherer, N.F. *J. Phys. Chem. C* **2006**, *111*, 116-123.
- (52) Jiang, Y., Wang, H.-Y., Xie, L.-P., Gao, B.-R., Wang, L., Zhang, X.-L., Chen, Q.-D., Yang, H., Song, H.-W. and Sun, H.-B. *J. Phys. Chem. C* **2010**, *114*, 2913-2917.

## **Chapter 4. Broadband Ultrafast Carrier Dynamics of Graphene Oxide and Reduced Graphene Oxide**

### **4.1 Introduction**

Graphene is a one-atom-thick two dimensional (2D) sheet of  $sp^2$  carbon atoms that are densely packed in a honeycomb crystal lattice.<sup>1,2</sup> It exhibits unusual electrical and optical properties due to its unique structure. The charge carriers in graphene behave like a 2D gas of mass less Dirac fermions.<sup>1,3</sup> The electrons in graphene can cover sub-micrometer distances at room temperature without scattering, which makes graphene an interesting material for optoelectronics.<sup>3,4</sup> In recent years, the research on graphene has been sparked by their appeal in technological applications as well as for fundamental scientific understanding of the outstanding optical and electronic properties.<sup>2</sup> Several methods such as epitaxial growth,<sup>5</sup> chemical vapor deposition (CVD),<sup>6</sup> physical exfoliation,<sup>7</sup> solvent-assisted exfoliation<sup>8, 9</sup> and reduction of graphene oxide (GO)<sup>10-13</sup> have been reported to prepare graphene. Among all these methods, the use of chemically derived GO as a precursor for the large scale production of graphene has paid special attention for solution processed applications owing to the high solubility of GO over graphene in various solvents.<sup>13</sup>

GO is an atomically thin sheet of graphite oxide, first reported in 1859 by Brodie.<sup>14</sup> It can be prepared by oxidative exfoliation of graphite into atomically thin carbon sheets decorated with oxygen-containing functional groups.<sup>10, 11, 13, 15</sup> GO sheets

contain a mixture of electronically conducting  $sp^2$  carbon and insulating  $sp^3$  carbon sites. As-prepared GO usually behaves like insulator with large number of  $sp^3$  carbon sites.<sup>11, 15</sup> Subsequently, GO can be transformed into semiconductor or graphene-like semi-metal by the controlled deoxidation.<sup>11</sup> Many kinds of reduction methods have been reported, such as chemical,<sup>11, 12</sup> electrical<sup>16</sup>, thermal,<sup>17</sup> and photo-thermal reduction<sup>18-20</sup>. The electronic mobility of the reduced GO is less compared to the mechanically cleaved graphene due to the defects present in reduced GO.<sup>11</sup> As the extent of reduction is different at various reduction conditions, the electronic and optical properties of the reduced GO depend on the type of reduction process.<sup>11, 12, 15</sup> Moreover, GO itself exhibits interesting optoelectronic properties<sup>21-23</sup> and has been utilized in various applications such as catalysis<sup>24-26</sup>, bio-sensing<sup>27</sup>, flexible memory devices.<sup>28</sup>

Owing to the unique properties, solution processing ability and potential applications of GO and reduced GO,<sup>17</sup> the investigation of their ultrafast electron relaxation dynamics is vital for the realization of graphene-based electronic devices in the future.<sup>4</sup> Ultrafast carrier dynamics of graphite has been reported by Breusing et al.<sup>29</sup> Recently, Jahan et al.<sup>5</sup> found that the carrier relaxation time in epitaxial graphene was inversely proportional to the degree of crystalline disorder. Huang et al.<sup>30</sup> employed the transient absorption microscopy to investigate the charge carrier dynamics of multilayer epitaxial graphene. Ultrafast dynamics of CVD-grown multilayer graphene has been investigated by Obraztsov et al.<sup>31</sup> and Shang et al.,<sup>32</sup> separately. Very recently,

a few research groups have paid special attention to the studies of carrier relaxation dynamics of solution processing reduced GO.<sup>33-36</sup> So far, most of the above-mentioned studies on the ultrafast dynamics of different kinds of graphene and GO related materials were performed using degenerate pump-probe measurements in the infrared region and less attention has been paid to the broadband (visible-infrared) electron relaxation properties using non-degenerate pump-probe measurements to understand the probe energy-dependence on the carrier relaxation time.<sup>29, 32, 37</sup> Moreover, the broadband transient absorption spectra of GO and reduced GO have been very rarely studied.<sup>38</sup>

Herein, broadband ultrafast dynamics of GO in solution, GO and reduced GO films were investigated by employing transient absorption and pump-probe spectroscopy with 400 nm pump and white light continuum probe. The carrier relaxation of GO in solution exhibited tri-exponential decay, which is independent of probe wavelength. However, the carrier relaxation of GO film was found to be faster than GO in solution and the relaxation time increased with the decrease of probe wavelength. More interestingly, the transient differential transmission ( $\Delta T/T$ ) of reduced GO exhibits broadband saturable absorption unlike GO in solution or GO film. The carrier relaxation of reduced GO exhibits bi-exponential decay and the relaxation processes become much faster compared to GO in solution or GO films.

## 4.2 Experimental Section

### Preparation of Graphene oxide:

GO was prepared from graphite via a modified Hummers and Offeman method.<sup>13</sup> In a typical procedure, 1.5 g graphite flakes (Asbury Carbons Ltd.) and 1.0 g NaNO<sub>3</sub> were placed in a 500 mL round bottom flask. 45 mL of concentrated H<sub>2</sub>SO<sub>4</sub> was subsequently added into the flask. The mixture was stirred overnight at room temperature. 6.0 g KMnO<sub>4</sub> was then slowly added into the mixture in a ice bath to avoid rapid heat evaluation. The flask was shifted to an oil bath after 4 hrs and the reaction mixture was stirred at 35 °C for another 2 hrs. The temperature was slowly increased to 60 °C and stirred for 4 hrs. Finally, the reaction mixture was added into 40 mL of water and stirred at 90 °C for 5 hrs. The reaction was ended by adding 10 mL of 30% H<sub>2</sub>O<sub>2</sub>, which resulted in a change of color from yellow to brown. The warm solution was then filtered and washed with 5% HCl and water. The obtained solid was dissolved in water and sonicated to exfoliate oxidized graphene. The oxidized graphene was centrifuged at 1000 rpm for 2 min. After removing all visible graphite particles, it was again centrifuged at 15,000 rpm for 2 hrs. This washing procedure was repeated until the pH became 4-5. For complete oxidation, the above dried GO was further treated with 70% HNO<sub>3</sub> (10 mL of HNO<sub>3</sub>/100 mg of GO). The mixture was sonicated for 8 hrs at 60 °C and the sediment was dispersed in water. The obtained GO was purified by washing multiple times with ethanol and water, and then completely dried using a rotary evaporator. The dried GO was finally dispersed in water for further characterization.



The GO in water was spin-coated onto a silica substrate for Atomic Force Microscopy (AFM) measurement.

#### **Preparation of graphene oxide and reduced Graphene oxide films:**

The as-prepared GO sheets were dissolved in water by ultrasonication with a concentration of 3mg/mL. GO film was prepared by spin coating the GO solution onto clean oxygen plasma treated quartz slides at a speed of 1000 rpm and the films were dried at 70 °C. The spin coating was repeated for 8 times on each slide. The reduced GO film was prepared by annealing the as-prepared GO film in vacuum at 1000°C for 30 min.

#### **Transient absorption and pump-probe measurements:**

The ultrafast relaxation dynamics of GO and reduced GO was measured by using transient absorption and pump-probe experiment, which was performed by using a femtosecond Ti:sapphire laser system (Spectra Physics). The laser pulses were generated from a mode-locked Ti:sapphire oscillator seeded regenerative amplifier with a pulse energy of 2 mJ at 800 nm and a repetition rate of 1 kHz. The 800 nm laser beam was split into two portions. The larger portion of the beam was passed through a BBO crystal to generate the 400 nm pump beam by frequency-doubling. A residual portion of the beam was used to generate white light continuum in a 1 mm sapphire plate. The white light continuum was split into two beams, one as probe and the other as a reference to correct for pulse-to-pulse intensity fluctuations. The signal and

reference beams were detected by photodiodes that are connected to lock-in amplifiers and the computer. The pump beam is focused onto the film with a beam size of 300  $\mu\text{m}$  and overlaps the smaller-diameter (100  $\mu\text{m}$ ) probe beam. The delay between the pump and probe pulses was varied by a computer-controlled translation stage (Newport, ESP 300). The pump beam was modulated by an optical chopper at a frequency of 500 Hz. The spectral resolution is 2 nm for transient absorption spectra.

### 4.3 Absorption and Photoluminescence of Graphene Oxide

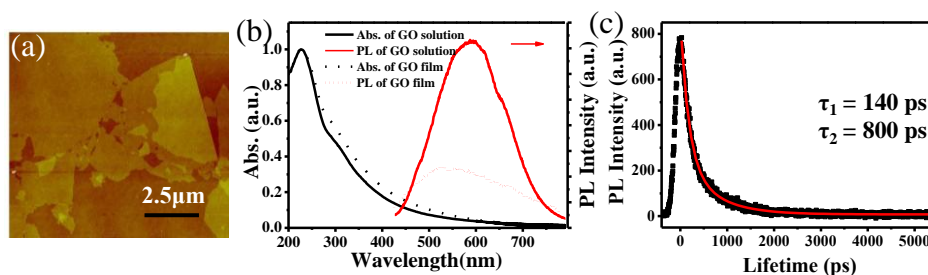


**Figure 4.1:** (a) AFM image of GO sheet. (b) UV-visible absorption spectra and photoluminescence (PL) spectra of GO at an excitation wavelength of 400 nm. (c) Time-resolved PL of GO solution measured via time correlated single photon counting (TCSPC) system. The detection wavelength was at 580 nm and no wavelength dependence of the PL lifetimes was found.

The as-prepared GO sheets are highly soluble in water due to the oxygen-containing functional groups, such as carboxyl, epoxide and hydroxyl groups, which are present on the basal plane or at the edges of GO sheet. The AFM image (Figure 4.1a) shows the wide size distributions of GO sheets ranging from 300 nm to a few  $\mu\text{m}$  with average thickness of about 1 nm, which indicates that most of the GO sheets are single layer. Figure 4.1b shows the absorption and photoluminescence (PL) spectra of GO. The two characteristic absorption peaks at 223 nm and 320 nm were

believed to originate from  $\pi$ - $\pi^*$  and  $n$ - $\pi^*$  transitions of C=C and C=O bands, respectively.<sup>39</sup> Under excitation at 400 nm, GO displays a broad emission band at 580 nm. The PL of GO originates from the radiative recombination of electron-hole pairs localized within semiconducting quasi-molecular fluorophores, which are formed by the electronic coupling of carboxylic acids with nearby  $\pi$ -conjugated  $sp^2$  domains.<sup>21, 23</sup> The broad emission spectrum of GO reflects the broad size distribution of fluorescent domains in the GO sheet, which has been utilized for bio-imaging and bio-sensing.<sup>40, 41</sup> The PL lifetime decay of GO was measured by using time correlated single photon counting (TCSPC) system under excitation at 400 nm using femtosecond laser pulses. The decay dynamics shows bi-exponential decay with an initial fast relaxation of  $\tau_1=140$  ps followed by a slower relaxation of  $\tau_2=800$  ps (Figure 4.1c). As a result of its broadband fluorescence in the visible and near IR regions, GO has drawn much attention in the application of low cost and large area optoelectronic devices. So it is important to understand how these optical properties changes when they are formed as films.

#### **4.4 Carrier Dynamics of Graphene Oxide**

The ultrafast carrier dynamics of GO solution and film were investigated by utilizing femtosecond transient absorption spectroscopy. GO films were prepared by spin coating the GO solution onto the quartz substrates. It has been previously reported that the femtosecond laser pulses with high pulse energy can reduce GO into reduced GO.<sup>20</sup>

Here we performed all the transient absorption measurements at very low excitation fluence of  $2.4 \mu\text{J}\cdot\text{cm}^{-2}$ . The transmittance of GO before and after the experiment were measured to ensure that there was no reduction taking place during measurements.

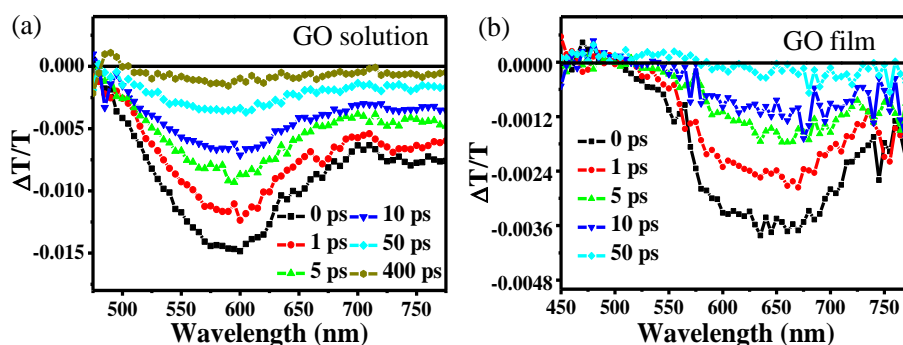


**Figure 4.2:** Transient absorption spectra of GO in water (a) and GO film (b) at different delay times upon excitation at 400 nm.

Figures 4.2a&b shows the transient absorption spectra of GO solution and film at different delay times upon excitation at 400 nm. Both of them share the similar broad transient absorption profile with negative  $\Delta T/T$ , which spans from visible to near Infrared. This negative  $\Delta T/T$  signal is ascribed to the transient absorption signal, which can be dominated by excited state absorption. For GO, this broadband excited state absorption is likely attributed to the excited-state absorption or multiphoton absorption due to quasi-molecular fluorophores arising from the different sizes of nanometer-scale  $sp^2$  clusters present in the GO sheets.<sup>23</sup> However, the absorption maximum of the transient absorption spectra of GO film ( $|\Delta T/T|_{\text{max}}=650 \text{ nm}$ ) is red shifted compared to that of GO solution ( $|\Delta T/T|_{\text{max}}=585 \text{ nm}$ ). This red shift might be attributed to the aggregation of the GO sheets in film, where the strong electronic

coupling exists between quasi-fluorescent localized  $\pi$ -conjugated  $sp^2$  clusters of nearby GO sheets.

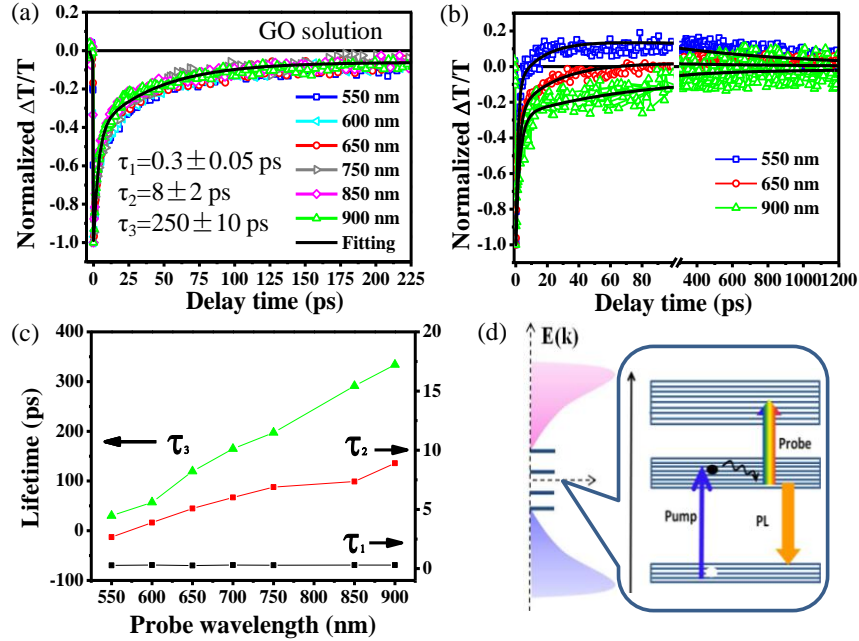


**Figure 4.3:** Carrier relaxation dynamics probed at different wavelength of GO in water (a) and GO film (b). (c) Probe wavelength dependent time constants for carrier relaxation processes of GO films ( $\tau_1$ ,  $\tau_2$ ,  $\tau_3$ ). (d) Schematic band structure of semiconducting  $\pi$ -conjugated  $sp^2$  domains in GO sheets.

Figure 4.3a shows the single wavelength dynamics of GO in water at different probe wavelength. It can be clearly observed that the decay times are independent of probe wavelength. The relaxation dynamics of GO in water can be well fitted with tri-exponential decays with time constants of  $\tau_1=0.3$  ps (20%),  $\tau_2=8$  ps (55%) and  $\tau_3=250$  ps (25%). In general, the fast relaxation  $\tau_1$  can be attributed to the thermalization via electron-electron scattering and  $\tau_2$  corresponds to the intraband relaxation process of electron-phonon scattering. The slower time constant  $\tau_3$  of GO is ascribed to the interband carrier recombination of quasi-fluorescent  $\pi$ -conjugated  $sp^2$  clusters in GO sheets. The semiconducting quasi-fluorescent  $\pi$ -conjugated  $sp^2$  clusters

in GO sheets possess large energy gap, which leads to the slow interband carrier relaxation upon the excitation of GO in water. Such kind of slow relaxation has not been observed in graphene and the relaxation times in graphene are usually ranges from 100 fs to few ps. The broad PL spectrum observed in steady-state fluorescence measurements further supports the presence of radiative recombination of electron-hole pair and large energy band gap of quasi-fluorescent localized  $\pi$ -conjugated  $sp^2$  clusters.

As shown in Figure 4.3b, it is obviously observed that the average carrier relaxation is faster in GO films compared to that of suspended-GO in solution. The faster decay is likely due to the inter sheet electron transfer within the GO film and the interactions between the carriers and the substrate. In the previous studies on conjugated polymers, faster relaxation time was observed in polymer films respect to that of polymers in solution due to the close contacts between chains favor interchain transport and increased the transfer rate.<sup>42</sup> Moreover, the substrate would can also provide an additional relaxation channel for the supported samples compared to the suspended one.<sup>43</sup> GO sheets are in close contact each other in GO films unlike in GO solution. So there will be strong electronic coupling between the nearby GO sheets, which causes the faster relaxation due to inter-sheet electron transfer after photo excitation.

It should be also noticed that unlike GO in water, the carrier relaxation time constants of GO films are probe wavelength dependent and the relaxation becomes

faster with the decrease of probe wavelength (Figure 4.3b&c). When the transient absorption was probed at shorter wavelength (550 nm), the  $\Delta T/T$  becomes positive at time delays beyond around 10 ps and then decays slowly to zero. The positive  $\Delta T/T$  could be due to the delayed emission arises from the recombination of charge-separated pairs into neutral excitons in GO sheets. Similar behavior has been previously observed in semiconductor polyfluorene system.<sup>44</sup> In this case, the probe wavelength relaxation dynamics can be fitted with four-exponential decays and the fitted parameters are summarized in Table 4-1.

**Table 4-1:** Lifetimes of the transient absorption signal of GO films at different probe wavelengths under excitation at 400 nm.

Probe wavelength (nm)	550nm	600nm	650nm	700nm	750nm	850nm	900nm
A1	-26%	-23%	-21%	-20%	-20%	-20%	-20%
$\tau_1$ (ps)	0.28	0.30	0.26	0.30	0.29	0.30	0.30
A2	-65%	-61%	-61%	-60%	-60%	-60%	-60%
$\tau_2$ (ps)	2.65	3.89	5.08	6.01	6.88	7.35	8.90
A3	-21%	-21%	-20%	-20%	-20%	-20%	-20%
$\tau_3$ (ps)	30	57	120	165	198	291	334
A4	12%	5%	1%	-	-	-	-
$\tau_4$ (ps)	800	800	800	-	-	-	-

Similar to GO solution, the first three time constants of the carrier relaxation in GO films correspond to electron-electron scattering, electron-phonon scattering and recombination of electron-hole pairs into neutral excitons. The contribution of fourth component ( $\tau_4$ ) arising from the positive  $\Delta T/T$  increases with the decrease of probe wavelength. The time constant  $\tau_4 = 800$  ps is almost similar to the lifetime of the GO fluorescence observed by TCSPC measurement, which further supports the origin of the positive  $\Delta T/T$  signal is due to the delayed emission of GO. The delayed emission was only observed at shorter probe wavelengths obviously, where the excited-state

absorption decays rapidly and the emission dominated subsequently. But in the case of longer probe wavelengths in GO film, the excited-state absorption contribution dominates the overall transient signal, so we did not observed the delayed emission just as in GO solution, where the excited-state absorption decays slowly. Furthermore, we have measured the intensity dependent carrier decay of GO in solution and film at their absorption maxima. The peak  $\Delta T/T$  increases proportionally with the increase of pump intensity, which confirms that the change in absorption of the probe is due to state-filling effects (Figure 4.4&4.5).

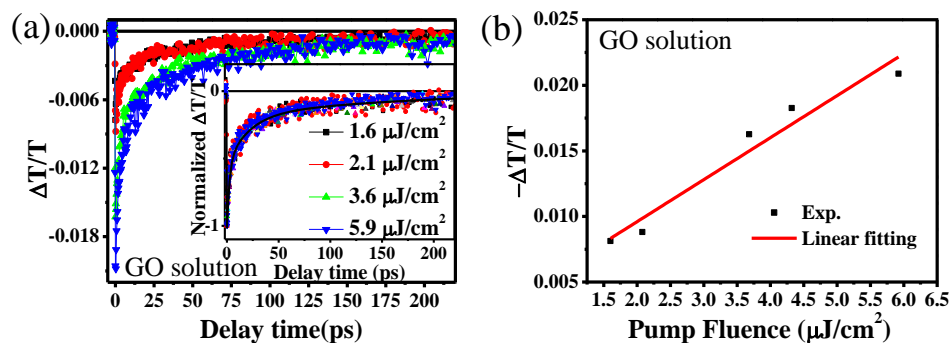


**Figure 4.4:** (a) Carrier relaxation dynamics of GO solution probed at wavelength of 600 nm upon different pump fluence at 400 nm. The insets show the normalized data. (b) The absorption maximum after photo excitation is plotted for various pump fluences for GO solution.

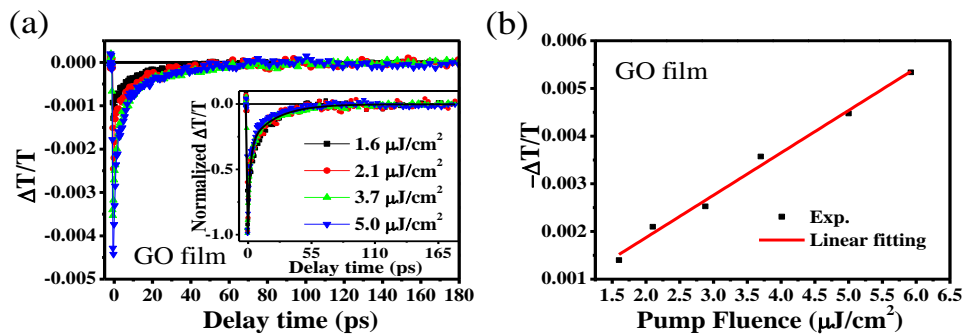


**Figure 4.5:** (a) Carrier relaxation dynamics of GO film probed at wavelength of 600 nm upon different pump fluence at 400 nm. The insets show the normalized data. (b) The absorption maximum after photo excitation is plotted for various fluences for GO film.



These results indicate that the transient absorption spectra and relaxation dynamics of both GO in solution and GO in films are completely different from that of pristine graphene that have been previously reported.<sup>37</sup> The transient absorption spectra of pure graphene show the transient bleaching (positive  $\Delta T/T$ ) upon the photo excitation.<sup>29, 45</sup> Pristine graphene is a broadband saturable absorber with very fast decay time ranging from 60 fs to 2 ps,<sup>32, 45</sup> whereas GO is a broadband excited state absorber with slow relaxation time. Our results predict that GO is a potential candidate as optical limiting material, which would be systematically studied in Chapter 5.

## **4.5 Carrier Dynamics of Reduced Graphene Oxide**

The insulating nature of the as-prepared GO limits their applications for the fabrication of graphene-based electronic devices. So it needs to convert the as-prepared GO into graphene by removing oxygen defects in GO. The reduced GO is not soluble in water like graphene, so we have prepared reduced GO films by thermal annealing of GO films and their ultrafast dynamics behaviors have been studied. The thermal reduction of GO films was carried out by annealing the GO films at 1000°C. The prepared and reduced GO films were characterized by UV-visible transmittance and Raman spectroscopy measurements, as shown in Figure 4.6.

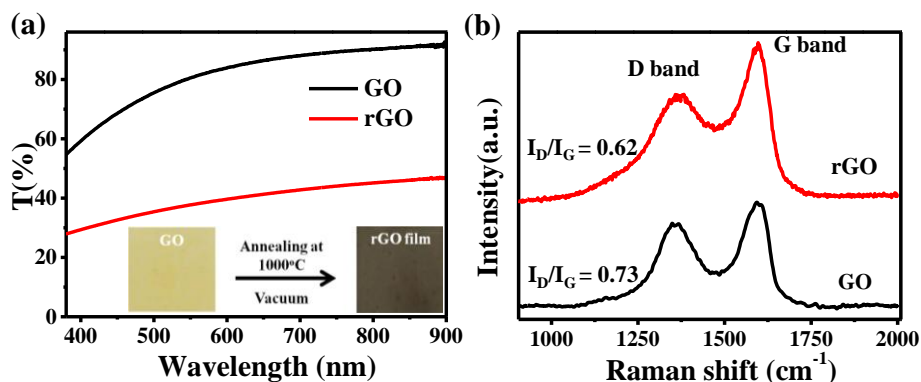


**Figure 4.6:** (a) Transmittance spectra of the as-prepared GO and reduced GO (rGO) films. The inset shows the sample colors with a white background. (b) Raman spectra of as-prepared and reduced GO films.

Figure 4.6a shows the comparison of the transmittance spectra of GO and reduced GO film. The transmittance of the GO film is about 80-85% in the visible to infrared range, and decreases to around 40% when GO film was converted to reduced GO film. The decrease of the transmittance over broad range of wavelengths is due to the restoration of  $sp^2$   $\pi$ -conjugated network by deoxygenation of GO upon reduction. The photographs of the GO and reduced GO films with a white background are shown in the inset of Figure 4.6a. The light yellow color of the thin GO film changes to black color upon thermal reduction of GO.

The Raman spectra of the as-prepared GO and reduced GO are shown in Figure 4.6b. The Raman spectra of GO displayed two peaks at  $1354\text{ cm}^{-1}$  and  $1595\text{ cm}^{-1}$ , corresponding to D and G-bands, respectively. The G-band is attributed to an  $E_{2g}$  phonon mode of  $sp^2$  bonded carbon atoms and the D-band is related to the local defects and disordered graphite.<sup>18,20</sup> These two peaks were slightly red shifted to  $1358\text{ cm}^{-1}$  and  $1598\text{ cm}^{-1}$  and become broader for reduced GO. The ratios of the intensities of the D

and G-bands ( $I_D/I_G$ ) are usually indicates the quality of the graphitic structures and this ratio approaches zero for highly ordered pyrolytic graphite. Here the ratios obtained for GO and reduced GO are 0.73 and 0.62, respectively, which indicates that significant reduction of disordered sites upon reduction of GO.<sup>18</sup> The ultrafast carrier dynamics of reduced GO was measured at the similar experimental conditions as GO solution and GO films with excitation fluence of  $27 \mu\text{J}\cdot\text{cm}^{-2}$  at 400 nm.

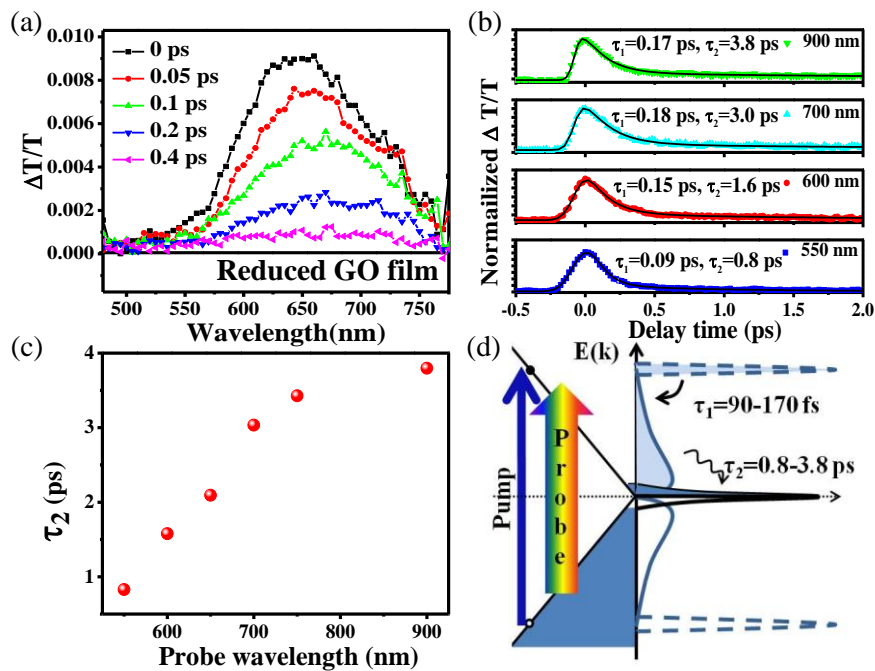


**Figure 4.7:** (a) Transient absorption spectra of reduced GO film at different time delays upon excitation at 400 nm. (b) Carrier relaxation dynamics of reduced GO probed at different wavelengths upon excitation at 400 nm. The solid lines are the analytical fits to the data using exponentials with two time constants:  $\tau_1$  and  $\tau_2$ . (c) Probe wavelength dependent time constant ( $\tau_2$ ) for carrier relaxation processes of reduced GO film (d) Schematic band structure of reduced GO showing intrinsic population near the Dirac point and its carrier relaxation via electron-electron scattering ( $\tau_1$ ) and electron-phonon scattering ( $\tau_2$ ).

Figure 4.7a&b shows the transient absorption spectra at different time delays and probe wavelength dependent ultrafast relaxation dynamics of reduced GO film, respectively. Obviously, the transient signal of reduced GO indicates an instantaneous

increase of transmittance in the visible range with the photo-excitation at 400 nm (positive  $\Delta T/T$ ). The profile of the transient absorption spectrum of reduced GO film with transient differential transmittance maximum at 650 nm, is quite similar to that of GO film. However, the sign of the transient signal ( $\Delta T/T$ ) is opposite to that of GO film. Moreover, the transient absorption of reduced GO decays very rapidly ( $\sim 0.8$ - $3.8$  ps) compared to that of GO film ( $\sim 30$ - $300$  ps).

The sign of the transient absorption and the decay times of reduced GO are quite similar to that of pristine graphene.<sup>5</sup> GO is a large band gap insulator type material, but the band gap can be significantly reduced by converting GO into reduced GO. The band gap of reduced GO depends on the efficiency of reduction process. Here in the present study, thermal reduction in vacuum at  $1000^\circ\text{C}$  for half an hour is efficient enough to convert GO into highly reduced GO, so the band gap of reduced GO can be very small and readily absorb almost all photons at any wavelength like pristine graphene (Figure 4.7d). Due to the Pauli blocking principle, the carriers generated by strong incident intensities quickly fill the valence bands, preventing further excitation of electrons at valence band and allowing photons transmitted absence of loss, which induced the observed broadband bleaching signal in the transient absorption spectra.<sup>45</sup> However, we did not expect a peak in the transient absorption of reduced GO, which has not been observed in pristine graphene.<sup>46</sup> The  $\Delta T/T$  peak in the transient absorption spectra of reduced GO could arise from the contribution of ultrafast emission from the residual quasi-molecular fluorophores present in the reduced GO sheets. The fact is

that, GO cannot be completely converted into perfect graphene by reduction methods and there are always defects present in the reduced GO and these are responsible for the weak PL. Previously, Lui et al.<sup>47</sup> reported ultrafast visible PL from graphene under ultrafast laser excitation. However, further experiments such as time-resolved PL using fluorescence up-conversion technique are needed to understand the ultrafast PL contribution to the transient signal. Recently, it has been demonstrated that graphene and their composites can be use for mode-locking of ultrashort lasers in the infrared region.<sup>45, 48, 49</sup> The transient absorption spectrum of reduced GO suggests that these materials can serve as a broadband saturable absorber ranging from visible to infrared.

**Table 4-2:** Lifetimes of the transient absorption signal of reduced GO film at different probe wavelengths under excitation at 400 nm.

Probe wavelength (nm)	$\tau_1$ (ps)	error	$\tau_2$ (ps)	error
550	0.09	0.01	0.83	0.11
600	0.15	0.01	1.58	0.36
650	0.19	0.01	2.09	0.51
700	0.18	0.01	3.03	0.49
750	0.19	0.01	3.43	0.42
900	0.16	0.02	3.80	1.47

Figure 4.7b shows the probe wavelength dependent carrier dynamics of reduced GO. It is obviously that the carrier relaxation decays are significantly faster compared to that of GO solution and film. The carrier decay can be well fitted using deconvoluted bi-exponential decays with time constants  $\tau_1=0.09-0.17$  ps and  $\tau_2=0.8-3.8$  ps. The time constants ( $\tau_1$  &  $\tau_2$ ) at different probe wavelengths are tabulated in the Table 4-2.

These time constants ( $\tau_1$  and  $\tau_2$ ) are consistent with the previously reported

excited state dynamics of near infrared excited graphene samples.<sup>5, 33, 35</sup> The fast relaxation time  $\tau_1$  and the slow relaxation time  $\tau_2$  have been assigned to the electron-electron scattering and the electron-phonon intraband scattering, respectively.<sup>5</sup> Electron-hole recombination could also contribute to the slow decay time. The time constants  $\tau_2$  of reduced GO film at different probe wavelength have summarized in Figure 4.7c. The slower recombination time  $\tau_2$  shows a clear increasing tendency as the probe wavelength down from 550 nm to 900 nm. The probe wavelength dependent decay is analogous to the cooling of quasi-equilibrium in semiconductors, where the electrons in the low energy level stays longer compared to these in the higher energy level.

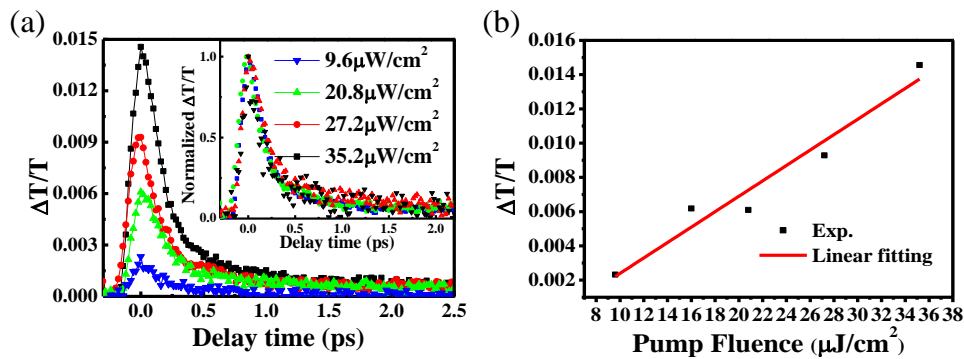


**Figure 4.8:** (a) Carrier relaxation dynamics of reduced GO film probed at wavelength of 650 nm upon different pump fluence at 400 nm. The insets show the normalized data. (b) The absorption maximum after photo-excitation is plotted for various pump fluences for reduced GO film.

The pump power dependence of the transmittance change at the probe wavelength 650nm for reduced GO film is shown in Figure 4.8 and the normalized data shows that the relaxation time is independent of excitation density. As depicted in Figure 4.8, the differential transmittance is proportional to the pump power, which confirms that the

band-filling effects in reduced GO films. These results suggest that the decay dynamics of reduced GO films are very similar to that of pristine graphene,<sup>5,47</sup> but fundamentally different from GO solution and film. The present comparative study is useful to understand the ultrafast relaxation properties of GO and reduced GO, which is important for development of GO-based low-cost optoelectronic devices.

## 4.6 Conclusion

Broadband ultrafast dynamics of as-prepared and reduced GO have been comparatively studied via femtosecond transient absorption and pump-probe spectroscopy. Transient absorption spectra of GO in solution or film exhibited broad excited-state absorption spanning from visible to infrared, which is due to the localized states arising from the small size of quasi-molecular  $sp^2$  clusters in GO sheets. The carrier relaxation dynamics of GO in solution was found to be independent of probe wavelength. However, the carrier relaxation becomes faster and probe wavelength dependent in GO films. The relaxation rate increased as the probe wavelength blue shifts, and the delayed emission was observed at the short probe wavelength around 550 nm after 10 ps of delay time. The aggregation of quasi-molecular  $sp^2$  clusters present in GO sheets is responsible for the faster relaxation in GO films compared to that of GO in solution. The transient absorption spectra of GO switched over from excited-state absorption to saturable absorption when GO was converted to reduced GO by thermal annealing. Carrier relaxation of photo-excited reduced GO film was found to be significantly faster compared to that of

GO and quite similar to that of pristine graphene. These results indicate that GO solution and films can be used as broadband optical limiting materials, whereas reduced GO can be used as broadband saturable absorber.

## References

- (1) Novoselov, K.S., Geim, A.K., Morozov, S.V., Jiang, D., Katsnelson, M.I., Grigorieva, I.V., Dubonos, S.V. and Firsov, A.A. *Nature* **2005**, *438*, 197-200.
- (2) Geim, A.K. and Novoselov, K.S. *Nat. Mater.* **2007**, *6*, 183-191.
- (3) Zhang, Y.B., Tan, Y.W., Stormer, H.L. and Kim, P. *Nature* **2005**, *438*, 201-204.
- (4) Castro Neto, A.H., Guinea, F., Peres, N.M.R., Novoselov, K.S. and Geim, A.K. *Rev. Mod. Phys.* **2009**, *81*, 109-162.
- (5) Dawlaty, J.M., Shivaraman, S., Chandrashekar, M., Rana, F. and Spencer, M.G. *Appl. Phys. Lett.* **2008**, *92*, 042116.
- (6) Reina, A., Jia, X.T., Ho, J., Nezich, D., Son, H.B., Bulovic, V., Dresselhaus, M.S. and Kong, J. *Nano Lett.* **2009**, *9*, 30-35.
- (7) Novoselov, K.S., Geim, A.K., Morozov, S.V., Jiang, D., Zhang, Y., Dubonos, S.V., Grigorieva, I.V. and Firsov, A.A. *Science* **2004**, *306*, 666-669.
- (8) Hernandez, Y., Nicolosi, V., Lotya, M., Blighe, F.M., Sun, Z.Y., De, S., McGovern, I.T., Holland, B., Byrne, M., Gun'ko, Y.K., Boland, J.J., Niraj, P., Duesberg, G., Krishnamurthy, S., Goodhue, R., Hutchison, J., Scardaci, V., Ferrari, A.C. and Coleman, J.N. *Nat. Nanotechnol.* **2008**, *3*, 563-568.
- (9) Li, X.L., Zhang, G.Y., Bai, X.D., Sun, X.M., Wang, X.R., Wang, E. and Dai, H.J. *Nat. Nanotechnol.* **2008**, *3*, 538-542.
- (10) Becerril, H.A., Mao, J., Liu, Z., Stoltenberg, R.M., Bao, Z. and Chen, Y. *ACS Nano* **2008**, *2*, 463-470.
- (11) Eda, G., Fanchini, G. and Chhowalla, M. *Nat. Nanotechnol.* **2008**, *3*, 270-274.
- (12) Gilje, S., Han, S., Wang, M., Wang, K.L. and Kaner, R.B. *Nano Lett.* **2007**, *7*, 3394-3398.
- (13) Hummers, W.S. and Offeman, R.E. *J. Am. Chem. Soc.* **1958**, *80*, 1339-1339.
- (14) Brodie, B.C. *Phil. Trans. R. Soc. Lond. A* **1859**, *149*, 249-259.
- (15) Stankovich, S., Dikin, D.A., Piner, R.D., Kohlhaas, K.A., Kleinhammes, A., Jia, Y., Wu, Y., Nguyen, S.T. and Ruoff, R.S. *Carbon* **2007**, *45*, 1558-1565.
- (16) Ekiz, O.O., Urel, M., Guner, H., Mizrak, A.K. and Dana, A. *Acs Nano* **2011**, *5*,



2475-2482.

- (17) Li, D., Muller, M.B., Gilje, S., Kaner, R.B. and Wallace, G.G. *Nat. Nanotechnol.* **2008**, *3*, 101-105.
- (18) Abdelsayed, V., Moussa, S., Hassan, H.M., Aluri, H.S., Collinson, M.M. and El-Shall, M.S. *J. Phys. Chem. Lett.* **2010**, *1*, 2804-2809.
- (19) Sokolov, D.A., Shepperd, K.R. and Orlando, T.M. *J. Phys. Chem. Lett.* **2010**, *1*, 2633-2636.
- (20) Zhang, Y.L., Guo, L., Wei, S., He, Y.Y., Xia, H., Chen, Q.D., Sun, H.B. and Xiao, F.S. *Nano Today* **2010**, *5*, 15-20.
- (21) Gokus, T., Nair, R.R., Bonetti, A., Böhmler, M., Lombardo, A., Novoselov, K.S., Geim, A.K., Ferrari, A.C. and Hartschuh, A. *Acs Nano* **2009**, *3*, 3963-3968.
- (22) Loh, K.P., Bao, Q., Eda, G. and Chhowalla, M. *Nat. Chem.* **2010**, *2*, 1015-1024.
- (23) Galande, C., Mohite, A.D., Naumov, A.V., Gao, W., Ci, L., Ajayan, A., Gao, H., Srivastava, A., Weisman, R.B. and Ajayan, P.M. *Sci. Rep.* **2011**, *1*, 1-5.
- (24) Huang, J., Zhang, L., Chen, B., Ji, N., Chen, F., Zhang, Y. and Zhang, Z. *Nanoscale* **2010**, *2*, 2733-2738.
- (25) Lightcap, I.V., Murphy, S., Schumer, T. and Kamat, P.V. *J. Phys. Chem. Lett.* **2012**, *3*, 1453-1458.
- (26) Williams, G., Seger, B. and Kamat, P.V. *Acs Nano* **2008**, *2*, 1487-1491.
- (27) Morales-Narváez, E. and Merkoç, A. *Adv. Mater.* **2012**, *24*, 3298-3308.
- (28) Jeong, H.Y., Kim, J.Y., Kim, J.W., Hwang, J.O., Kim, J.-E., Lee, J.Y., Yoon, T.H., Cho, B.J., Kim, S.O., Ruoff, R.S. and Choi, S.-Y. *Nano Lett.* **2010**, *10*, 4381-4386.
- (29) Breusing, M., Ropers, C. and Elsaesser, T. *Phys. Rev. Lett.* **2009**, *102*, 086809.
- (30) Huang, L.B., Hartland, G.V., Chu, L.Q., Luxmi, Feenstra, R.M., Lian, C.X., Tahy, K. and Xing, H.L. *Nano Lett.* **2010**, *10*, 1308-1313.
- (31) Obraztsov, P.A.O.P.A., Rybin, M.G., Tyurnina, A.V., Garnov, S.V., Obraztsova, E.D., Obraztsov, A.N. and Svirko, Y.P. *Nano Lett.* **2011**, *11*, 1540-1545.
- (32) Shang, J.Z., Yu, T., Lin, J.Y. and Gurzadyan, G.G. *ACS Nano* *5*, 3278-3283.
- (33) Ruzicka, B.A., Werake, L.K., Zhao, H., Wang, S. and Loh, K.P. *Appl. Phys. Lett.* **2010**, *96*, 173106.
- (34) Ruzicka, B.A., Kumar, N., Wang, S., Loh, K.P. and Zhao, H. *J. Appl. Phys.* **2011**, *109*, 084322.

- (35) Kumar, S., Anija, M., Kamaraju, N., Vasu, K.S., Subrahmanyam, K.S., Sood, A.K. and Rao, C.N.R. *Appl. Phys. Lett.* **2009**, *95*, 191911.
- (36) Liu, Z.B., Zhao, X., Zhang, X.L., Yan, X.Q., Wu, Y.P., Chen, Y.S. and Tian, J.G. *J. Phys. Chem. Lett.* **2011**, *2*, 1972-1977.
- (37) Sun, D., Wu, Z.K., Divin, C., Li, X.B., Berger, C., de Heer, W.A., First, P.N. and Norris, T.B. *Phys. Rev. Lett.* **2008**, *101*, 157402.
- (38) Kaniyankandy, S., Achary, S.N., Rawalekar, S. and Ghosh, H.N. *J. Phys. Chem. C* **2011**, *115*, 19110-19116.
- (39) Eda, G., Lin, Y.Y., Mattevi, C., Yamaguchi, H., Chen, H.A., Chen, I.S., Chen, C.W. and Chhowalla, M. *Adv. Mater.* **2010**, *22*, 505-509.
- (40) Chen, J.L. and Yan, X.P. *Chem. Comm.* **2011**, *47*, 3135-3137.
- (41) Sun, X.M., Liu, Z., Welsher, K., Robinson, J.T., Goodwin, A., Zaric, S. and Dai, H.J. *Nano Res.* **2008**, *1*, 203-212.
- (42) Beljonne, D., Pourtois, G., Silva, C., Hennebicq, E., Herz, L., Friend, R., Scholes, G., Setayesh, S., Müllen, K. and Bredas, J. *Proc. Natl. Acad. Sci. U. S. A.* **2002**, *99*, 10982-10987.
- (43) Gao, B., Hartland, G., Fang, T., Kelly, M., Jena, D., Xing, H. and Huang, L. *Nano Lett.* **2011**, *11*, 3184-3189.
- (44) Xu, Q.-H., Moses, D. and Heeger, A.J. *Phys. Rev. B* **2004**, *69*, 113314.
- (45) Bao, Q.L., Zhang, H., Ni, Z.H., Wang, Y., Polavarapu, L., Shen, Z.X., Xu, Q.H., Tang, D.Y. and Loh, K.P. *Nano Res.* **2011**, *4*, 297-307.
- (46) Shang, J., Yu, T., Lin, J. and Gurzadyan, G.G. *ACS Nano* **2011**, *5*, 3278-3283.
- (47) Lui, C.H., Mak, K.F., Shan, J. and Heinz, T.F. *Phys. Rev. Lett.* **2010**, *105*, 127404.
- (48) Bonaccorso, F., Sun, Z., Hasan, T. and Ferrari, A.C. *Nat. Photonics.* **2010**, *4*, 611-622.
- (49) Jiang, Y., Wang, H.-Y., Xie, L.-P., Gao, B.-R., Wang, L., Zhang, X.-L., Chen, Q.-D., Yang, H., Song, H.-W. and Sun, H.-B. *J. Phys. Chem. C* **2010**, *114*, 2913-2917.

# **Chapter 5. Graphene Oxides as Tunable Broadband Nonlinear Optical Materials for Femtosecond Laser Pulses**

## **5.1 Introduction**

Since its invention in 1960,<sup>1</sup> laser has been widely used in many fields including electronics, medicine, information technology, entertainment, industries and military.<sup>2</sup> There is significant interest in developing nonlinear optical materials (optical limiting materials and saturable absorbers) to modulate the light intensity. Optical limiting materials display a decreased transmittance at higher input laser intensity, which can be utilized to protect eyes and sensitive instruments from laser induced damage.<sup>3</sup> In contrast, saturable absorbers display an increased transmittance at very high input laser intensity, which are useful for pulse compression, mode locking and Q-switching.<sup>4</sup>

In the past decade, significant efforts have been devoted to developing ideal broadband optical limiting materials.<sup>5-8</sup> Strong optical limiting activity has been observed in carbon based materials such as carbon nanotubes,<sup>9</sup> fullerenes<sup>2</sup> and carbon black suspensions,<sup>2</sup> and metal nanoparticles such as gold and silver.<sup>6, 10, 11</sup> These materials usually show saturable absorption at low input intensities and exhibit optical limiting activity at very high input intensities. The primary contribution to the optical limiting effect is nonlinear scattering, which is due to formation of solvent micro-bubbles at high excitation intensities as a consequence of energy transfer from

the dispersed material to the solvent. Optical limiting materials for ultrashort (femtosecond or picosecond) laser pulses are less common than those for nanosecond laser pulses because nonlinear scattering for ultrashort laser pulses are usually much weaker than that for nanosecond laser pulses due to slow formation of micro-bubbles.<sup>7</sup>

<sup>12</sup> Thin film materials usually show worse optical limiting performance than solution materials due to lack of solvent to form micro-bubbles as scattering centers. An essential requirement for effective thin film optical limiting materials is strong nonlinear absorption such as multiphoton absorption and excited state absorption.<sup>13</sup>

$\pi$ -conjugated organic molecules such as porphyrins,<sup>14</sup> phthalocyanines<sup>14</sup> and other large aromatic molecules are known to exhibit optical limiting activity to femtosecond laser pulses due to strong multiphoton absorption or excited state absorption. However, thin films of these materials only exhibit femtosecond optical limiting activity over a very narrow wavelength range. Very recently, several research groups reported strong broadband optical limiting properties in graphene,<sup>7</sup> GO,<sup>5, 15</sup> and GO-polymer composite<sup>16</sup> in solutions for nanosecond laser pulses. They attributed the optical limiting effects to nonlinear scattering.

GO sheets contain a mixture of electronically conducting  $sp^2$  and insulating  $sp^3$  carbon domains. Their electronic properties could be tuned by controlling the ratio of  $sp^2/sp^3$  carbon domains,<sup>17, 18</sup> which might have interesting implications on their nonlinear optical properties. The  $sp^2$  domains in GO resemble  $\pi$ -conjugated organic molecules with strong nonlinear optical properties, which motivated us to investigate

the nonlinear optical properties of GO. The investigation of femtosecond nonlinear optical properties of GO is vital for development of future graphene based ultrafast optoelectronic applications.

In this work, we studied exceptional broadband nonlinear optical properties of GO and partially reduced GO thin films for femtosecond laser pulses. The as-prepared GO films displayed exceptional optical limiting effects to femtosecond laser pulses at both 400 and 800 nm, with a huge effective two-photon absorption coefficient of  $\sim 41000 \text{ cm}\cdot\text{GW}^{-1}$  at 400 nm, effective two- and three-photon absorption coefficients at 800 nm of  $\sim 31 \text{ cm}\cdot\text{GW}^{-1}$  and  $\sim 0.47 \text{ cm}^3\cdot\text{GW}^{-2}$  respectively. Most interestingly, their optical limiting performances were found to be significantly enhanced upon partial reduction of GO. The partially reduced GO could be prepared by laser induced reduction or chemical reduction by exposure to the hydrazine vapour. The laser induced reduction of GO could result in enhancement of effective two-photon absorption coefficient at 400 nm by up to  $\sim 19$  times, effective two- and three-photon absorption coefficients at 800 nm by  $\sim 12$  and  $\sim 14.5$  times respectively. The optical limiting thresholds of a 380 nm-thick, partially reduced GO film for femtosecond laser pulses at 800 and 400 nm were found to be as low as  $37 \text{ mJ}\cdot\text{cm}^{-2}$  and  $0.12 \text{ mJ}\cdot\text{cm}^{-2}$  respectively, which are much lower than those of various previously reported materials.<sup>5, 6, 19, 20</sup> The limiting threshold of these films could be further reduced by increasing the film thickness. The chemically reduced GO film displayed complicated nonlinear optical properties. Slightly reduced GO films displayed enhanced nonlinear absorption, while highly

reduced GO films displayed saturable absorption. These GO films can be deposited onto a plastic substrate to fabricate flexible broadband optical limiters with excellent performance to femtosecond laser pulses.

## 5.2 Experimental Section

### Preparation of Graphene Oxide (GO):

GO was prepared from graphite via a modified Hummers and Offeman method.<sup>21</sup> 1.5 g graphite flakes (Asbury Carbons Ltd.) and 1.0 g NaNO<sub>3</sub> were placed in a 500 mL round bottom flask. 45 mL of concentrated H<sub>2</sub>SO<sub>4</sub> was subsequently added into the flask. The mixture was stirred overnight at room temperature. 6.0 g KMnO<sub>4</sub> was then slowly added into the mixture in an ice bath to avoid rapid heat evaluation. The flask was shifted to an oil bath after 4 hrs and the reaction mixture was stirred at 35 °C for another 2 hrs. The temperature was slowly increased to 60 °C and stirred for 4 hrs. Finally, the reaction mixture was added into 40 mL of water and stirred at 90 °C for 5 hrs. The reaction was ended by adding 10 mL of 30% H<sub>2</sub>O<sub>2</sub>, which resulted in a change of color from yellow to brown. The warm solution was then filtered and washed with 5% HCl and water. The obtained solid was dissolved in water and sonicated to exfoliate oxidized graphene. The oxidized graphene was centrifuged at 1000 rpm for 2 min. After removing all visible graphite particles, it was again centrifuged at 15,000 rpm for 2 hrs. This washing procedure was repeated until the pH became 4-5. For complete oxidation, the above dried GO was further treated with 70% HNO<sub>3</sub> (10 mL of

HNO<sub>3</sub>/100 mg of GO). The mixture was sonicated for 8 hrs at 60 °C and the sediment was dispersed in water. The obtained GO was purified by washing multiple times with ethanol and water, and then completely dried using a rotary evaporator. The dried GO was finally dispersed in water for further characterization. The GO in water was spin-coated onto a silica substrate for AFM measurements.

#### **Preparation of GO films:**

The prepared graphene oxide sheets were dissolved in water with a concentration of 5 mg·mL<sup>-1</sup> by ultrasonication. GO films were prepared by spin-coating the graphene oxide solution onto clean oxygen plasma treated glass slides and an oxygen plasma treated plastic sheet at a speed of 1000 rpm. The spin-coating was repeated for different number of times on each glass slide to control the thickness. The film was dried at 70 °C after each layer of spin-coating. The thicknesses of the films were measured by Profilometer (KLA Tencor).

#### **Open-aperture femtosecond Z-scan technique:**

Nonlinear optical properties of these GO films were characterized by using an open-aperture femtosecond Z-scan technique. The Z-scan measurements were performed by using a mode-locked Ti:sapphire oscillator seeded regenerative amplifier, which gives output laser pulses with a central wavelength of 800 nm, pulse duration of ~100 fs and repetition rate of 1 kHz. The laser beam was focused onto the sample with a beam waist of ~20 μm. The transmittance of the GO films was measured as a function

of input fluence, which was varied by moving the samples in and out of beam focus along the z-axis. Z-scan measurements have also been performed by using laser pulses of 400 nm, which were generated by frequency-doubling the 800 nm beam.

### **Experimental setup for laser induced reduction of graphene oxide films**

Laser irradiation on GO film was performed using the same experimental setup for the Z-scan measurements, as shown in Figure 5.1. GO film was moved 35 mm away from the focus point ( $Z=0$ ) and was then irradiated with 400 nm (fluence of  $8 \text{ mJ}\cdot\text{cm}^{-2}$ ) or 800 nm (fluence of  $80 \text{ mJ}\cdot\text{cm}^{-2}$ ) femtosecond laser pulses for different periods of time. The Z-scan measurements were subsequently performed on the irradiated area at much lower excitation intensities.

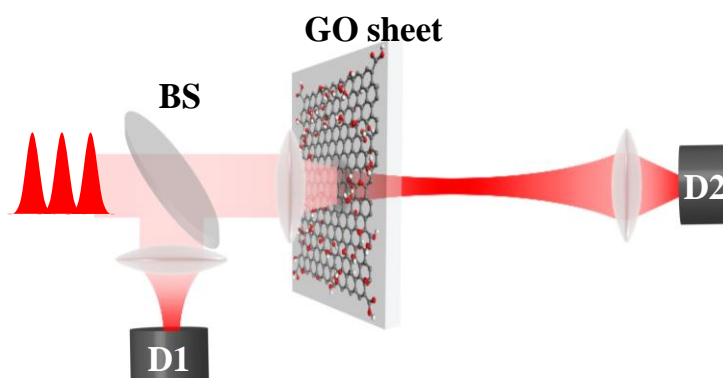


**Figure 5.1:** Experimental setup for laser induced reduction of GO film. D1 and D2: photodiodes.

### **Absorption spectra of GO before and after laser irradiation:**

The experimental setup for measuring absorption spectra of laser reduced GO using white light continuum is shown in Figure 5.2. The 400 nm and white light laser beams overlapped at the same spot on the GO film, while the white light beam has a smaller beam size than that of the 400 nm beam. The transmittance spectra of the



sample were measured by using the white light before and after irradiation of the 400 nm beam for 10 min at fluence of  $8 \text{ mJ}\cdot\text{cm}^{-2}$ . The absorption spectra were obtained by normalizing the obtained transmittance spectra with respect to the transmittance spectra of a glass slide.

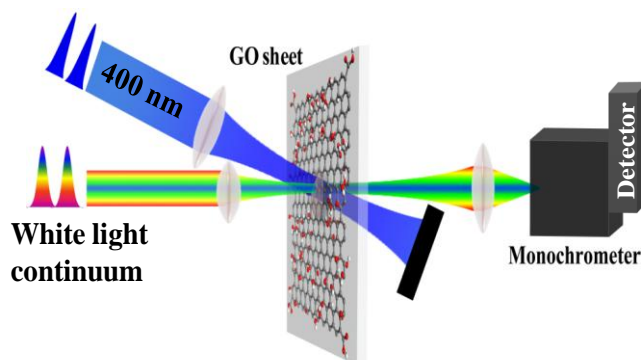


**Figure 5.2:** Experimental setup for the measuring absorption spectra of laser reduced GO films.

### 5.3 Characterizations of Graphene Oxide Films

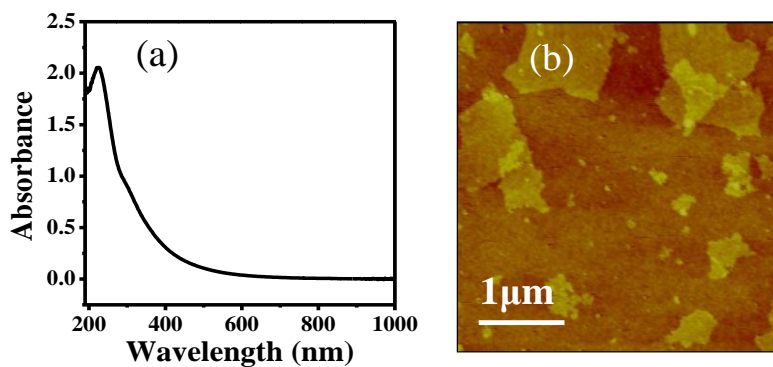


**Figure 5.3:** (a) UV-Vis absorption spectrum of GO in water and (b) the AFM image of the as-prepared GO.

The as-prepared GO sheets were dispersed in water to a concentration of  $5 \text{ mg}\cdot\text{mL}^{-1}$ . The AFM images (Figure 5.3b) showed that the obtained GO sheets are mostly single layer with some a few-layer GO with sizes ranging from 300 nm to a few  $\mu\text{m}$ . The UV-Vis absorption spectrum of GO shows an absorption maximum at 223 nm

(Figure 5.3a), which is due to the  $\pi$ - $\pi^*$  transition of C=C band.

The GO films were prepared by spin-coating the solution onto oxygen plasma treated glass slides at a speed of 1000 rpm. Thicker GO films were prepared by increasing number of layers. The films were dried at 70 °C after each layer of spin-coating. Figure 5.4 shows the transmittance spectra of GO films of different thickness on glass substrates (thickness of 32, 73, 100, 140, and 380 nm for Samples 1-5). These GO films are highly transparent in the near-IR region and the transmittance decreased towards shorter wavelengths. The transmittance of these GO films decreases with increasing film thickness.

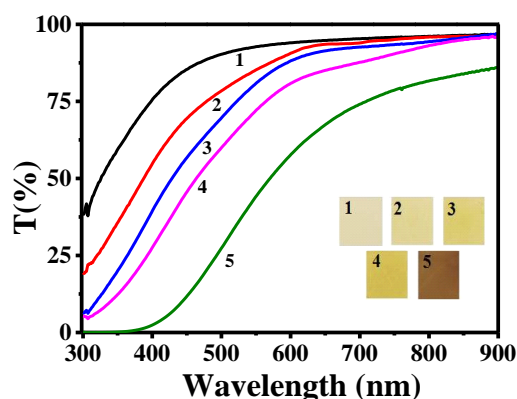


**Figure 5.4:** UV-Vis transmittance spectra and photographs (inset) of GO films of different thicknesses on glass substrates (Samples 1-5).

## 5.4 Nonlinear Optical Properties of Graphene Oxide Films

Nonlinear optical properties of these GO films were characterized by using an open-aperture femtosecond Z-scan technique. Z-scan measurements have also been performed by using laser pulses of 800 nm and 400 nm, respectively. Experiments on different samples have been done and the results of Sample 4 were chosen for

illustration purpose.

#### 5.4.1 Z-scan measurements under low excitation fluences

Figure 5.5 shows the excitation fluence dependent open-aperture Z-scan measurement results of a GO film (Sample 4) at 800 and 400 nm, respectively. At the lowest excitation fluence at 800 nm, the normalized transmittance was found to increase as the sample moved into the beam focus ( $z = 0$ ), indicating an optically induced transparency or saturable absorption behavior. As the excitation fluence increased, reverse saturable absorption was observed instead, indicating existence of strong nonlinear absorption. When 400 nm laser pulses were used, the GO films showed systematical reverse saturable absorption even at very low excitation fluence (Figure 5.5b) despite the high linear absorbance at 400 nm (Figure 5.4), indicating existence of very strong nonlinear absorption at 400 nm.

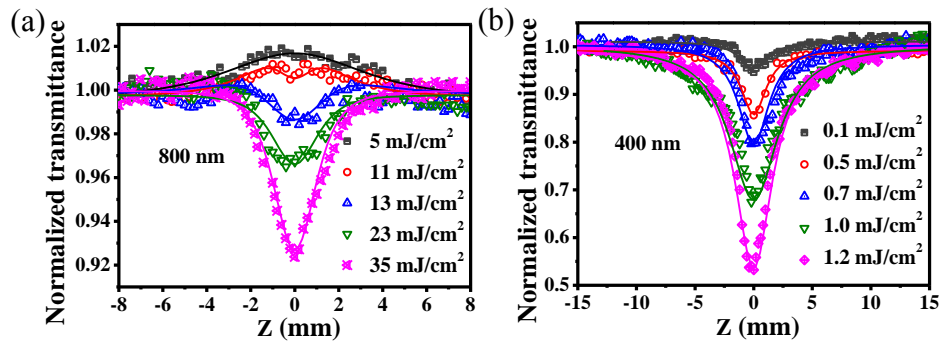


**Figure 5.5:** Open aperture Z-scan results of a GO film (Sample 4) at 800 nm (c) and 400 nm (d) under different input fluences.

The observed saturable absorption behavior at 800 nm under low excitation fluences can be ascribed to ground state bleaching. 800 nm is located at the edge of absorption band of GO (Figure 5.4). Ground state bleaching will be caused by

increasing pump fluence as the sample moved into the beam focus. When the excitation fluence further increases, nonlinear absorption starts to play a dominant role since it is more sensitive to excitation fluence. Reverse saturable absorption was observed instead at high excitation fluences. There are generally two types of nonlinear absorption: excited state absorption and multiphoton absorption, both of which lead to a decrease in transmittance with increasing input fluence. Observation of reverse saturation absorption at very low excitation fluences (Figure 5.5b) suggests very large nonlinearity at 400 nm, which dominates the ground state bleaching at all the excitation fluences used here.

#### 5.4.2 Z-scan theories for characterizing multiphoton process

When a laser beam propagates in an optically thin sample in which multiphoton absorption occurs, the optical intensity inside the sample can be represented by the equation

$$\frac{dI}{dz} = -\left(\alpha_0 \frac{I}{1 + I/I_s} + \sum_n^{n \geq 2} \alpha_n I^n\right), \quad 5.1$$

where  $I$  is the irradiance within the sample and  $z$  is the propagation distance,  $I_s$  is the saturable intensity,  $\alpha_0$  and  $\alpha_n$  are the linear absorption coefficient and  $n$ -photon absorption coefficient, respectively. The two- and three-photon absorption coefficients ( $\alpha_2$  and  $\alpha_3$ ) are generally expressed as  $\beta$  and  $\gamma$  respectively. If only one  $n$ -photon process is considered, the transmitted intensity through the sample can be obtained as<sup>22</sup>

$$I_{out} = \frac{I \exp(-\alpha_0 L)}{[1 + (n-1)\alpha_n L_{eff}^{(n)} I^{n-1}]^{1/(n-1)}}, \quad 5.2$$

$L$  is the sample length;  $L_{eff}^{(n)} = \{1 - \exp[-(n-1)\alpha_0 L]\} / (n-1)\alpha_0$  is the effective sample length related to the  $n$ -photon absorption. For the first-order approximation, when  $[(n-1)\alpha_n L_{eff}^{(n)} (I_{00})^{n-1}]^{1/(n-1)} < 1$ , the Z-scan curve of  $n$ -photon absorption process measuring by Gaussian beam can be expressed by<sup>23</sup>

$$T_{nPA}(z) = 1 - \frac{1}{n^{3/2}} \alpha_n (I_0)^{n-1} L_{eff}^{(n)}, \quad 5.3$$

$I_{00}$  is the peak, on-axis irradiance at the focal point within the sample,  $I_0 = \frac{I_{00}}{1+z^2/z_0^2}$

is the excitation intensity at position  $z$ ,  $z_0 = \pi\omega_0^2/\lambda$  is the Rayleigh range,  $\omega_0$  is the minimum beam waist at the focal point ( $z = 0$ ) and  $\lambda$  is the laser free-space wavelength;

The Z-scan profiles for two-photon ( $n=2$ ) and three-photon ( $n=3$ ) processes can be expressed as

$$T_{2PA}(z) = 1 - \alpha_2 I_0 L_{eff}^{(2)} / 2^{3/2}, \text{ and} \quad 5.4$$

$$T_{3PA}(z) = 1 - \alpha_3 I_0^2 L_{eff}^{(3)} / 3^{3/2}. \quad 5.5$$

Accordingly, a linear fit of  $\ln(1-T)$  versus  $\ln(I_0)$  is expected to give a slope of 1 for two-photon absorption (2PA) and 2 for three-photon absorption (3PA), respectively.

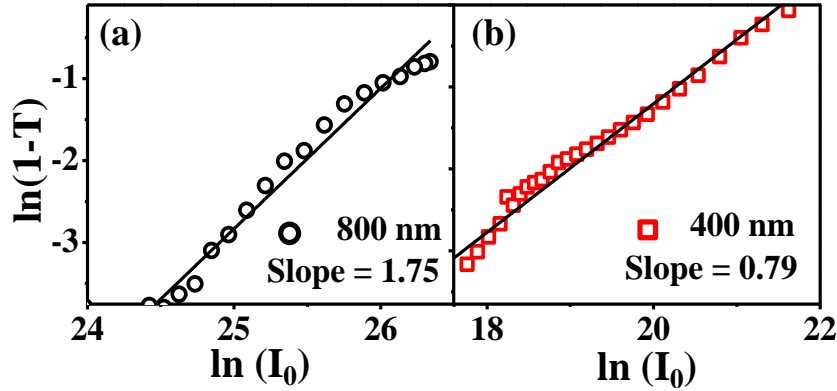


**Figure 5.6:** Plots of  $\ln(1-T)$  versus  $\ln(I_0)$  ( $I_0$ : input intensity) at 800 (a) and 400 nm (b).

As shown in Figure 5.6, the plots of  $\ln(1-T)$  versus  $\ln(I_0)$  at 400 and 800 nm gave slopes of  $\sim 0.79$  and  $\sim 1.75$  respectively, indicating co-existence of one- and two-photon absorption processes at 400 nm, and co-existence of two- and three-photon absorption at 800 nm.<sup>24</sup> The Z-scan measurement results at 400 and 800 nm were fitted by considering one- and two-photon absorption at 400 nm, and one-, two- and three-photon absorption at 800 nm using equations (deduced from equation 5.1):  $\alpha = \alpha_0/(1 + I/I_s) + \beta_{\text{eff}}I$  and  $\alpha = \alpha_0/(1 + I/I_s) + \beta_{\text{eff}}I + \gamma_{\text{eff}}I^2$  respectively, where  $\alpha$  and  $\alpha_0$  are total absorption coefficient and linear absorption coefficient respectively,  $I$  and  $I_s$  are laser intensity and saturation intensity respectively. As it is difficult to distinguish the contributions of excited state absorption and multiphoton absorption using the Z-scan technique, the fitting results give effective two- and three-photon absorption coefficients ( $\beta_{\text{eff}}$  and  $\gamma_{\text{eff}}$ ). An average value of  $\sim 41000 \pm 1000 \text{ cm}\cdot\text{GW}^{-1}$  was obtained for effective two-photon absorption coefficient ( $\beta_{\text{eff}}$ ) at 400 nm. The effective two- and three-photon absorption coefficients ( $\beta_{\text{eff}}$  and  $\gamma_{\text{eff}}$ ) at 800 nm were calculated to be  $\sim 31 \pm 2 \text{ cm}\cdot\text{GW}^{-1}$  and  $\sim 0.47 \pm 0.03 \text{ cm}^3\cdot\text{GW}^{-2}$  respectively.

### 5.4.3 Z-scan measurements under high excitation fluences

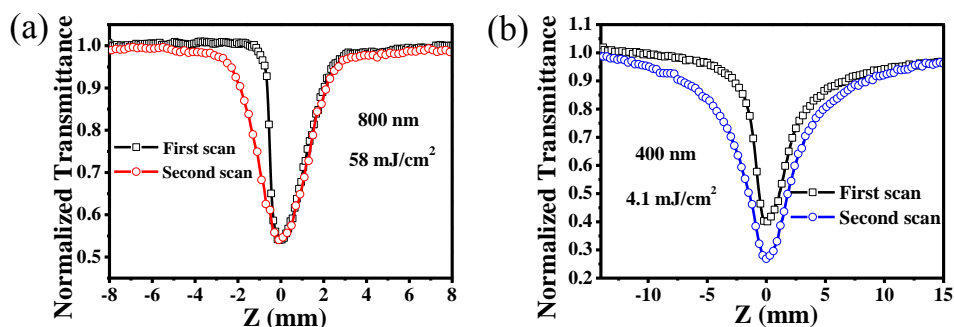


**Figure 5.7:** Consecutive Z-scan measurements under high excitation fluences at (a) 800 nm (fluence of 58 mJ·cm<sup>-2</sup> at focal point) and (b) 400 nm (fluence of 4.1 mJ·cm<sup>-2</sup> at focal point).

Some asymmetric and non-repeatable Z-scan curves were observed when conducting the Z-scan measurements under very high excitation fluences, such as 58 mJ·cm<sup>-2</sup> at 800 nm or 4.1 mJ·cm<sup>-2</sup> at 400 nm (Figure 5.7). These results indicated the occurrence of laser induced change in the GO films under strong laser illumination. It has been previously reported that femtosecond laser irradiation can partially reduce the GO.<sup>25</sup> We also noticed a change of color from yellow to brown in the illuminated area, which is consistent with increased extent of conjugation and ratio of sp<sup>2</sup>/sp<sup>3</sup> carbon domains in the GO film after the reduction.

The absorption of GO was found to increase after 400 nm laser irradiation (Figure 5.8a), which can be ascribed to the restoration of sp<sup>2</sup> π-conjugated network upon laser induced reduction of GO. Similar spectra change was observed before and after illumination of the GO film with strong laser beams at 800 nm.

Raman spectra changes of the as-prepared GO film upon laser illumination are also shown in Figure 5.8b. The two peaks at 1354 and 1595 cm<sup>-1</sup> correspond to D and

G-bands respectively. The G-band is attributed to the  $E_{2g}$  phonon mode of  $sp^2$  bonded carbon atoms and the D-band is related to the local defects and disordered graphite. The intensity ratio of two bands,  $I_D/I_G$ , for as-prepared GO and laser induced partially reduced GO are 0.73 and 0.66 respectively. The decrease in  $I_D/I_G$  is consistent with partial reduction of disordered sites upon laser irradiation of GO.

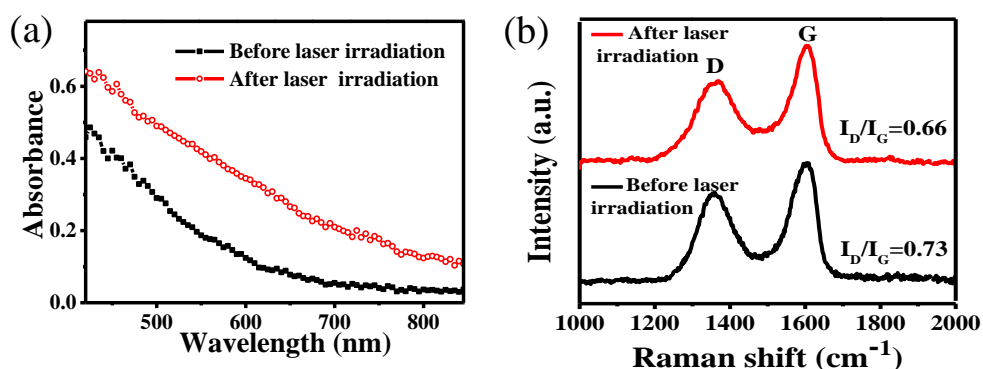


**Figure 5.8:** Absorption spectra (a) and Raman spectra (b) of GO film (Sample 4) before and after laser irradiation at 400 nm for 10 min with fluence of  $8 \text{ mJ}\cdot\text{cm}^{-2}$ .

## 5.5 Tunable Nonlinear Optical Properties Controlled by Degree of Reduction

The asymmetric shape of the Z-scan curves under very high excitation fluences suggested that reduction of GO caused an enhancement in their nonlinear absorption. To further confirm and understand the laser induced enhancement of nonlinear optical properties of GO, Z-scan measurements were performed on GO films dealt with successive laser irradiation and chemical reduction, respectively.

### 5.5.1 Laser irradiation reduction

A small portion of the GO film (Sample 4) was intentionally irradiated with



femtosecond laser pulses of high fluences (fluence of  $80 \text{ mJ}\cdot\text{cm}^{-2}$  at 800 nm and  $8 \text{ mJ}\cdot\text{cm}^{-2}$  at 400 nm) for different periods of time. The Z-scan measurements were subsequently performed on the irradiated area at much lower excitation fluences ( $25 \text{ mJ}\cdot\text{cm}^{-2}$  for 800 nm and  $0.6 \text{ mJ}\cdot\text{cm}^{-2}$  for 400 nm at the focus point) and the results are shown in Figure 5.9. It can be clearly seen that exposure to strong femtosecond laser pulses resulted in a significant increase in nonlinear absorption of the GO films. The nonlinear absorption quickly increased to maximum within a few minutes ( $\sim 1$  min under irradiation at 800 nm and  $\sim 6$  min at 400 nm) and remained nearly unchanged for up to 2 hours. The effective two-photon absorption coefficient ( $\beta_{\text{eff}}$ ) at 400 nm of GO increased by  $\sim 19$  times under strong irradiation at 400 nm. The effective two- and three-photon absorption coefficients ( $\beta_{\text{eff}}$  and  $\gamma_{\text{eff}}$ ) at 800 nm increased by  $\sim 12$  and  $\sim 14.5$  times respectively after laser irradiation at 800 nm. The observed significantly enhanced nonlinear absorption can be ascribed to increased conjugation length and formation of more and larger  $sp^2$  domains in the GO sheet upon laser induced reduction.

Similar laser irradiation treatments have been applied to GO films of different thickness (Sample 1-5) and their nonlinear optical properties were then characterized by using Z-scan measurements. The GO films were irradiated with strong femtosecond laser pulses for 10 min to ensure their nonlinear absorption reaching the maximum. The input fluence dependent transmittance at 800 and 400 nm (Figure 5.9c&d) were extracted from the Z-scan measurement results. The transmittance of these laser

reduced GO films decreased with increasing input fluence, exhibiting promising optical limiting activity for femtosecond laser pulses at both 800 and 400 nm.

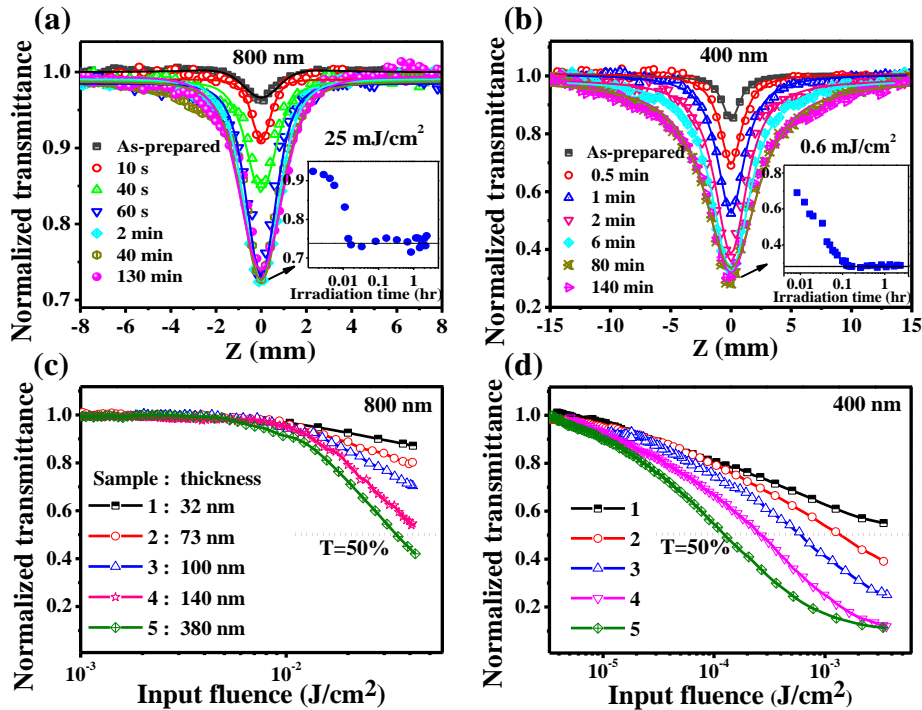


**Figure 5.9:** (a,b) Open-aperture Z-scan curves of a partially reduced GO film (Sample 4, film thickness=140 nm) at 800 nm (fluence of  $25 \text{ mJ}\cdot\text{cm}^{-2}$  at focal point) (a) and 400 nm (fluence of  $0.6 \text{ mJ}\cdot\text{cm}^{-2}$  at focal point) (b) by laser irradiation of different periods of time. (Insets: normalized transmittance at the focus ( $z=0$ ) versus laser illumination time) (c,d) Optical limiting response of laser induced partially reduced GO films of different thickness to femtosecond laser pulses at 800 nm (c) and 400 nm (d).

The optical limiting threshold values ( $F_{50}$ , defined as the incident fluence at which the transmittance falls to 50% of the linear transmittance) for different samples at 800 and 400 nm are summarized in Table 5-1 & 5-2. The  $F_{50}$  values of 77, 57, 46, 42, and 37  $\text{mJ}\cdot\text{cm}^{-2}$  at 800 nm, and 6, 1.4, 0.6, 0.3, and 0.12  $\text{mJ}\cdot\text{cm}^{-2}$  at 400 nm were obtained for Samples 1-5 respectively. The optical limiting threshold values ( $F_{50}$ ) at both 800 and 400 nm decreased with increasing film thickness. The  $F_{50}$  of these partially reduced GO films for femtosecond laser pulses are significantly lower than those previously

reported metal nanoparticles ( $26000 \text{ mJ}\cdot\text{cm}^{-2}$  at  $780 \text{ nm}$ )<sup>6</sup> and conjugated organic molecules ( $117 \text{ mJ}\cdot\text{cm}^{-2}$  at  $800 \text{ nm}$ ).<sup>26</sup> Most importantly, these partially reduced GO materials display huge nonlinear absorption at  $400 \text{ nm}$  with exceptionally low limiting thresholds for femtosecond laser pulses at  $400 \text{ nm}$ . So far there is no report on femtosecond optical limiting materials at  $400 \text{ nm}$ .

**Table 5-1:** Linear transmittance (T), effective two-photon absorption coefficients ( $\beta_{\text{eff}}$ ), optical limiting onsets ( $F_{\text{on}}$ ) and thresholds ( $F_{50}$ ) of laser reduced GO films at  $400 \text{ nm}$ .

Sample	Linear Transmittance	Two-photon Absorption Coefficient	Optical Limiting Onset [b]	Optical Limiting Threshold
No.	T%	$\beta_{\text{eff}}$ [ $\text{cm}\cdot\text{GW}^{-1}$ ]	$F_{\text{on}}$ [ $\text{mJ}\cdot\text{cm}^{-2}$ ]	$F_{50}$ [ $\text{mJ}\cdot\text{cm}^{-2}$ ]
1	62	$612032\pm 10250$	$4.8\text{E}-03$	6
2	45	$662627\pm 11272$	$4.3\text{E}-03$	1.4
3	32	$713692\pm 13225$	$4.1\text{E}-03$	0.6
4	23	$768000\pm 12253$	$3.9\text{E}-03$	0.3
5	2	$709385\pm 10337$	$3.6\text{E}-03$	0.12
6 [a]	2	$672837\pm 13121$	$3.3\text{E}-03$	0.11

[a] Sample 6 is on plastic substrate with thickness of  $400 \text{ nm}$ ; [b] For direct comparison with the literature values, the optical limiting onset ( $F_{\text{on}}$ , defined as the incident fluence at which optical limiting activity starts) values are also included.

**Table 5-2:** Linear transmittance (T), effective two- and three-photon absorption coefficients ( $\beta_{\text{eff}}$  and  $\gamma_{\text{eff}}$ ), optical limiting onsets ( $F_{\text{on}}$ ) and thresholds ( $F_{50}$ ) of laser reduced GO films at  $800 \text{ nm}$ .

Sample	Linear Transmittance	Multi-photon Absorption Coefficient		Optical Limiting Onset	Optical Limiting Threshold
No.	T%	$\beta_{\text{eff}}$ [ $\text{cm}\cdot\text{GW}^{-1}$ ]	$\gamma_{\text{eff}}$ [ $\text{cm}^3\cdot\text{GW}^{-2}$ ]	$F_{\text{on}}$ [ $\text{mJ}\cdot\text{cm}^{-2}$ ]	$F_{50}$ [ $\text{mJ}\cdot\text{cm}^{-2}$ ]
1	78	$336\pm 2$	$5.35\pm 0.07$	6	77
2	77	$339\pm 2$	$5.75\pm 0.08$	5.4	57
3	76	$358\pm 3$	$6.06\pm 0.1$	5.2	46
4	75	$369\pm 6$	$6.8\pm 0.2$	3.6	42
5	66	$356\pm 6$	$6.28\pm 0.3$	2.4	37
6	64	$346\pm 5$	$6.10\pm 0.3$	1.5	31

### 5.5.2 Chemical reduction

GO can also be reduced via a chemical method by exposing the film to the hydrazine vapors, which can convert the insulating GO to a semi-metal.<sup>17, 18</sup> This method allows to control the extent of reduction and ratio of  $sp^2$  and  $sp^3$  carbon domains in the GO sheets by controlling exposure time to the hydrazine vapor.<sup>17</sup> The gradual transformation of GO was monitored by the transmittance measurements after different periods of exposure time (Figure 5.10a). It can be seen that the transmittance gradually decreased with increasing exposure time to hydrazine. The decreasing transmittance is due to formation of larger  $sp^2$  conjugated network upon chemical reduction.<sup>17</sup>

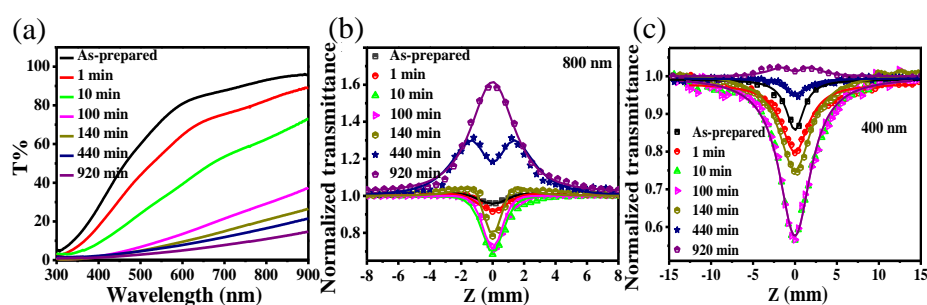


**Figure 5.10:** Linear transmittance (a) and Z-scan measurement results at 800 nm (fluence of  $25 \text{ mJ}\cdot\text{cm}^{-2}$  at focal point) (b) at 400 nm (fluence of  $0.6 \text{ mJ}\cdot\text{cm}^{-2}$  at focal point) (c) of a GO film (Sample 4) upon exposure to hydrazine vapor for different periods of time.

Nonlinear optical properties of the chemically reduced GO film after different periods of hydrazine exposure were measured by performing Z-scan measurements at 800 and 400 nm (Figure 5.10b&c). It can be seen that nonlinear absorption of the GO film at both 800 and 400 nm increased significantly upon a short period (10 min) of exposure to the hydrazine vapor. The results are consistent with enhanced nonlinear

absorption upon laser induced partial reduction of GO. However, this trend is reversed after extended exposure of the GO films to the hydrazine vapor. Longer exposure (>100 min) to the hydrazine vapor led to a decrease in nonlinear absorption and the Z-scan profiles eventually switched to saturable absorption at both 800 and 400 nm.

### 5.5.3 Mechanism analysis

These results indicated that partially reduced GO films act as good optical limiting materials while highly reduced GO films are good saturable absorbers. Previous studies revealed that GO underwent insulator-semiconductor-semi-metal transition depending on the reduction time.<sup>18,27</sup> This transition can be explained by the change in fraction of  $sp^2$  domains in the GO sheet. Previously Eda et al.<sup>17</sup> reported that the blue photoluminescence (PL) of GO was enhanced upon partial reduction due to the increase of localized  $sp^2$  domains. The PL signal was quenched upon high reduction of GO due to the interconnectivity of the localized  $sp^2$  domains, which results the increase of nonradiative recombination rate.<sup>17</sup> As-prepared GO sheets contain mostly  $sp^3$  domains and less  $sp^2$  domains (Figure 5.11a). After a short period of exposure to hydrazine, the fraction of strongly delocalized semiconducting  $sp^2$  domains increases (Figure 5.11b), which leads to significant increase in nonlinear absorption. Further reduction of the GO films leads to formation of larger  $sp^2$  domains (Figure 5.11c).<sup>17, 18</sup> Saturable absorption (due to strong linear absorption) may dominate over nonlinear absorption and an overall saturable absorption would be resulted. Nonlinear optical properties of GO can thus be controlled by varying the degree of reduction.

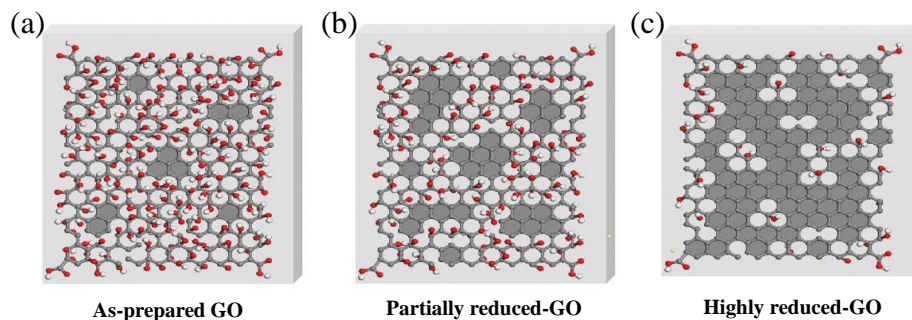


**Figure 5.11:** Schematic structures of GO at different stages of reduction: as-prepared (a), partially reduced (b) and highly reduced (c).

There are generally two mechanisms responsible for optical limiting effects: nonlinear scattering and nonlinear absorption.<sup>7, 13</sup> Development of thin film optical limiting materials for femtosecond laser pulses with low thresholds is very challenging because of lack of contribution from nonlinear scattering. To the best of our knowledge, there is no report on femtosecond optical limiting materials at 400 nm so far. Most materials generally display saturable absorption in the near UV region. These GO films, in particular the partially reduced GO films, display very strong two-photon absorption at 400 nm (with huge effective two-photon absorption coefficient of  $768000 \text{ cm}\cdot\text{GW}^{-1}$ ) and strong two- and three-photon absorption at 800 nm, which make them excellent candidates for broadband (from UV to near-Infrared) optical limiting materials for femtosecond laser pulses.

## 5.6 Graphene Oxide on a Flexible Plastic Substrate

We have also prepared GO films on a plastic substrate by using the spin-coating method. The thickness of the GO films is 400 nm. After laser induced partial reduction, the film displayed excellent optical limiting effects. The optical limiting threshold is

0.11 mJ·cm<sup>-2</sup> for 400 nm and 31 mJ·cm<sup>-2</sup> for 800 nm(Figure 5.12).

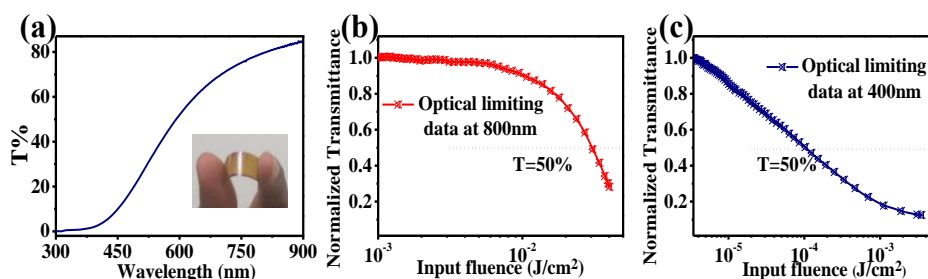


**Figure 5.12:** (a) UV-Vis spectrum of a GO film on a plastic substrate (Sample 6) and its optical limiting properties at (b) 800 and (c) 400 nm after laser induced reduction.

## 5.7 Conclusion

We have investigated the broadband nonlinear optical properties of GO thin films and their optical limiting activity for femtosecond laser pulses at 800 and 400 nm, which could be tuned by the extent of reduction. The as-prepared GO films were found to exhibit strong broadband optical limiting behaviors, which were significantly enhanced upon partial reduction by using laser irradiation or chemical reduction methods. The laser induced reduction of GO could result in enhancement of effective two-photon absorption coefficient at 400 nm by up to ~19 times, effective two- and three-photon absorption coefficients at 800 nm by ~12 and ~14.5 times respectively. Highly reduced GO films prepared by using chemical method displayed strong saturable absorption behavior. The optical limiting thresholds of these partially reduced GO films are significantly lower than those of previously reported  $\pi$ -conjugated organic molecules and metal nanoparticles. These thin films could be easily fabricated on glass and even plastic substrates by using solution processing methods on a large scale. Low cost, easy preparation, and excellent nonlinear optical properties make

these GO materials promising candidates for practical applications as broadband femtosecond optical limiters or saturable absorbers.

## References

- (1) Maiman, T.H. *Nature* **1960**, *187*, 493-494.
- (2) Tutt, L.W. and Boggess, T.F. *Prog. Quant. Electron.* **1993**, *17*, 299-338.
- (3) Mamidala, V., Polavarapu, L., Balapanuru, J., Loh, K.P., Xu, Q.H. and Ji, W. *Opt. Express* **2010**, *18*, 25928-25935.
- (4) Bonaccorso, F., Sun, Z., Hasan, T. and Ferrari, A.C. *Nat. Photonics* **2010**, *4*, 611-622.
- (5) Feng, M., Zhan, H.B. and Chen, Y. *Appl. Phys. Lett.* **2010**, *96*, 033107.
- (6) Polavarapu, L., Venkatram, N., Ji, W. and Xu, Q.H. *ACS Appl. Mater. Interfaces* **2009**, *1*, 2298-2303.
- (7) Wang, J., Hernandez, Y., Lotya, M., Coleman, J.N. and Blau, W.J. *Adv. Mater.* **2009**, *21*, 2430-2435.
- (8) Scalora, M., Dowling, J.P., Bowden, C.M. and Bloemer, M.J. *Phys. Rev. Lett.* **1994**, *73*, 1368-1371.
- (9) Chen, P., Wu, X., Sun, X., Lin, J., Ji, W. and Tan, K.L. *Phys. Rev. Lett.* **1999**, *82*, 2548-2551.
- (10) Polavarapu, L., Xu, Q.H., Dhoni, M.S. and Ji, W. *Appl. Phys. Lett.* **2008**, *92*, 263110.
- (11) Lee, Y.H., Yan, Y., Polavarapu, L. and Xu, Q.H. *Appl. Phys. Lett.* **2009**, *95*, 023105.
- (12) Francois, L., Mostafavi, M., Belloni, J. and Delaire, J.A. *Phys. Chem. Chem. Phys.* **2001**, *3*, 4965-4971.
- (13) He, G.S., Tan, L.S., Zheng, Q. and Prasad, P.N. *Chem. Rev.* **2008**, *108*, 1245-1330.
- (14) Calvete, M., Yang, G.Y. and Hanack, M. *Synth. Met.* **2004**, *141*, 231-243.
- (15) Liu, Z.B., Wang, Y., Zhang, X.L., Xu, Y.F., Chen, Y.S. and Tian, J.G. *Appl. Phys. Lett.* **2009**, *94*, 021902.
- (16) Zhu, J.H., Li, Y.X., Chen, Y., Wang, J., Zhang, B., Zhang, J.J. and Blau, W.J. *Carbon* **2011**, *49*, 1900-1905.
- (17) Eda, G., Lin, Y.Y., Mattevi, C., Yamaguchi, H., Chen, H.A., Chen, I.S., Chen,



- C.W. and Chhowalla, M. *Adv. Mater.* **2010**, *22*, 505-509.
- (18) Eda, G., Mattevi, C., Yamaguchi, H., Kim, H. and Chhowalla, M. *J. Phys. Chem. C* **2009**, *113*, 15768-15771.
- (19) Lim, G.K., Chen, Z.L., Clark, J., Goh, R.G.S., Ng, W.H., Tan, H.W., Friend, R.H., Ho, P.K.H. and Chua, L.L. *Nat. Photonics* **2011**, *5*, 554-560.
- (20) Zhao, B.S., Cao, B.B., Zhou, W.L., Li, D. and Zhao, W. *J. Phys. Chem. C* **2010**, *114*, 12517-12523.
- (21) Hummers, W.S. and Offeman, R.E. *J. Am. Chem. Soc.* **1958**, *80*, 1339-1339.
- (22) Sutherland, R.L., McLean, D.G. and Kirkpatrick, S., *Handbook of Nonlinear Optics*. Vol. 82. **2003**: CRC.
- (23) Gu, B., Huang, X.Q., Tan, S.Q., Wang, M. and Ji, W. *Appl. Phys. B: Laser O* **2009**, *95*, 375-381.
- (24) Wang, H., Huff, T.B., Zweifel, D.A., He, W., Low, P.S., Wei, A. and Cheng, J.-X. *Proc. Natl. Acad. Sci. U. S. A.* **2005**, *102*, 15752-15756.
- (25) Zhang, Y.L., Guo, L., Wei, S., He, Y.Y., Xia, H., Chen, Q.D., Sun, H.B. and Xiao, F.S. *Nano Today* **2010**, *5*, 15-20.
- (26) Patra, A., Venkatram, N., Rao, D.N. and Radhakrishnan, T.P. *J. Phys. Chem. C* **2008**, *112*, 16269-16274.
- (27) Eda, G., Fanchini, G. and Chhowalla, M. *Nat. Nanotechnol.* **2008**, *3*, 270-274.

## Chapter 6. Conclusions and Outlook

By employing several ultrafast laser spectroscopic techniques, some intriguing optical properties of graphene oxide (GO) sheets and gold nanoparticles (Au NPs) have been explored in this dissertation, including nonlinear optical properties such as nonlinear absorption, two-photon photoluminescence (TPPL) as well as the electronic relaxation dynamics. In this final chapter, conclusions will be given by reviewing the main results and an outlook on the future work will also be provided.

### 6.1 Conclusions

Gold nanorods (Au NRs) and coupled Au NPs are known to display strong TPPL. To figure out the underlying mechanisms, we developed and performed two-pulse emission modulation spectroscopy (TPEM) and transient absorption spectroscopy to investigate their excitation dynamics.

The excitation mechanism of TPPL in Au NPs was discussed in Chapter 2. It was found that the two-photon excitation of TPPL in Au NRs was not a coherent two-photon absorption process via a virtual intermediate state but two sequential one-photon absorption steps involving a real intermediate state. This sequential absorption mechanism in Au NPs could be confirmed by the apparently different TPEM decay profiles between Au NPs and a standard two-photon absorption organic dye molecule: Fluorescein, which shares the coherent two-photon absorption mechanism. Previous support for the sequential TPA in metal nanoparticles was mainly

based on the TPPL excitation polarization dependence. However, this evidence was questioned by some other experimental results. In contrast, our results showed that the TPEM time constant measured in Au NRs was consistent with the lifetime of intermediate state measured from femtosecond pump-probe technique. Therefore, our TPEM experimental results provide a more conclusive evidence for the sequential TPA mechanism in Au NRs. Furthermore, our results also indicate that plasmon coupling between adjacent nanoparticles in coupled Au nanostructures significantly enhance the two-photon excitation efficiency by two sequential one-photon absorption steps. As the energy and densities of these intermediate states could be tuned by the dimension of nanoparticles and inter-particle coupling, their nonlinear plasmonic properties could be engineered to cater various applications. Our studies are very helpful for understanding the fundamental excitation nature of nonlinear optical properties in various Au nanostructures as well as their practical applications in two-photon sensing, imaging, phototherapy and optoelectronics.

To further understand the excitation dynamics of TPPL in Au NRs, the solvent dependent TPPL properties of Au NRs were investigated in Chapter 3. The TPPL intensities of Au NRs in different organic solvents including DMF, DEG, CH<sub>3</sub>OH, C<sub>2</sub>H<sub>5</sub>OH, CH<sub>3</sub>CN, DMSO and THF were found to be significantly lower than that in H<sub>2</sub>O. The quenching mechanisms were studied by performing the ultrafast time-resolved transient absorption and pump-probe measurements. Different from the decay behavior of Au NRs in H<sub>2</sub>O, an additional transient species was observed for Au

NRs in organic solvents such as DMF or DEG upon photo-excitation. This additional transient species was found to appear on a time scale of tens of picoseconds and subsequently to disappear on a time scale of nanoseconds. This intermediate state can be ascribed to the charge separated species. The observation of this transient species indicates that the observed TPPL quenching in organic solvents is due to electron transfer from electron-donating solvents to the excited Au NRs. The charge transfer mechanism was further supported by the observation that the TPPL intensity of Au NRs in H<sub>2</sub>O was found to be quenched by nearly 5.0-fold in the presence of S<sup>2-</sup>. These findings are of great importance in terms of understanding the carrier dynamics of Au NPs. The results also provide valuable insight on the choice of surface conjugated surfactants to improve their TPPL efficiency for various biological applications.

In Chapter 4 & 5, we transferred our research focus to the nonlinear optical properties of GO, not only because its two-dimensional structure can act as an excellent platform for GO-metal nanocomposites but also its own exciting nonlinear optical properties can be tailored by the heterogeneous distribution of sp<sup>2</sup> and sp<sup>3</sup> domains. We performed transient absorption and pump-probe spectroscopy to study the broadband ultrafast carrier relaxation dynamics of as-prepared GO and reduced GO in Chapter 4. Both GO solution and GO film exhibited strong excited state absorption over the broad range of probe wavelengths from visible to infrared, which were ascribed to the localized states arising from the small size of sp<sup>2</sup> cluster isolated by sp<sup>3</sup> sites in GO sheets. However, the carrier relaxation became faster in GO films

compared to GO solution. The aggregation of  $sp^2$  clusters in GO sheets induced strong interlayer coupling is responsible for the faster relaxation in GO films compared to that of GO in solution. The transient absorption spectra of GO switched over from excited-state absorption to saturable absorption when GO was converted to reduced GO reduced by thermal annealing. Carrier relaxation of photo-excited reduced GO film was found to be significantly faster compared to that of GO and quite similar to that of pristine graphene. These results unveil that GO films should be good potential candidates for broadband optical limiting materials, whereas reduced GO can be used as broadband saturable absorber.

Inspired by the above results, we further investigated the nonlinear optical properties of GO and reduced GO thin films by femtosecond open aperture Z-scan measurement in Chapter 5. The as-prepared GO films were found to exhibit strong broadband optical limiting behaviors, which were significantly enhanced upon partial reduction by using laser irradiation or chemical reduction methods. The laser induced reduction of GO could result in huge enhancement of effective two-photon and three-photon absorption coefficient at 400 nm and 800 nm respectively. Highly reduced GO films prepared by using chemical method displayed strong saturable absorption behavior. The optical limiting thresholds of these partially reduced GO films are significantly lower than those of previously reported  $\pi$ -conjugated organic molecules and metal nanoparticles. These thin films could be easily fabricated on glass or plastic substrates by using solution processing methods on a large scale. Low cost,

easy preparation and excellent nonlinear optical properties make these GO materials promising candidates for practical applications.

## 6.2 Outlook

Based on the studies presented in this thesis, some perspectives about the future work are highlighted here. One direction is the development of femtosecond laser spectroscopic techniques. Ultrafast laser spectroscopic techniques are of great importance and indispensable to the study of optical phenomena spanning various disciplines from physics, chemistry to material science. With the help of femtosecond laser pulses, time resolved spectroscopy can monitor the dynamic processes occur in time scale as short as  $10^{-15}$  s. Measurements with different polarization configurations can provide even more detailed information about the electron motions such as depolarization, spin orientation in anisotropic nanostructures and molecules. However, it should be noticed that the techniques employed in this thesis mainly consist of two pulses with identical polarization. As most of nanostructures, in particular, noble metal nanoparticles prepared by wet-chemical methods, are impossible to be isotropic structures, it would be more promising to develop some novel spectroscopic techniques with various excitation and emission polarization configurations to study their anisotropic nonlinear optical properties as well as the underlying carrier relaxation dynamics.

We should also point out that most of the results presented in this thesis were

achieved by the large-scale ensemble measurements. Due to the free rotation of Au nanoparticles in solution, the orientations of the nanoparticles could not be resolved in ensemble measurements. However, some optical properties are very sensitive to the orientation, such as the polarization dependent behaviors of anisotropic nanoparticles. These studies are very challenging and difficult in ensemble measurements. Recently, some novel techniques such as dark-field scattering as well as the fluorescence microscopy have been developed and utilized to study the optical properties of metal nanoparticles at single particle level. Single particle measurements effectively avoid the free rotation of nanoparticles in suspension and allow the detailed studies on nanoparticles with fixed orientation and well-known morphology. Single particle study has attracted increasing attention in metal nanoparticles research area. Therefore, nonlinear optical study at single particle level would pave the way for us to achieve a more comprehensive understanding of the intrinsic properties of nanoparticles in the future.

Besides the experimental improvements, a comprehensive study on the GO and metal nanocomposites would also be desirable. As GO is an excellent platform for noble metal nanoparticles, the interaction between GO and metal nanoparticles might be expected to give exciting nonlinear optical properties in GO-metal nanocomposites. The enhanced TPPL properties as well as the synergic nonlinear absorption effects of GO-metal nanocomposites have been observed in our group. The ultrafast dynamics studies on these materials should also be beneficial for a better understanding of these

effects and exploring the various kinds of applications from optoelectronics to bio-engineering based on GO and noble metal nanocomposites.